

DTIC FILE COPY

AD-A233 106

12

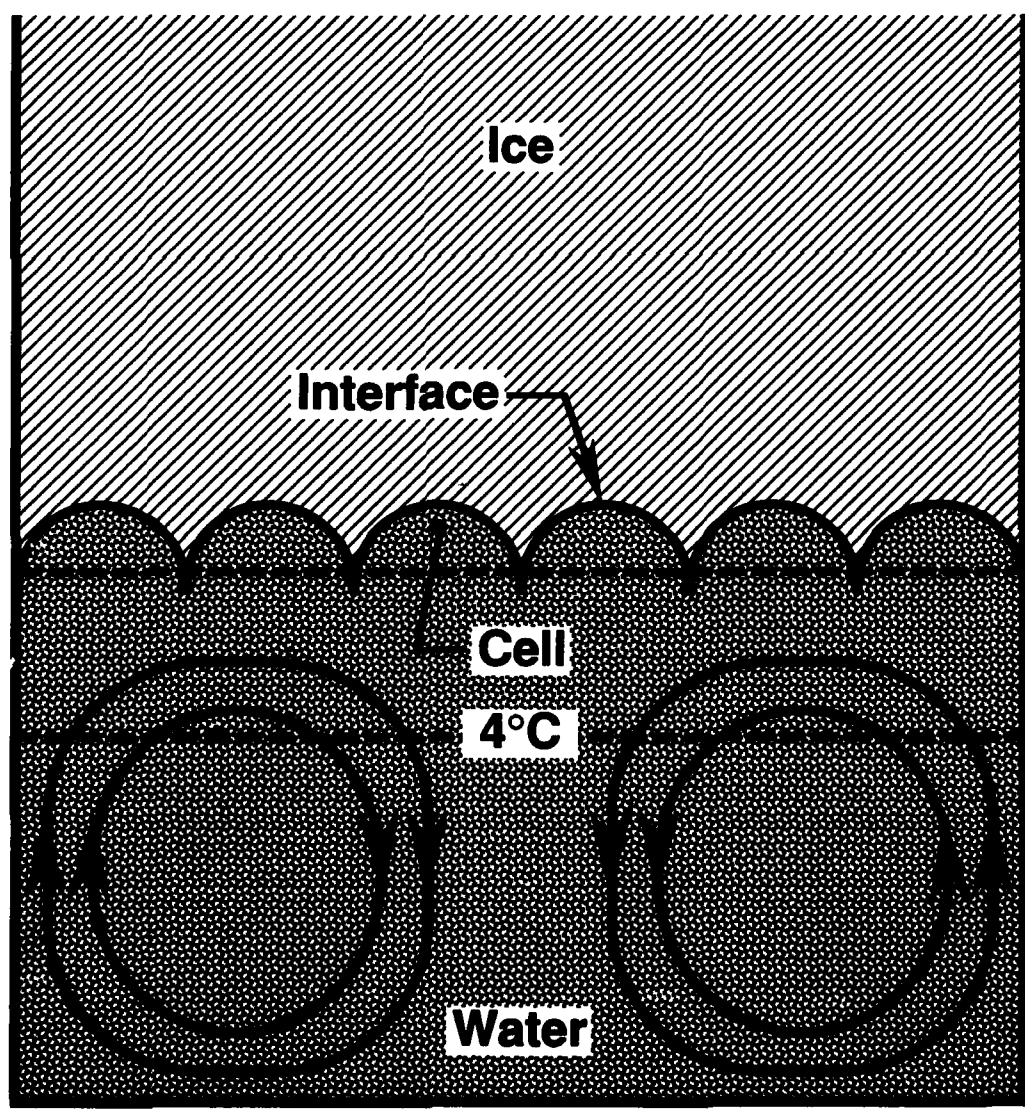


DTIC
SELECTE
MAR 22 1991
S D D

Natural Convection Heat Transfer in Water Near its Density Maximum

Yin-Chao Yen

December 1990



DISTRIBUTION STATEMENT A

Approved for public release
Distribution Unlimited

91 3 19 106

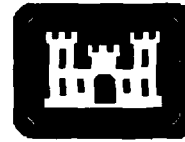
90-4

MONOGRAPH

For conversion of SI metric units to U.S./British customary units of measurement consult ASTM Standard E380, Metric Practice Guide, published by the American Society for Testing and Materials, 1916 Race St., Philadelphia, Pa. 19103.

Cover: Convection cells at the water/ice interface.

Monograph 90-4



**U.S. Army Corps
of Engineers**
Cold Regions Research &
Engineering Laboratory

Natural Convection Heat Transfer in Water Near its Density Maximum

Yin-Chao Yen

December 1990

Accession For	
NTIS CR&I	<input checked="" type="checkbox"/>
DTIC TAB	<input type="checkbox"/>
Unannounced	<input type="checkbox"/>
Justification	
By	
Distribution /	
Availability Codes	
Dist	Availability or Special
A-1	



Prepared for
OFFICE OF THE CHIEF OF ENGINEERS

Approved for public release; distribution is unlimited.

PREFACE

This monograph was prepared by Dr. Yin-Chao Yen, Geophysical Sciences Branch, Research Division, U.S. Army Cold Regions Research and Engineering Laboratory. Funding for this research was provided by DA Project 4A161102AT24, *Research in Snow, Ice and Frozen Ground*, Task SS Work Unit 09, *Phase Change Thermodynamics in Cold Regions Materials*.

The manuscript of this monograph was technically reviewed by Dr. Virgil Lunardini and Dr. Yoshisuke Nakano of CRREL.

The contents of this report are not to be used for advertising or promotional purposes. Citation of brand names does not constitute an official endorsement or approval of the use of such commercial products.

CONTENTS

	Page
Preface	ii
Nomenclature	vi
Introduction	1
General description of Rayleigh instability	1
Effect of 4°C water on onset of convection	2
In a confined horizontal layer	2
In a melt layer with a free surface	10
In a melt layer between vertical plates	13
Effect of 4°C on heat transfer in pure water and ice-water systems	19
In a vertical enclosure	19
In a vertical annulus	24
Between horizontal concentric cylinders	32
In a square enclosure	47
In rectangular enclosure	57
In a horizontal layer	61
In a circular and confined melt layer	71
Melting in bulk water	75
Discussion and conclusions	86
Onset of convection	86
Flow patterns and natural convective heat transfer	88
Literature cited	89
Abstract	93

ILLUSTRATIONS

Figure

1. Critical Rayleigh number for $\lambda_2 = 0$	4
2. $(Ra_c)_{\lambda_2}/(Ra_c)_{\lambda_2=0}$ vs λ_2 with λ_1 as parameter for rigid-free case	4
3. $(Ra_c)_{\lambda_2}/(Ra_c)_{\lambda_2=0}$ vs λ_2 with λ_1 as parameter for rigid-rigid case	5
4. Ra_c as function of T_1 or T_2	5
5. Principal stability diagram	6
6. Critical Rayleigh number Ra_c as function of T_1 with T_2 as a parameter for $T_w = \text{constant}$	7
7. Critical Rayleigh number Ra_c as function of T_1 with T_2 as a parameter for $q_w = \text{constant}$	8
8. Comparison of $Ta \int 2(1-\mu)^4 \pi^4$ and $Ra \int 2\lambda^4 \pi^4$ vs λ	9
9. Illustration of the effect of maximum density in a melted water layer	10
10. Critical Rayleigh number as function of T_2	11
11. $Ra_c/(Ra_c)_{Bi=0}$ vs Bi in the case of $Ma = 0$	11
12. $Ra_c/(Ra_c)_{Ma=0}$ vs Ma in the case of $T_2 = 4^\circ\text{C}$	12
13. $Ra_c/(Ra_c)_{Ma=0}$ vs Ma in the case of $Bi = 0$	12
14. Comparison of experimental and analytical results	13
15. Schematic of the problem	14

	Page
16. Critical Grashof number Gr_c vs T_1	14
17. Critical melting thickness h_c and melting time t_c as function of step-wall temperature T_1	16
18. Velocity profiles in Regions I and III	17
19. Average coefficient of thermal expansion $\bar{\beta}$ vs T_1	18
20. Variation of wave speed, C_i vs T_1	18
21. Variation of wave number, a vs T_1	19
22. Example of wall temperature distribution with T_H and T_c consistently greater than T_m	20
23. Example of wall temperature distribution when T_H and T_c embrace T_m	20
24. Correlation of heat transfer results in water at temperatures above 4°C	21
25. The breakdown of the Nu and Ra_H correlation as T_m is approached	22
26. Schematic of the boundary layer regime in a vertical space filled with cold water at a mean temperature of 4°C	23
27. Correlation of heat transfer results in water at temperature near 4°C	24
28. Vertical annulus, coordinate system and thermal boundary conditions	25
29. Stream function and temperature contours	27
30. Effect of K on distribution of stream function and temperature	29
31. Effect of A on distribution of stream function temperature contour	30
32. Variation of Nu_i with K for $R' = 0.4$, $A = 1$	32
33. Variation of ratio of $Nu_i/(Nu_i)_{\text{cond}}$ for $R' = 0.4$, $A = 1$	32
34. Photographs and schematic views of flow patterns for $d_o = 121.5$ mm	33
35. Photograph and schematic view for $d_o = 65.5$ mm, $d_i = 19.0$ mm and $T_o = 8^\circ\text{C}$	35
36. Temperature profiles and local Nusselt numbers for $d_o/d_i = 3.20$ and $T_o = 4^\circ\text{C}$	36
37. Temperature profiles and local Nusselt numbers for $d_o/d_i = 1.75$, and $T_o = 6^\circ\text{C}$	37
38. Temperature profiles and local Nusselt numbers for $d_o/d_i = 3.44$ and $T_o = 8^\circ\text{C}$	38
39. Variation of Nu with ΔT (or T_o)	39
40. Streamlines and isotherms for $Ra_n = 2000$, $R'' = 2$	40
41. Angular velocity profiles for $Ra_n = 8000$ and $R'' = 2$	41
42. Streamlines and isotherms for $Ra_n = 8000$	42
43. Coefficient of convective heat transfer ϵ as function of γ' and R''	44
44. Variation of isotherms and streamlines as function of Ra_n , R'' and γ'	46
45. Variation of dimensionless temperature θ as function of dimensionless radius	48
46. Variation of overall Nusselt number \bar{Nu} with γ'	49
47. Comparison of Nu from Boussinesq model, full equation and viscosity model as function of T_1	50
48. Schematics of the square enclosure with thermal conditions	50
49. Dimensionless stream function for $Ra''' = 10^3$ with $R' = 0.4, 0.5, 0.55, 2/3$ and $3/4$..	52
50. Dimensionless stream function and temperature contours for $Ra''' = 10^4$ and 10^6 and $R' = 1/2$	54
51. Dimensionless stream function and temperature contours for $Ra''' = 10^4$ and 10^6 and $R' = 0.55$	55
52. Variation of Nu with R' using Ra''' as parameter	56
53. Variation of Nu with Ra''' using R' as parameter	56
54. Variation of dimensionless stream function for $R' = 1/2$	59
55. Variation of dimensionless stream function for $R' = 0.65$	60
56. Dimensionless first correction θ_1 as function of R' with $A = 1$	60
57. First correction to heat transfer Nu_2 as function of R'	61
58. Transient dimensionless streamlines	63

	Page
59. Transient dimensionless streamlines and isotherms	64
60. Transient dimensionless streamlines and isotherms	66
61. Transient dimensionless streamlines and isotherms	68
62. Transient dimensionless streamlines and isotherms	69
63. Transient dimensionless streamlines and isotherms	70
64. Transient dimensionless streamlines and isotherms	71
65. Transient dimensionless streamlines and isotherms	71
66. Schematic representation of the interdependence of stable and unstable regions with the thermal boundary conditions	72
67. Mean temperature profiles for melting from below	73
68. Mean temperature profiles for melting from above	74
69. The influence of melting and solidification on the heat transfer in thermal convection for large Prandtl numbers	77
70. Convective inversion for melting ice in water of temperature T_{∞}	78
71. Comparison of theoretical and experimental \overline{Nu} for unidirectional convection	78
72. Comparison of theoretical and experimental Nu for inverted regime	78
73. Nusselt number as function of Rayleigh number	80
74. Nusselt number variation with bulk temperature for approximately constant sphere diameters	81
75. Correspondence between the melting of flat plates and spheres of ice	81
76. Variation of mean Nusselt numbers with ambient temperature T_{∞}	82
77. Velocity profiles for $T_{\infty} = 2.0^{\circ}\text{C}$	82
78. Velocity profiles	83
79. Velocity profiles	84

TABLES

Table

1. Summary of experimental parameters and calculated results	8
2. Steady-state mean Nusselt numbers	57
3a. Maximum and minimum values of stream functions, with a constant temperature boundary	65
3b. Maximum and minimum dimensionless temperature, with a constant temperature boundary	65
4a. Maximum and minimum values of stream functions, with a constant temperature boundary	68
4b. Maximum and minimum dimensionless temperature, with a constant temperature boundary	68

NOMENCLATURE

a	wave number defined as $2\pi/\lambda$
A	defined as $(T_1 - T_m)/(T_1 - T_2)$, also aspect ratio H/W , H/D
Bi	Biot number, hd/k
C_i	wave speed, specific heat of ice
C_p	specific heat of water
D	gap width, depth, diameter
d	total layer depth, diameter
d_c	critical layer depth (depth at onset of convection)
d_f	final diameter
Fo	Fourier number, defined as α/L^2
g	gravitational acceleration
Gr_c	Grashof number, $g\gamma_1 T_1^2 h^3/\nu^2$ defined in eq 19
\overline{Gr}_c	modified Grashof number, $\beta_0 g T_1 h^3/\nu^2$ defined in eq 20
H	total layer depth ($= h$ when $T_2 \leq 4^\circ\text{C}$), also height
h	heat transfer coefficient, and also depth of unstable layer
h_c	critical unstable layer depth
k	thermal conductivity
K, R''	ratio of r_o/r_i
L	gap width ($= (d_o - d_i)/2$), also length or height
L_f	latent heat of fusion
Ma	Marangoni number defined as $\sigma_o \phi'(T_o - T_i)H/(\rho\nu\alpha)$
Nu	Nusselt number, defined as $q''D/k(T_h - T_c)$, also defined in eq 26
Nu_{loc}	Local Nusselt number defined in eq 50, 64 and 65.
$Nu(x)$	average Nusselt number over a vertical cross section defined in eq 72
\overline{Nu}	average Nusselt number, also average Nusselt number based on inner diameter defined in eq 51
\overline{Nu}	average Nusselt number defined as $\frac{1}{\pi} \int_0^\pi (Nu) d\phi$
p'	pressure
p	modified pressure defined as $p' + \rho_c gz$
P	dimensionless pressure defined as $pD^2/\rho_c \nu_c^2$
Pr	Prandtl number $c_p \mu/k$
q	local heat flux, also exponent defined in eq 37
q''	heat flux
Q	overall heat transfer rate
Q_t	total heat transfer rate per unit length
R_H	thermal resistance of hot-side boundary
R_c	thermal resistance of cold-side boundary
R'	density distribution parameter defined in eq 43 and eq 69 $(T_m - T_c)/(T_h - T_c)$
R''	radius ratio r_o/r_i
R	dimensionless radius, $(r - r_i)/L$, $(r - r_i)/(r_o - r_i)$ or $(r - r_i)/D$
R^+, R'''	dimensionless radial coordinate, r/L

Ra	Rayleigh number defined as in eq 1, also as $g\gamma L(T_h - T_c)^2/\nu\alpha$
Ra^*	Rayleigh number defined as $\bar{\rho}(\bar{\rho} - \rho(\theta'''))gD^3/\mu^2$
Ra_n	defined as $g\beta_2\gamma_i^3(T_i - T_o)^2/\nu\alpha$
Ra_c	critical Rayleigh number
\overline{Ra}_c	modified critical Rayleigh number defined as in eq 17 and 18
Ra_{ce}	experimental critical Rayleigh number defined in eq 11a and 11b
$Ra_{\eta H}$	hot-side Rayleigh number for fluid with density extremum defined in eq 36
$Ra_{\gamma c}$	cold-side Rayleigh number for fluid with density extremum defined in eq 36
Ra'	Rayleigh number defined in eq 42
Ra''	Rayleigh number defined as $g\beta_2\gamma_i^3(T_i - T_o)^2/\nu\alpha$
Ra'''	Rayleigh number defined as $g\rho_m\alpha_i L^3(T_h - T_c)^4/\rho_c\nu\alpha$
Ra_H	Rayleigh number defined in eq 27
Ra_G	Rayleigh number based on gap width defined as $g\beta_2(r_o - r_i)^3(T_i - T_o)/\nu\alpha$
S	shape factor defined in eq 96
St	Stefan number defined as $C_p(T_m - T_\infty)/L_f$
T	temperature
Ta	Taylor number
T_1	lower boundary temperature
T_2	upper boundary temperature
ΔT	temperature difference across the layer, $T_1 - T_2$, also $T_o - T_i$
T_m	temperature at maximum density
ΔT_{ce}	experimental critical temperature difference
ΔT_{ct}	theoretical critical temperature difference
T_h	hot wall temperature
T_c	cold wall temperature
T'	defined as $(T_h + T_c)/2$
T_{io}	initial ice temperature
T_o	temperature of outer cylinder
T_i	temperature of inner cylinder
\overline{T}_H	height-averaged hot wall temperature
\overline{T}_c	height-averaged cold wall temperature
T_{avg}	defined as $(\overline{T}_H + \overline{T}_c)/2$
T_s	surface temperature
T_a	ambient air temperature
T_i	ice temperature
T_{iv}	inversion temperature
T_r	reference temperature
T_∞	bulk water temperature
t	time
t_c	critical time, critical melting time
u	radial velocity
v	axial velocity, angular velocity
U	dimensionless radial velocity uD/ν_c , uL/α
V	dimensionless axial velocity and angular velocity, vD/ν_c and vL/α

\bar{U}	dimensionless mean-base flow velocity
W	width
x, y, z	coordinates
X, Y, Z	dimensionless coordinates defined as x/D , x/L , y/D , y/L and z/D .

Greek letters

β	volumetric coefficient of expansion
β_1, β_2	coefficient of expansion evaluated at T_1 and T_2 , also coefficient defined in eq 54
β_o	coefficient defined in eq 21
$\bar{\beta}$	mean volumetric coefficient of expansion defined as $1/T_1 \int_0^{T_1} \beta(T) dT$
$\beta'_1, \beta'_2, \beta'_3, \beta'_4$	coefficients defined in eq 61
$\beta''_1, \beta''_2, \beta''_3$	coefficient defined in eq 97a
μ	viscosity, ratio of angular velocity (Ω_2/Ω_1)
ν	kinematic viscosity
α	thermal diffusivity
α_1	coefficient defined in eq 37
ρ	density
ρ_r	reference density
ρ_m	maximum density
$\bar{\rho}$	average density
γ	coefficient defined in eq 2
γ_1, γ_2	coefficient defined in eq 4
γ'	inversion parameter defined as $-2(T_m - T_o)/(T_o - T_i) (= -2R')$
λ_1, λ_2	thermal parameters defined in eq 6 and 7
Ω	angular velocity, also dimensionless vorticity $\omega L^2/\alpha$
δ_H	scale of hot-side boundary layer thickness defined by eq 32
δ_c	scale of cold-side boundary layer thickness defined by eq 33
ϕ	angular function from vertical axis
ϕ'	linear coefficient of density-temperature relation
θ	dimensionless temperature defined as $(T - T_i)/(T_o - T_i)$ or $(T - T_c)/(T_h - T_c)$
θ'	defined as $(T - T_o)/(T_i - T_o) = 1 - \theta$
θ''	defined as $(T - T')/(T_h - T')$
θ'''	defined as $(T - T_a)/(T_o - T_a)$
θ''''	defined as $(T - T_s)/(T_o - T_s)$
ε	coefficient of heat transfer coefficient defined in eq 55
ξ, ω	vorticity
$\bar{\xi}$	dimensionless vorticity, $\bar{\xi} L^2/\nu$
$\bar{\Psi}$	stream function
ψ	dimensionless stream function $\bar{\psi}/\nu$

Subscripts

<i>a</i>	ambient
1, 2	lower, upper also inner and outer
<i>i</i>	inner
<i>c</i>	critical, cold
<i>loc</i>	local
<i>h, H</i>	hot
<i>avg</i>	average
<i>iv</i>	inversion
<i>s</i>	surface
<i>m</i>	maximum
<i>r</i>	reference
<i>o</i>	outer, initial and reference
∞	bulk
<i>f</i>	final

Natural Convection Heat Transfer in Water Near its Density Maximum

YIN-CHAO YEN

INTRODUCTION

The most comprehensive treatment of cold regions heat transfer processes is given by Lunardini (1981, 1988). He discusses the mechanisms of frost heave and their relation to soil composition and properties, methods of calculating or approximating the extent of ground freezing and thawing with uniform or variable thermal properties, and transfer processes associated with structures in cold climates. In contrast, this monograph deals exclusively with the phenomena arising from the density anomaly of water that is formed by melting ice in either an ice-water system or in single-phase water that encompasses the density extremum. The effect of this density anomaly on the onset of convection (i.e., thermal instability), the transient and steady temperature structure within the water layer, and the associated heat transfer rate will be examined and summarized in various geometrical arrangements.

GENERAL DESCRIPTION OF RAYLEIGH INSTABILITY

For fluids not undergoing phase change or density inversion, the magnitude of the Rayleigh number is the criterion commonly used to determine if natural convection is significant:

$$Ra = \frac{g\beta(\Delta T)d^3}{\nu\alpha} \quad (1)$$

where β = the coefficient of expansion
 ν = the kinematic viscosity
 α = the thermal diffusivity of the fluid
 d = the depth of the fluid layer
 g = the gravitational acceleration
 ΔT = the temperature difference across the liquid layer.

β , ν and α are usually evaluated at the arithmetic average of lower and upper boundary temperatures. For normal fluids with density decreasing with increasing temperature, it has been determined analytically and confirmed experimentally that the liquid will go into motion at a Rayleigh number of about 1708 for both lower and upper rigid boundaries and constant temperatures.

The ice–water system, in which the water accumulates continuously by melting from below, forms in the lower part of the system, and is subject to a negative temperature gradient, resembles the classical Rayleigh problem. However, the melting system differs fundamentally in a number of ways from that of the classical Rayleigh problem: 1) for an ice–water system, water may not act as a normal fluid because of its peculiar properties of density inversion at 4°C; therefore, ideally, a stable and unstable region may exist simultaneously in the water layer, 2) the upper boundary (water/ice interface) is moving upward as melting progresses so that it can be considered neither a rigid nor a free boundary, and 3) though both boundaries are maintained at fixed temperatures, the upper boundary is moving; therefore, a time-dependent temperature gradient exists across the layer.

For the case of the ice–water system, with the water layer formed by melting ice from above, the water layer will be situated over the remaining ice. For normal fluids, the system will always be stable. However, in the case of water near the water/ice interface, there exists a region with a positive density and temperature gradient directed away from the interface. This is a system equivalent to the case of a water layer heated above ($\geq 4^\circ\text{C}$) and cooled below at 0°C in which a stable region will sit on an unstable region. A convective motion is thus created in the layer for both cases, involving either phase change (i.e., in a ice–water system) or a single phase (i.e., in water alone), either when 1) the lower is maintained at 8°C (i.e., heating from below) and the upper boundary is at 0°C (equivalent to the case of melting from below), or 2) the upper boundary is maintained at 8°C and the lower is at 0°C (equivalent to melting from above). When the value of β in eq 1 is evaluated at $8/2 = 4^\circ\text{C}$ [$\beta = 1/\rho (\partial\rho/\partial T)_{4^\circ\text{C}} = 0$], one may face the contradictory situation of observing convection with $Ra=0$, which violates the classical stability criterion.

EFFECT OF 4°C WATER ON ONSET OF CONVECTION

In a confined horizontal layer

When a layer of liquid whose density decreases monotonically with the increase of temperature is subject to an adverse temperature gradient (say $T_1 > T_2$ where subscripts 1 and 2 refer to lower and upper surfaces, respectively) the system is potentially unstable because it is top-heavy. The onset of convection is indicated if the Rayleigh number exceeds its critical value. For normal fluid, the Rayleigh number is defined as in eq 1.

A somewhat complicated situation arises if the liquid possesses a maximum density within the temperature range between T_1 and T_2 (such a situation could exist either in a water layer formed by melting ice, i.e., ice–water system, or in a water layer by maintaining the boundary layer temperatures in such a manner that a maximum density will exist within the layer). In such a case, the liquid density increases upward from the lower surface until it reaches a maximum and decreases afterward. Therefore, only part of the liquid layer is potentially unstable. Furthermore, the onset of convection is possible with both heating from below and above.

For liquids with a density–temperature relationship expressed by

$$\rho = \rho_m [1 - \gamma (T - T_m)^2] \quad (2)$$

Veronis (1963), Debler (1966) and Tien (1968) all have found that the critical Rayleigh number is dependent upon the temperature difference ratio defined as $A = (T_1 - T_m)/(T_1 - T_2)$ with the Rayleigh number given by

$$Ra = \frac{2\gamma (T_1 - T_m) g (T_1 - T_2) d^3}{\nu \alpha} \quad (3)$$

where γ is the temperature coefficient of eq 2, and T_m is the temperature corresponding to maximum density.

The major limitation of these earlier works is that the particular temperature–density relationship used has only a limited range of applicability. For the case of water, the representation of the temperature–density relation by a parabolic expression is only valid for the temperature range from 0° to 8°C. The other limitation was that these investigations were restricted to the special case of two rigid boundary surfaces.

Sun et al. (1969) extended these earlier works by representing the density–temperature relationship with

$$\rho = \rho_m [1 - \gamma_1 (T - T_m)^2 - \gamma_2 (T - T_m)^3] \quad (4)$$

which was found to be valid for water temperature from 0° to 30°C. They also broadened their investigation by including the rigid–free hydrodynamic boundary, in addition to rigid–rigid boundary. Using the classical stability analysis, they derived a new Rayleigh number as

$$Ra = \frac{2\gamma_1 Ag (\Delta T)^2 d^3 \left(1 + \frac{3}{2} \frac{\gamma_2}{\gamma_1} A \Delta T\right)}{v\alpha} \quad (5)$$

in terms of thermal parameters

$$\lambda_1 = \left(-\frac{1}{A}\right) \left[\frac{1 + 3 \frac{\gamma_2}{\gamma_1} A \Delta T}{1 + \frac{3}{2} \frac{\gamma_2}{\gamma_1} A \Delta T} \right] \quad (6)$$

and

$$\lambda_2 = \left(\frac{1}{A^2}\right) \left[\frac{\frac{3}{2} \frac{\gamma_2}{\gamma_1} A \Delta T}{1 + \frac{3}{2} \frac{\gamma_2}{\gamma_1} A \Delta T} \right]. \quad (7)$$

The critical Rayleigh number has been computed for the range of $-4.25 < \lambda_1 < -0.5$ and $-1.4 < \lambda_2 < 1.6$. For the special case $\lambda_2 = 0$ (equivalent only to the parabolic density–temperature relation, where γ_1 is only a function of the temperature difference ratio A since $\gamma_2 = 0$), the critical Rayleigh number for both rigid–free and rigid–rigid boundary conditions is shown in Figure 1. The effect of λ_2 on Ra_c is shown in Figures 2 and 3, respectively, for rigid–free and rigid–rigid boundaries.

It can be seen from Figure 1, that for $\lambda_1 \geq -1.75$, the values of $(Ra_c)_{\lambda_2=0}$ are nearly equal to each other for the conditions of rigid–free and rigid–rigid boundaries.

Chandrasekhar (1961) derived, for the use of rigid–rigid boundary, the asymptotic expression for Ra_c as

$$Ra_c \sim 1,186 \left(\frac{1}{A}\right)^4 \quad (8)$$

in terms of the work reported by Sun et al. (1969). Equation 8 then becomes

$$Ra_c \sim 1,186 (\lambda_1)^4, \text{ for } \lambda_2 = 0. \quad (9)$$

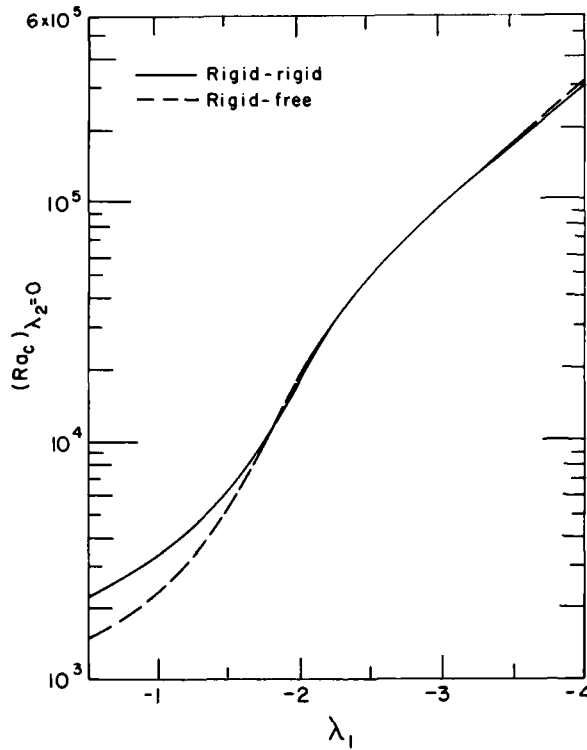


Figure 1. Critical Rayleigh number for $\lambda_2 = 0$ (after Sun et al. 1969).

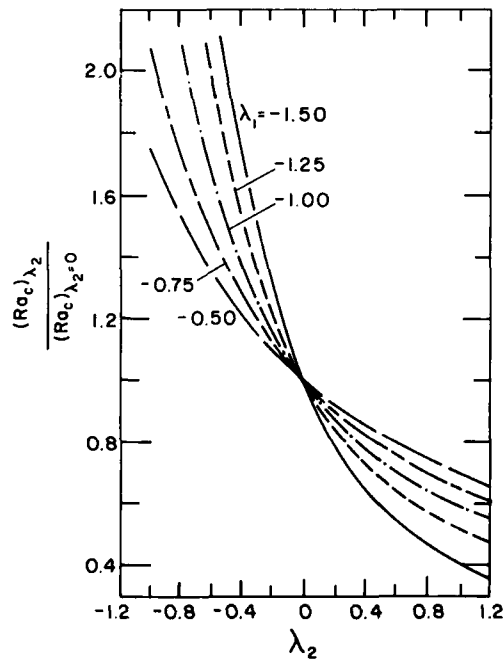


Figure 2. $(Ra_c)_{\lambda_2} / (Ra_c)_{\lambda_2=0}$ vs λ_2 with λ_1 as parameter for rigid-free case (after Sun et al. 1969).

Though the above approximation is obtained for the rigid-rigid surfaces, this is expected to hold true for rigid-free surfaces and for the case of melting from below. There is no proof in the case of melting from above, where the unstable region is above the moving water/ice interface. For a layer of maximum density fluid subject to temperatures from above and below, which are on either side of the maximum density temperature, the density of the fluid first increases upward from the lower surface to a maximum then decreases. The fluid layer, therefore, consists of a potentially unstable layer (with a height of Ad) and a stable layer. The upper boundary effect (i.e., one with free or rigid upper surfaces)

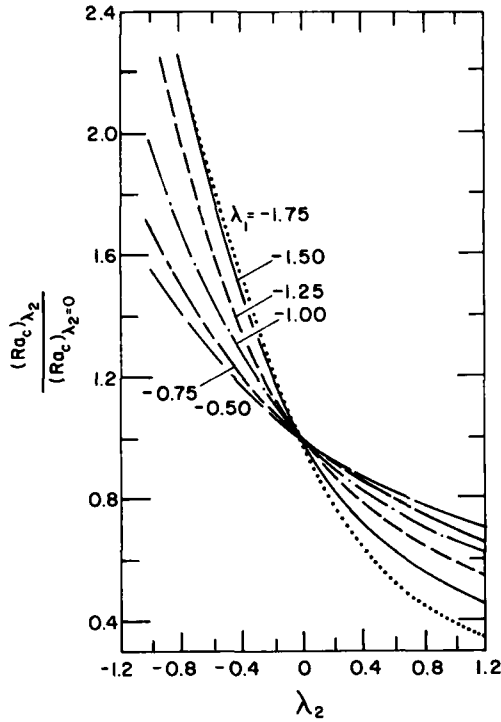


Figure 3. $(Ra_c)_{\lambda_2} / (Ra_c)_{\lambda_2=0}$ vs λ_2 with λ_1 as parameter for rigid-rigid case (after Sun et al. 1969).

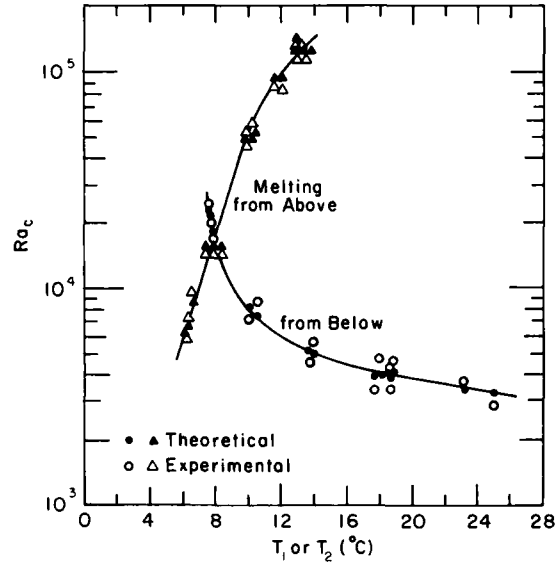


Figure 4. Ra_c as function of T_1 or T_2 (after Sun et al. 1969).

is felt only indirectly by the potentially unstable layer. This boundary effect would become less significant as the relative thickness of the stable layer to that of the potentially unstable layer increases, which corresponds to a decreasing value of A or an increasing value of $-\lambda_1$ (see Fig. 1). For the limiting case where $A \rightarrow 0$, $T_1 = T_m$, and the fluid layer is always stable. Figure 4 completely supports this argument. Although the curve for the rigid-rigid case differs from that of rigid-free case for small values of $(-\lambda_1)$, both curves approach the same asymptotic condition for $(-\lambda_1) > 3.0$ and become indistinguishable. The asymptotic expression is found to be

$$(Ra_c)_{\lambda_2=0} \sim 1,177 (\lambda_1)^4. \quad (10)$$

This is essentially the same as eq 9, with a less than 1% difference in coefficient which, in all probability, can be attributed to errors introduced in the numerical computations.

Experimental verification

Yen (1968), Yen and Galea (1969), Sun et al. (1969) and Yen (1980) verified the above findings by performing melting experiments in both melting modes (i.e., melting from below and above). In both cases, bubble-free ice was fabricated, and the melting system was maintained airtight (any trace of air trapped in the water/ice interface would drastically affect the melting mechanism). In these experiments the onset of convection was found either by determining the inflection point on the melting front vs time plot or by determining the time where the steep jump in the temperature gradient of the stable region occurred. If the values of T_1 ($T_1 > 0^\circ\text{C}$, melting from below) and T_2 ($T_2 > 0^\circ\text{C}$ melting from above) and the critical layer depths determined by either of the mentioned methods (i.e., inflection point or sudden jump in the temperature gradient) are known, the experimental critical Rayleigh number can be found from

$$Ra_{ce} = \frac{(2\gamma_1 T_m T_2 g d_c^3) \left(1 - \frac{3}{2} \frac{\gamma_2}{\gamma_1}\right) T_m}{v\alpha} \quad (11a)$$

for melting from above. The corresponding values of λ_1 and λ_2 are given by

$$\lambda_1 = \left(-\frac{T_2}{T_m} \right) \left[\frac{\left(1 - 3 \frac{\gamma_2}{\gamma_1} T_m \right)}{\left(1 - \frac{3}{2} \frac{\gamma_2}{\gamma_1} T_m \right)} \right] \quad (12a)$$

and

$$\lambda_2 = \left(\frac{T_2}{T_m}\right)^2 \left[\frac{\left(1 - 3 \frac{\gamma_2}{\gamma_1} T_m\right)}{\left(1 - \frac{3}{2} \frac{\gamma_2}{\gamma_1} T_m\right)} \right] \quad (13a)$$

to compute the theoretical critical Rayleigh number. For melting from below, the value of Ra_{ce} is found from

$$Ra_{ce} = \frac{\left[(2\gamma_1 T_1 g a_c^3) (T_1 - T_m) \left(1 + \frac{3}{2} \frac{\gamma_2}{\gamma_1} \right) (T_1 - T_m) \right]}{\nu \alpha} \quad (11b)$$

with the corresponding values of λ_1 and λ_2 as

$$\lambda_1 = \left(-\frac{T_1}{T_1 - T_m} \right) \left[\frac{1 + 3 \frac{\gamma_2}{\gamma_1} (T_1 - T_m)}{1 + \frac{3}{2} \frac{\gamma_2}{\gamma_1} (T_1 - T_m)} \right] \quad (12b)$$

and

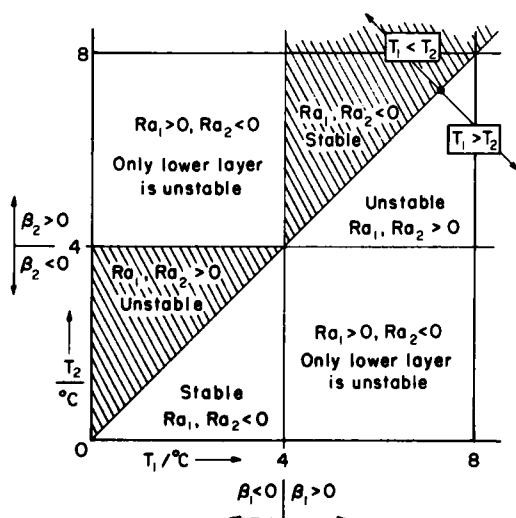


Figure 5. Principal stability diagram (after Merker et al. 1979).

$$\lambda_2 = \left(\frac{T_1 - T_m}{T_1} \right)^2 \left[\frac{\frac{3}{2} \frac{\gamma_2}{\gamma_1} (T_1 - T_m)}{1 + \frac{3}{2} \frac{\gamma_2}{\gamma_1} (T_1 - T_m)} \right]. \quad (13b)$$

The experimental values of Ra_{ce} from eq 11a and eq 11b are compared with Ra_{ct} values obtained by using λ_1 and λ_2 values from eq 12 and 13 in conjunction with Figures 1 and 3. The comparison is shown in Figure 4. Within the experimental error in determining the critical layer depth d_c (which is exemplified by its presence as d_c^3 in eq 11a and 11b), it can be concluded that Ra_{ce} and Ra_{ct} are nearly in complete agreement.

The other comprehensive analysis of the onset of convection (i.e., critical Rayleigh number) in a water layer encompassing the density anomaly was reported by Merker et al. (1979). In their study, the density-temperature relation of water was approximated by three different polynomials having two, three and five terms. Linear stability analysis was used and the resulting perturbation equations were solved with the aid of Galerkin's method. Figure 5 is a general diagram of regions, in which the fluid is purely stable, unstable or only unstable at the lower layer, according to the imposed boundary temperatures of T_1 and T_2 . β_1 and β_2 are the coefficients of thermal expansion evaluated at T_1 and T_2 , respectively, and the values of Ra_1 and Ra_2 are the corresponding Rayleigh numbers defined as in eq 1 with $\Delta T = T_1 - T_2$. Ra_1 is always defined as positive if the layer is unstably stratified, whereas Ra_2 changes sign. Therefore Ra_1 was used by Merker et al. (1979) to describe the layer stability.

Figure 6 shows the critical Rayleigh number variation with T_1 in the case of constant boundary temperature (i.e., $T_w = \text{constant}$) with the density-temperature relation represented by a polynomial of order $p = 5$ and $n = 7$ (number of Galerkin terms). Figure 7 shows the case of constant wall heat flux density (i.e., $q_w = \text{constant}$). Both figures show that in the region below the isotherm $T_2 = 4^\circ\text{C}$, the water layer has a density profile with no maximum value; i.e., the layer is completely unstably stratified. For this case, the bending of the density profile is weak, and accordingly, the effect on the critical Rayleigh number is small. The calculated Ra_c values are between 1708 and 3600 for $T_w = \text{constant}$ and below 720 and 1600 for $q_w = \text{constant}$. The region above the isotherm $T_2 = 4^\circ\text{C}$ refers to a density profile with maximum value; i.e., only a part of the layer is unstably stratified. The nonlinearity of the density profile is strong and the effect on Ra_c is great. The Ra_c values are significantly larger than those obtained from the classical problem. The usage of Figure 6 or 7 can be delineated by considering the following cases:

1. If the temperature $T_2 < 4^\circ\text{C}$ (say $T_2 = 0^\circ\text{C}$) then cooling this water layer with $T_1 < 0^\circ\text{C}$ from below results in an unstable stratification where the bending of the profile is weak. The water layer is stable if heated from below with temperature $0 \geq T_1 \geq 4^\circ\text{C}$ and it becomes partially unstable if T_1 exceeds 4°C . The density profile then includes the maximum density and the bending of the profile is strong.

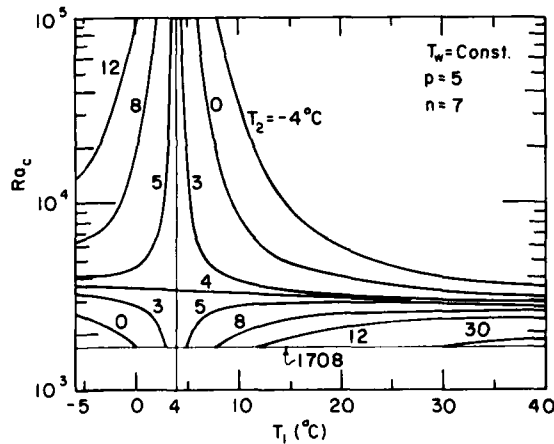


Figure 6. Critical Rayleigh number Ra_c as function of T_1 with T_2 as a parameter for T_w (wall temperature) = constant (after Merker et al. 1979).

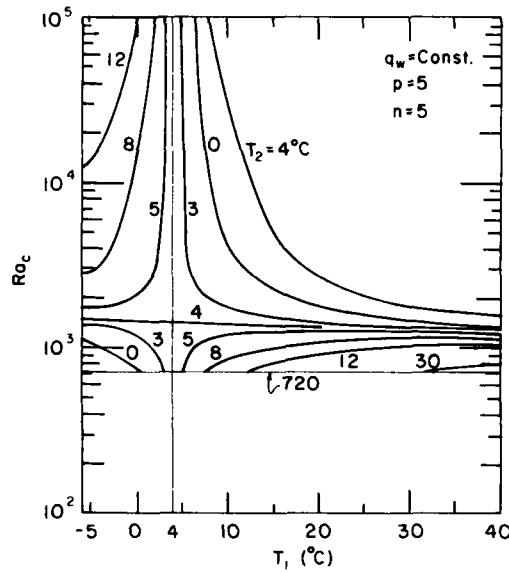


Figure 7. Critical Rayleigh number Ra_c as function of T_1 with T_2 as a parameter for q_w (constant wall flux) = constant (after Merker et al. 1979).

2. If T_2 is kept at $T_2 > 4^\circ\text{C}$ (say $T_2 = 8^\circ\text{C}$) then cooling this water from below with $T_1 < 4^\circ\text{C}$ results in the upper part between the upper boundary and the 4°C isotherm remaining stable, whereas the lower part becomes unstable. The strong bending of the profile affects the Rayleigh number considerably. The layer is stable if cooled with temperature T_1 between 4 and 8°C , and is unstably stratified if heated from below with $T_1 > 8^\circ\text{C}$.

For constant wall temperature and rigid boundary conditions, this study should be comparable to that of Sun et al. (1969) even though the Rayleigh number is defined here classically (except that β is evaluated at the lower boundary temperature or T_1) and that of Sun et al. (1969) is defined by eq 5. For $T_1 = 10^\circ\text{C}$ and $T_2 = 0^\circ\text{C}$ (i.e., the case of melting from below) the values of λ_1 and λ_2 are 1.527 and 0.217, respectively, based on eq 12b and 13b. In Figures 1 and 3, the Ra_c value was found to be $\sim 8,200$. Under the same conditions of T_1 and T_2 , based on Figure 6, Ra_c is found to be $\sim 8,150$. For the case of melting from above (i.e., for the case $T_1 = 0^\circ\text{C}$), and $T_2 = 10.5^\circ\text{C}$, based on eq 12a and 13a, the values of $\lambda_1 = 1.644$ and $\lambda_2 = 0.300$ were obtained with the aid of Figures 1 and 3, Ra_c is found to be $Ra_c = 48,200$, which compares remarkably well with $Ra_c = 47,520$ estimated from Figure 6. It is clear that regardless of how you define the Rayleigh number (as long as done appropriately), the equations will provide the same Ra_c for the same thermal boundary conditions.

Legros et al. (1974) were the first ones to investigate systematically the effect of the ratio d/h (where d is total layer depth, h is height of the unstable layer) on the onset of convection of a water layer with

Table 1. Summary of experimental parameters and calculated results (after Legros et al. 1974).

T_2 (°C)	d (mm)	h (mm)	$d-h$ (mm)	d/h	ΔT_{ce} (°C)	T_2 (°C)	d (mm)	$d-h$ (mm)	ΔT_{ce} (°C)
0.54	4.67	3.17	1.50	1.47	10.80	4.32	4.67	-0.23	6.62
0.86	4.67	3.27	1.40	1.42	10.46	5.18	4.67	-0.96	5.75
1.31	4.67	3.39	1.28	1.38	9.84	6.51	4.67	-2.47	4.75
1.67	4.67	3.51	1.16	1.33	9.40	9.05	4.67	-6.94	3.40
2.17	4.67	3.70	0.97	1.27	8.80	13.33	4.67	-19.90	2.19
2.56	4.67	3.85	0.82	1.21	8.24	16.84	4.67	-34.66	1.73
3.40	4.67	4.29	0.38	1.09	7.38	20.16	4.67	-55.90	1.35

a maximum density as a function of the upper boundary temperature (i.e., T_2). In their experiment, T_2 was varied from 0.54° to 20.16°C, and the layer depth was fixed at 0.467 cm. The critical temperature difference (ΔT_{ce}) was determined by observing the temperature difference as a function of heat flux. Table 1 is a summary of their results.

In Table 1, $d-h = d/\Delta T_{ce} (4 - T_2)$, (i.e., the stable layer depth just prior to onset of convection). For $T_2 > 4^\circ\text{C}$, the measured ΔT_{ce} values were compared with the analytical ΔT_{ct} values calculated from the classical critical Rayleigh number, i.e.,

$$\frac{g\beta\Delta T_{ct} d^3}{\nu\alpha} = 1708 \quad (14)$$

or

$$\Delta T_{ct} = \frac{(1708) (\nu\alpha)}{g\beta d^3} . \quad (15)$$

The β value was evaluated from a sixth-order polynomial: i.e.,

$$\rho = aT^6 + bT^5 + cT^4 + dT^3 + eT^2 + fT + g ,$$

where $a = 8.2270200 \times 10^{-13}$,
 $b = 6.8247601 \times 10^{-11}$,
 $c = 2.9114740 \times 10^{-9}$,
 $d = 1.2488637 \times 10^{-7}$,
 $e = -9.2582184 \times 10^{-6}$,
 $f = 6.8355321 \times 10^{-5}$,
 $g = 9.9984055 \times 10^{-1}$,

and was found to be in excellent agreement. The difference $\Delta T_{ce} - \Delta T_{ct}$ becomes greater when $T_2 \rightarrow 4^\circ\text{C}$, as expected. For the experiments of $T_2 < 4^\circ\text{C}$, the results were compared using an analogy pointed out by Veronis (1963) and Debler (1966) between the eigenvalues for the Benard problem with a maximum density and for the stability of viscous flow between two cylinders rotating at almost the same angular velocity. This is shown in Figure 8 along with the work reported by Yen (1980) from melting ice studies. Yen's data not only agree extremely well with those of Veronis (1963) and Legros

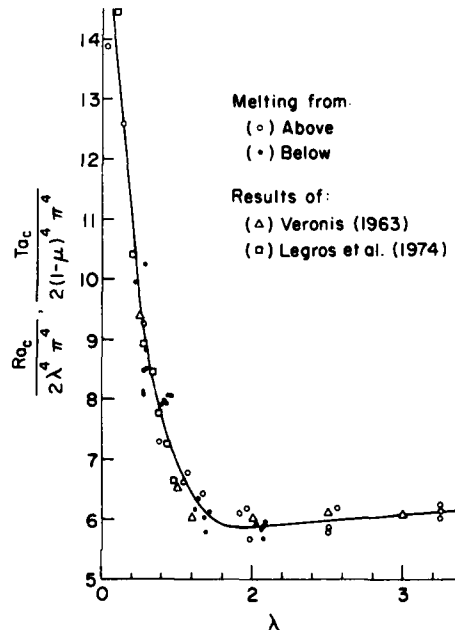


Figure 8. Comparison of $Ta_c/2(1-\mu)^4\pi^4$ and $Ra_c/2\lambda^4\pi^4$ vs λ (after Yen 1980).

et al. (1974) but the data extended Legros et al.'s range of λ from about 1.5 to 3.5. In this figure, the value of Ra_c is evaluated from

$$Ra_c = \frac{g\gamma (\Delta T)^2 h_c^3}{v\alpha} \quad (16)$$

where γ is obtained from eq 2 and has a value of $7.68 \times 10^{-6} \text{C}^{-2}$ with $\rho_m = 0.999973 \text{ g/cm}^3$, and v and α are evaluated at $(T_1 + T_2)/2$. In Yen's melting ice work, $\Delta T = 4^\circ\text{C}$ and $h_c = 4/T_2(d_c)$ for melting above and $\Delta T = T_1 - 4^\circ\text{C}$ and $h_c = [(T_1 - 4)/T_1] d_c$ for melting from below, where d_c is the total layer depth at the onset of convection.

In a melt layer with a free surface

Seki et al. (1977) performed an experimental and analytical study on the thermal instability program arising from a horizontal layer of ice heated from above under constant radiant heat flux. Two cases were considered, as indicated in Figure 9. In the case of (a), the fluid density in the layer increases at first downward from the free surface and then decreases (equivalent to melting from above with constant upper boundary $T_2 = \text{constant}$). Therefore, the fluid layer consists of potentially stable and unstable layers. On the other hand, in the case of (b), the entire layer is unstable. In the case of (a), the hydrodynamic boundary conditions, including surface tension and the thermal boundary conditions, are only felt indirectly by the potentially unstable layer. If the thickness of the stable layer decreases relative to that of the unstable one, it is obvious that these effects would become more significant. In case of (b), these effects are felt directly by the potentially unstable layer. The problem, which incorporates a maximum density and an upper free surface, differs distinctly from other instability problems.

In Seki et al.'s (1977) analysis, linear perturbation techniques are used to derive a sixth-order differential equation and the series-solution method is utilized to obtain an eigenvalue equation for the case where the lower surface is kept at 0°C and the upper free surface is subjected to temperatures ranging from 1.5° to 12°C . Figure 10 shows the variation of the critical Rayleigh number Ra_c with T_2 for $Ma = 0$ (Ma is the Marangoni number). Two solid lines were shown. One for $Bi = 0$ (Biot number $= hH/K$) corresponds to a fixed heat flux and the other for $Bi = \infty$ to a fixed temperature at the free surface. Also shown are the results of Sun et al. (1969). It appears that Ra_c values increase with T_2 . However, the two curves intersect each other at $\sim 6.2^\circ\text{C}$, and the reason for this occurrence is still not understood. (This phenomenon was also observed in Sun et al.'s study; see Fig. 1.) The effect of Bi on Ra_c is demonstrated through the plot of $Ra_c/(Ra_c)_{Bi=0}$ vs Bi for various T_2 for $Ma=0$ (see Fig. 11). It is clear that the effect is greatest for fixed surface temperature and smallest for fixed heat flux. But the sensitivity to Bi varies considerably; it decreases with increasing T_2 , indicating that the effect

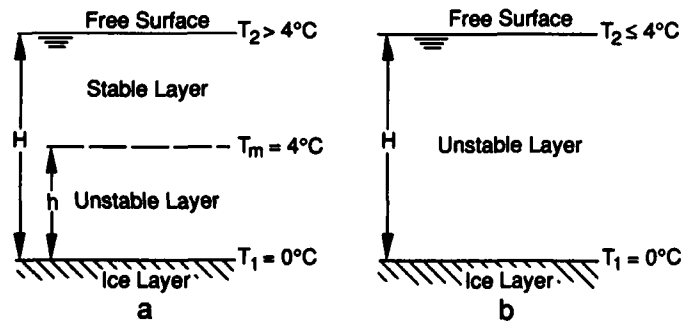


Figure 9. Illustration of the effect of maximum density in a melted water layer (after Seki et al. 1977).

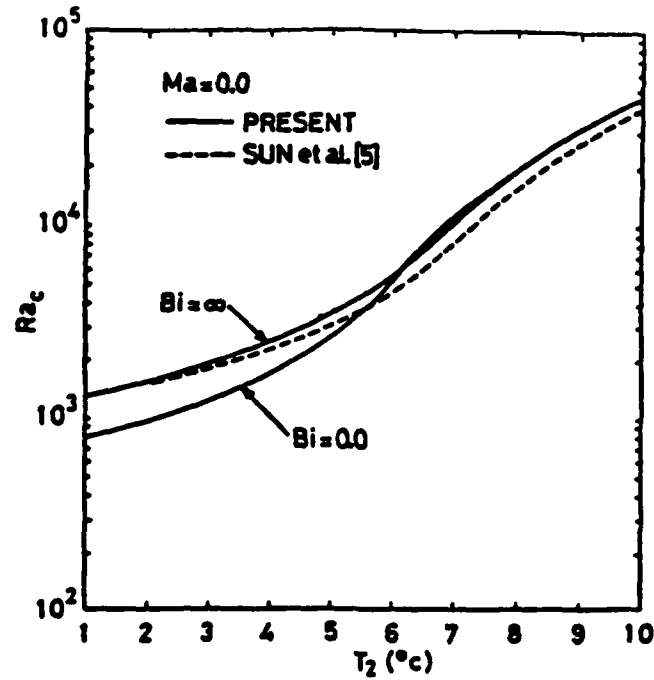


Figure 10. Critical Rayleigh number as function of T_2 (Seki et al. 1977).

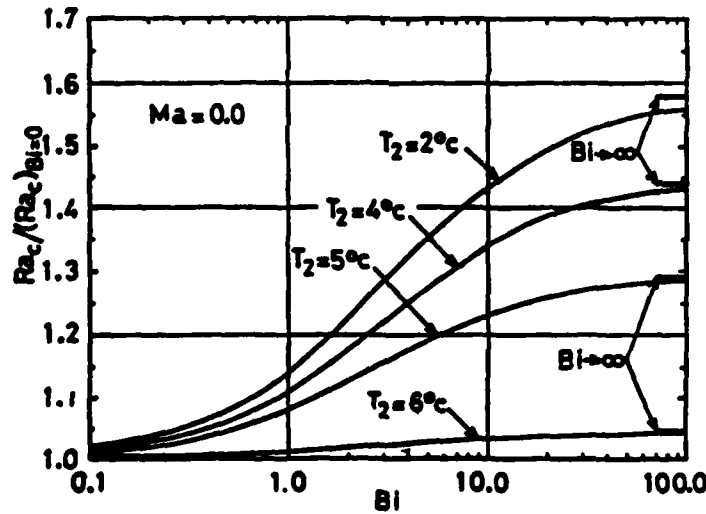


Figure 11. $Ra_c / (Ra_c)_{Bi=0}$ vs Bi in the case of $Ma = 0$ (Seki et al. 1977).

becomes less significant as the thickness of the stable layer increases. The effect of Ma on the ratio of $Ra_c / (Ra_c)_{Ma=0}$ vs Ma for various Bi values and $T_2 = 4^\circ\text{C}$ is shown in Figure 12. Clearly the effect of thermal boundary condition at the free surface on the onset of free convection for a given Ma is greatest for $Bi = 0$ and smallest for $Bi = \infty$.

The dependence of $Ra_c / (Ra_c)_{Ma=0}$ on Ma is shown in Figure 13 with $Bi = 0$ and various T_2 values. $Ra_c / (Ra_c)_{Ma=0}$ increases monotonically with increasing Ma and is most sensitive to Ma in the range of 100–1000. The value of T_2 markedly influences the effect of Ma on Ra_c . For $T_2 > 4^\circ\text{C}$, the thickness of the potentially stable layer in the melted water layer increases as T_2 increases; therefore, the thermal

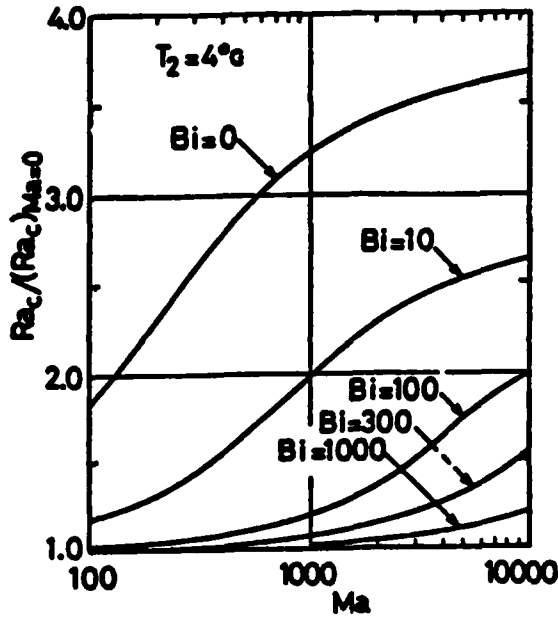


Figure 12. $Ra_c / (Ra_c)_{Ma=0}$ vs Ma in the case of $T_2 = 4^\circ\text{C}$ (Seki et al. 1977).

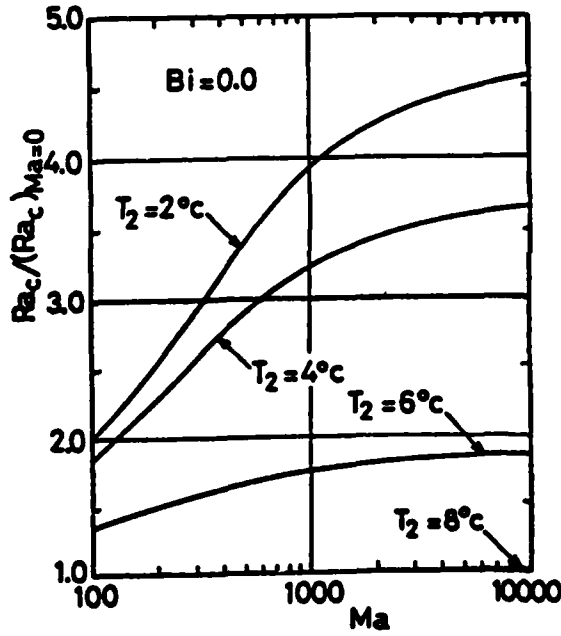


Figure 13. $Ra_c / (Ra_c)_{Ma=0}$ vs Ma in the case of $Bi = 0$ (Seki et al. 1977).

boundary condition of the free surface becomes less significant as T_2 increases and the effect of Ma on Ra_c is reduced. However, the effect of Ma on Ra_c still can be evaluated even at $T_2 > 4^\circ\text{C}$. This behavior may be attributed to the upward penetration of the free convective motion in the unstable layer exceeding the 4°C isotherm. Figure 14 shows the comparison of experimental and analytical results, in which Seki et al. (1977) evaluated the $\overline{Ra_c}$ value based on

$$\overline{Ra_c} = g\beta (T_m - T_1) h^3 / \nu\alpha \quad (17)$$

for $T_2 > 4^\circ\text{C}$ and

$$\overline{Ra_c} = g\beta (T_2 - T_1) H^3 / \nu\alpha \quad (18)$$

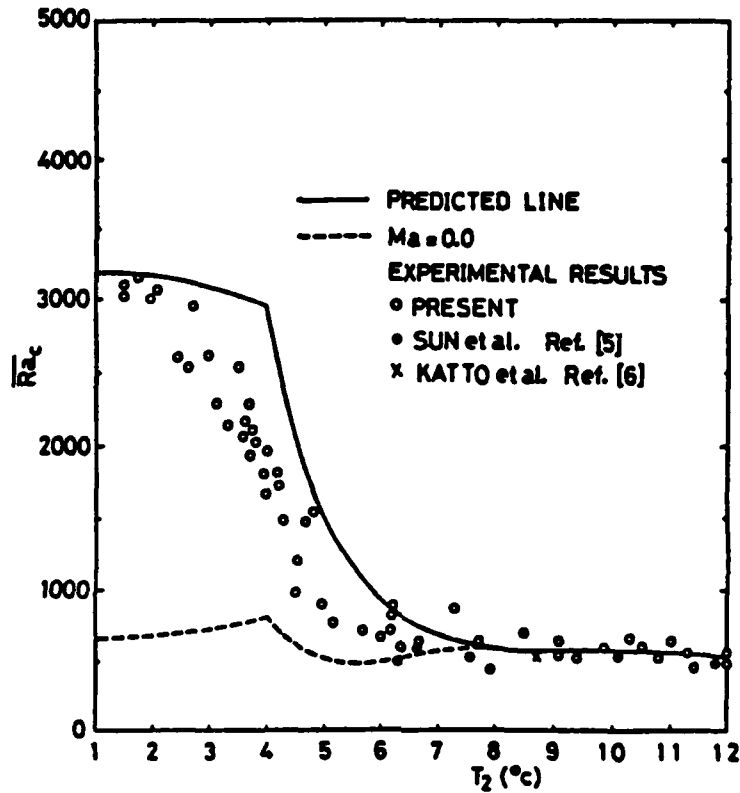


Figure 14. Comparison of experimental and analytical results (Seki et al. 1977).

for $T_2 \leq 4^\circ\text{C}$. β , ν , and α are evaluated at 2°C in eq 17 and evaluated at the arithmetic mean temperature in eq 18. It can be concluded that for $T_2 < 8^\circ\text{C}$, $Ra_c \sim 500$ agreed extremely well with the experimental results of Sun et al. (1969).

In a melt layer between vertical plates

The only analytical and experimental work dealing with the onset of convection of a vertical water layer formed by melting ice was reported by Hassab and Sorour (1982). Their problem deals with the melting of an ice layer that is confined inside a vertical slender slot as shown in Figure 15. Initially the ice is at its melting temperature (i.e., $T = 0^\circ\text{C}$) at $t = 0$, then the left side is suddenly increased to a constant temperature $T_1 > 0^\circ\text{C}$ and maintained at that value throughout the entire experiment. When the melt layer is thin, the heat is transferred by conduction (except at the ends) and consequently a laminar parallel flow will be developed as a result of ice density difference in the fluid. As the melt layer thickness gradually increases with time, the initial laminar motion breaks up, and secondary flow appears in the form of either stationary horizontal cells or traveling waves.

The stability problem was solved by the application of the Galerkin method, and the stability criteria of this system are established by determining its eigenvalue, $C_n = C_r + iC_i$ (where C_i = wave speed, $n = 1, 2, \dots, N$). That is, for a given choice of the system parameter T_1 , there are at least two minimum values of Gr (Grashof number) with respect to a wave number ($2\pi/\lambda$, where λ is the wavelength) for either the real part of the least eigenvalue $C_r = 0$, $C_i \neq 0$, in the case of traveling waves, or for both components $C_r = C_i = 0$ in the case of stationary cells. Figure 16 shows the critical Grashof number along with the modified Grashof number Gr_c as a function of T_1 . The values of Gr_c and \overline{Gr}_c are defined respectively as

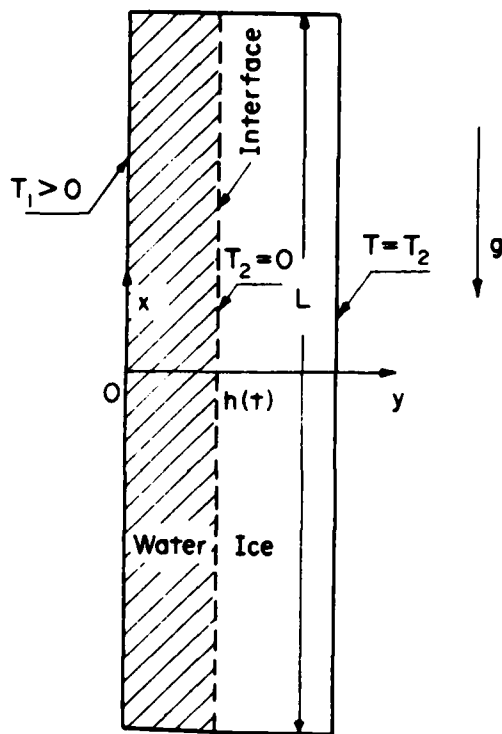


Figure 15. Schematic of the problem (Hassab and Sorour 1982).

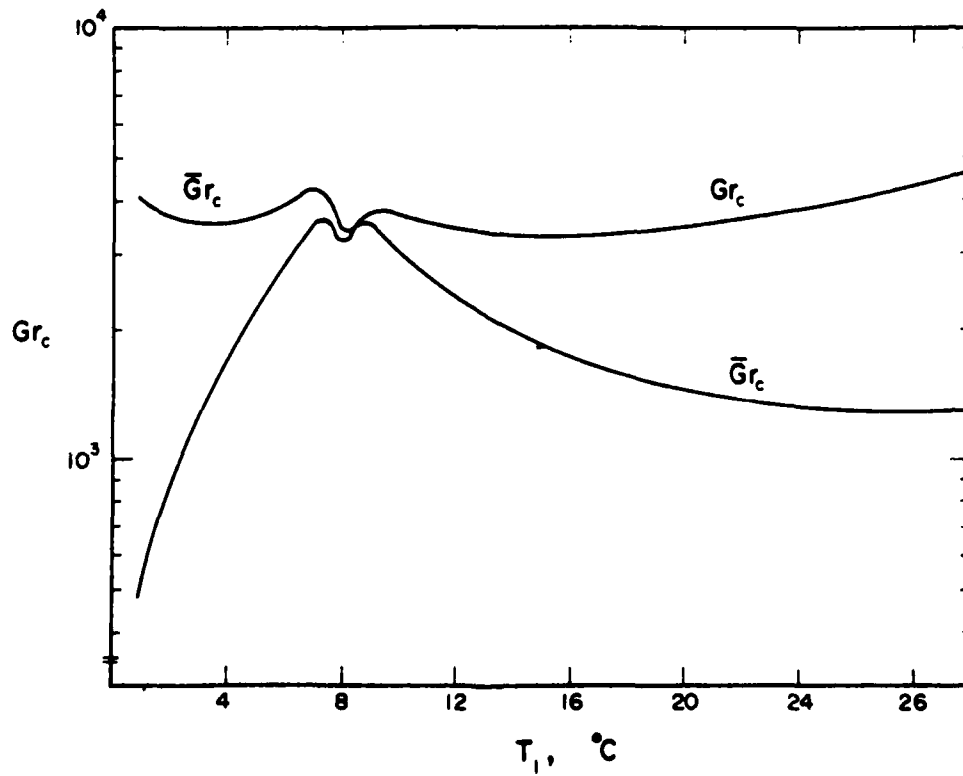


Figure 16. Critical Grashof number Gr_c vs T_1 (Hassab and Sorour 1982).

$$Gr_c = g \gamma_1 T_1^2 h^3 / \nu^2 \quad (19)$$

and

$$\overline{Gr_c} = \frac{\beta_0 g T_1 h^3}{\nu^2} \quad (20)$$

in which β_0 is evaluated from eq 4 as

$$\beta_0 = \left| -\frac{1}{\rho_0} \frac{d\rho}{dT} \right|_{T=T_m} = (2\gamma_1 - 3\gamma_2 T_m) T_m. \quad (21)$$

Substituting values of $\gamma_1 = 0.793953 \times 10^{-5} \text{C}^{-2}$, $\gamma_2 = -0.6559 \times 10^{-7} \text{C}^{-3}$ and $T_m = 4^\circ\text{C}$, the ratio of eq 20 to 19 can be expressed as

$$\overline{Gr_c} = 8.3965 Gr_c / T_1. \quad (22)$$

As shown in Figure 16, the $\overline{Gr_c}$ curves approach an asymptotic value of 1300 for $T_1 > 26^\circ\text{C}$ and, as in horizontally confined melt layers, the critical Grashof number is no longer a constant but varies with T_1 . However, this result would not provide insight into the value of T_1 at which the instability is enhanced or delayed. This uncertainty is due to the dependence of Gr upon both T_1 and the melt layer thickness $h(t)$. It is therefore more appropriate to recast the stability results in terms of critical melt layer thickness h_c and critical melting time t_c , which are derived from the critical Grashof number. The critical melt layer thickness and critical melting time are defined as

$$h_c = \sqrt[3]{\frac{\nu^2 Gr_c}{\gamma_1 g T_1^2}} \quad (23)$$

and

$$t_c = \frac{h_c^2}{4S^2 \alpha}. \quad (24)$$

Figure 17 shows the variation of h_c and t_c as a function of T_1 . The graph can be classified into three regions as follows:

1. In the region when $T_1 < 4^\circ\text{C}$, the density profile has no maximum value; increasing T_1 increases the density difference across the melt layer, accordingly destabilizing the flow. When $T_1 > 4^\circ\text{C}$, the melt layer has a maximum density, but increasing T_1 has a smaller destabilizing rate, although the instability sets in earlier owing to the higher temperature difference across the melt layer.
2. In the region for $7.1^\circ\text{C} \leq T_1 \leq 9.4^\circ\text{C}$, the variations of h_c and t_c are not monotonous for increased T_1 . This trend may be due to the transition in the wave structure from two-column waves for $T_1 < 7.1^\circ\text{C}$ to three column waves for $7.1^\circ\text{C} \leq T_1 \leq 9.4^\circ\text{C}$ and back as two-column waves for $T_1 > 9.4^\circ\text{C}$.
3. In the region for $T_1 > 9.4^\circ\text{C}$, increasing T_1 has a significant destabilizing effect because of the strong bending of the density profile resulting from the pronounced increase of the density difference.

Figures 18a and b show the dimensionless mean base flow velocity across the melt layer thickness. Figure 18a shows the \bar{U} distribution in regions I and III. In region I, a unicellular motion forms so that

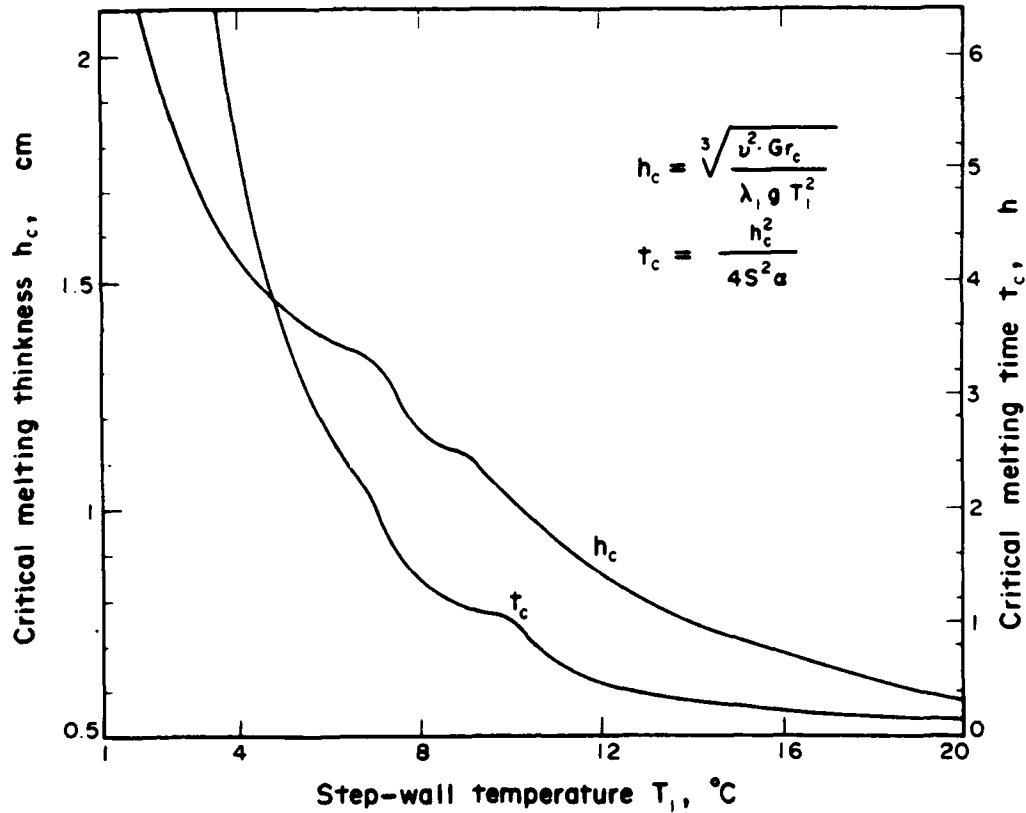
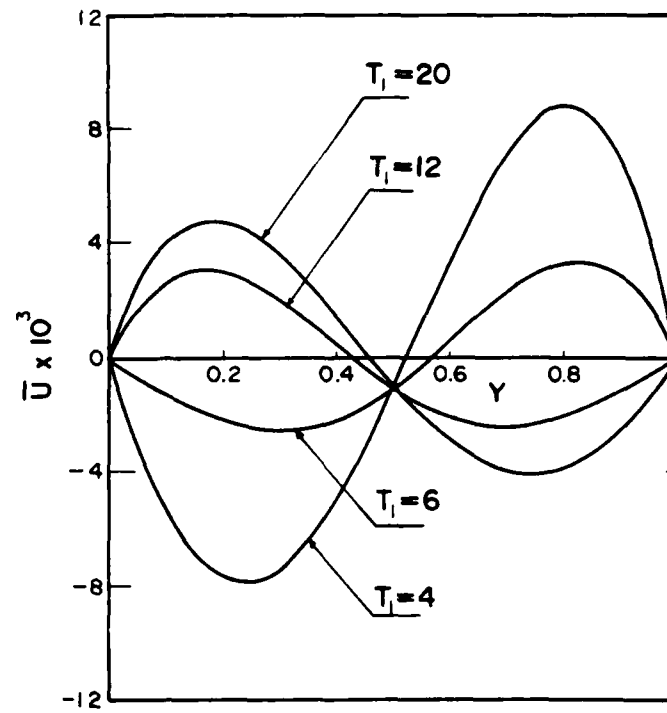


Figure 17. Critical melting thickness, h_c and melting time, t_c as function of step-wall temperature T_1 (Hassab and Sorour 1982).

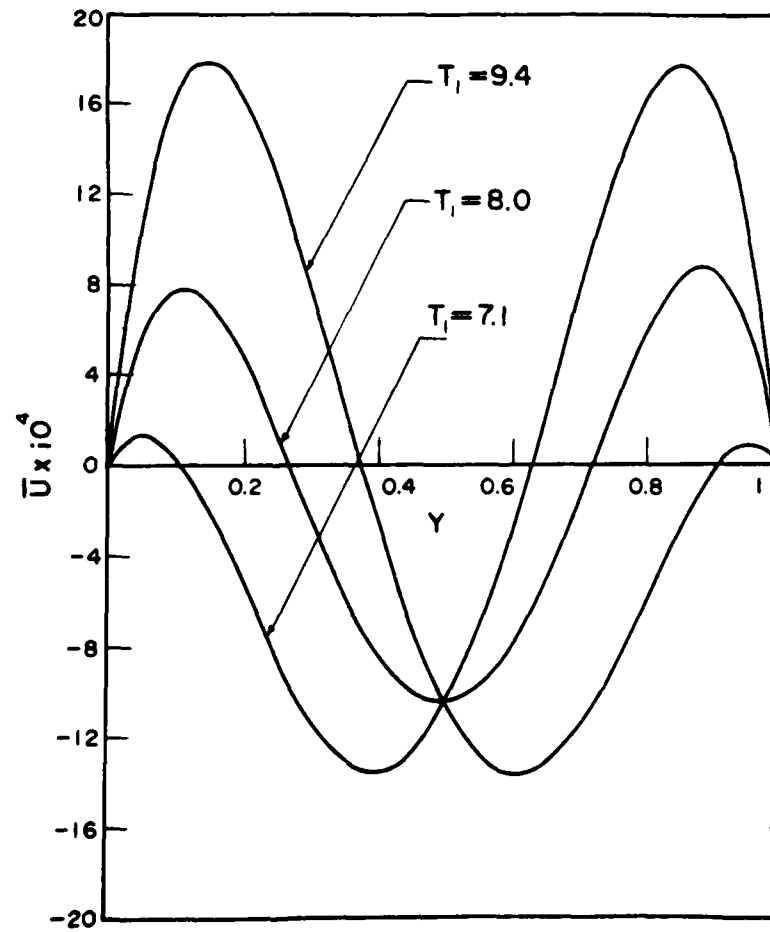
the fluid near the hot wall descends and near the interface ascends. An opposite unicellular motion occurs in region III because the water near the interface is denser than that near the hot wall. However, in region III (Fig. 18b), the fluid at the central part is denser than that next to the boundaries. Therefore, two parallel cells form, with the fluid at the central part moving downwards and that adjacent to the boundaries moving upwards. Figure 19 shows the variation of average volumetric expansion $\bar{\beta}$ as a function of T_1 and sheds some light on the magnitude of \bar{U} in regions I and III. When $T_1 < 8.2^\circ\text{C}$, $\bar{\beta}$ decreases with increases of T_1 ; for $T_1 > 8.2^\circ\text{C}$, $\bar{\beta}$ increases with increasing T_1 . Since the shear flow is driven by the buoyancy effects that are linearly dependent upon $\bar{\beta}$, increasing T_1 will suppress the dimensionless base flow \bar{U} in region I while expanding it in region III. (See Fig. 18a to compare \bar{U} curves for $T_1 = 4^\circ$ and 6°C , and for $T_1 = 12^\circ$ and 20°C .)

The stability problem of natural convection in a vertical melt layer can be classified in terms of the boundary temperature T_1 into three regions:

1. For $T_1 < 7.1^\circ\text{C}$, stability sets in as two-column waves travel opposite in the vertical direction. Although heating increases Gr it is actually destabilizing the flow with a decreasing rate.
2. For temperature range $7.1^\circ < T_1 < 9.4^\circ\text{C}$, instability occurs as three-column waves. Minimum wavelength and minimum wave speed occur at 8°C and maximum values of Gr_c occur at $T_1 = 7.3^\circ$ and 9.2°C , respectively. In this region heating also destabilizes the flow.
3. For $T_1 > 9.4^\circ\text{C}$, the instability recurs as two column waves, with both wave speed and wavelength increasing (see Fig. 20 and 21) as T_1 increases. Again, heating has a destabilizing effect on the flow.



a. Regions I and III.



b. Region III.

Figure 18. Velocity profiles in Regions I and III (Hassab and Sorour 1982).

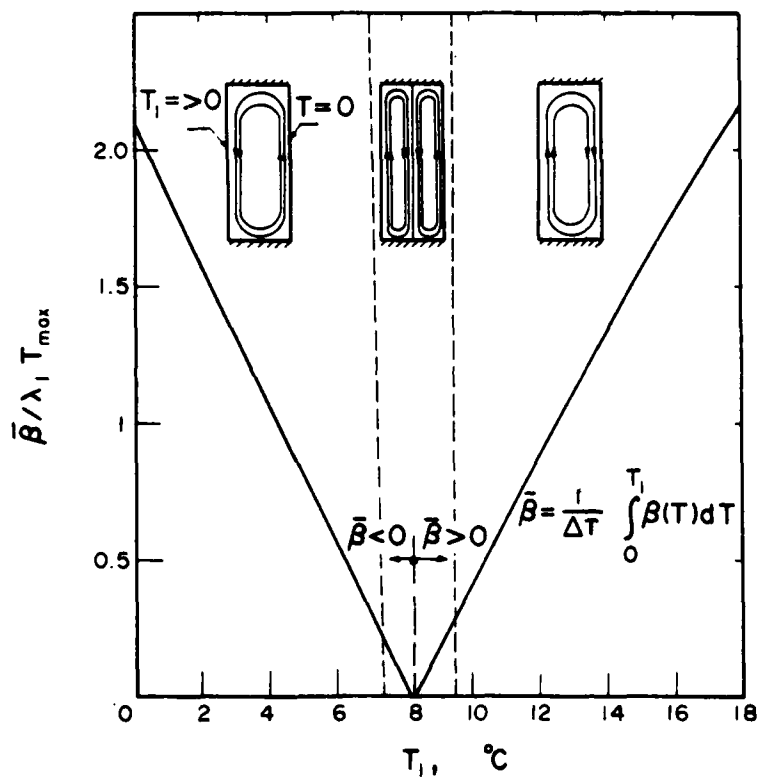


Figure 19. Average coefficient of thermal expansion $\bar{\beta}$ vs T_1 (Hassab and Sorour 1982).

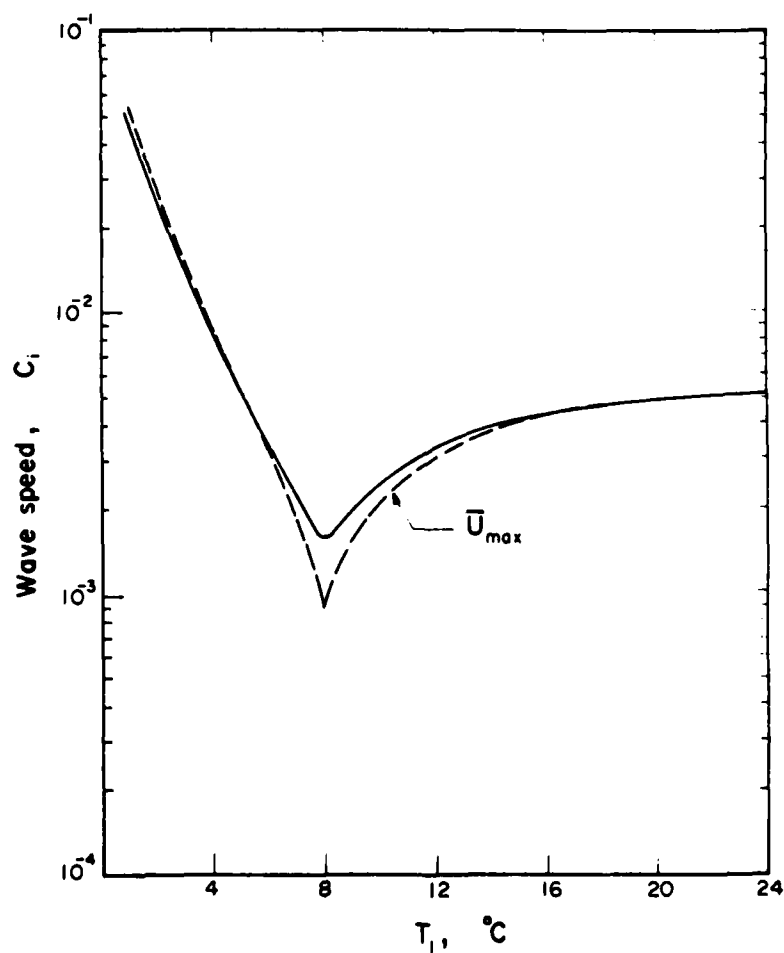


Figure 20. Variation of wave speed, C_i vs T_1 (Hassab and Sorour 1982).

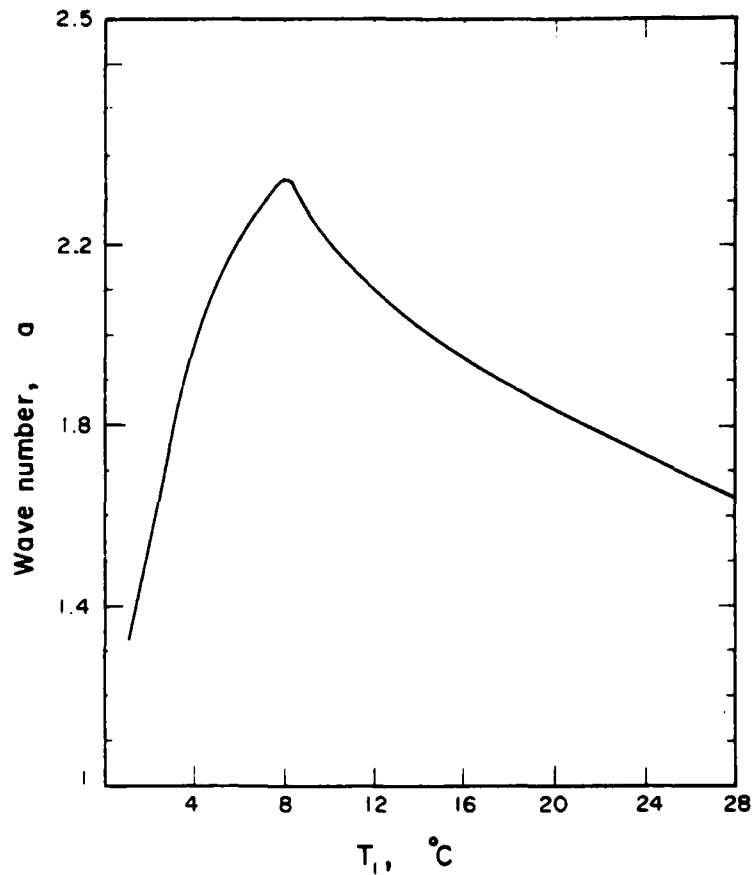


Figure 21. Variation of wave number, α vs T_1 (Hassab and Sorour 1982).

EFFECT OF 4°C ON HEAT TRANSFER IN PURE WATER AND ICE-WATER SYSTEMS

In a vertical enclosure

The vast majority of the natural convection studies reported so far pertain to fluids whose density decreases or increases monotonically with the temperature at a constant pressure. However, for liquids such as water, the density-temperature curve exhibits a maximum value. Since the coefficient of thermal expansion changes sign through the maximum, the use of linear approximation of density to model water is inappropriate in the range of temperature that corresponds to the density maximum. Lankford and Bejan (1986) were the first to investigate the natural convection in a vertical enclosure filled with water near 4°C. Two series of experimental runs were reported: one set for T_H (hot-wall) and T_C (cold-wall) temperatures well above T_m (temperature corresponding to maximum density), and one set for T_H and T_C embracing T_m .

Figures 22 and 23 show typical wall temperature distributions as a function of dimensionless height y/H and their corresponding flow patterns. When the temperature everywhere in the enclosure is well above 4°C the wall temperature increases almost linearly with height and, at each level, the wall-to-wall temperature difference is practically constant (Fig. 22). In experiments where the entire enclosure is below 4°C, the water density consistently increases upon heating. The wall temperature distribution in such a case is similar to that shown in Figure 22 except that the temperature of both walls decreases with height.

When the enclosure temperature range includes 4°C and when the average enclosure temperature is slightly less than 4°C, the sinking core jet emerges from near the top of the warm wall, and along the cold wall the water jet rises all the way to the top as it is cooled to a temperature close to 0°C. The same jet turns around at the top of the enclosure and descends along the warm wall, because its density increases as its temperature increases from 0° to 4°C.

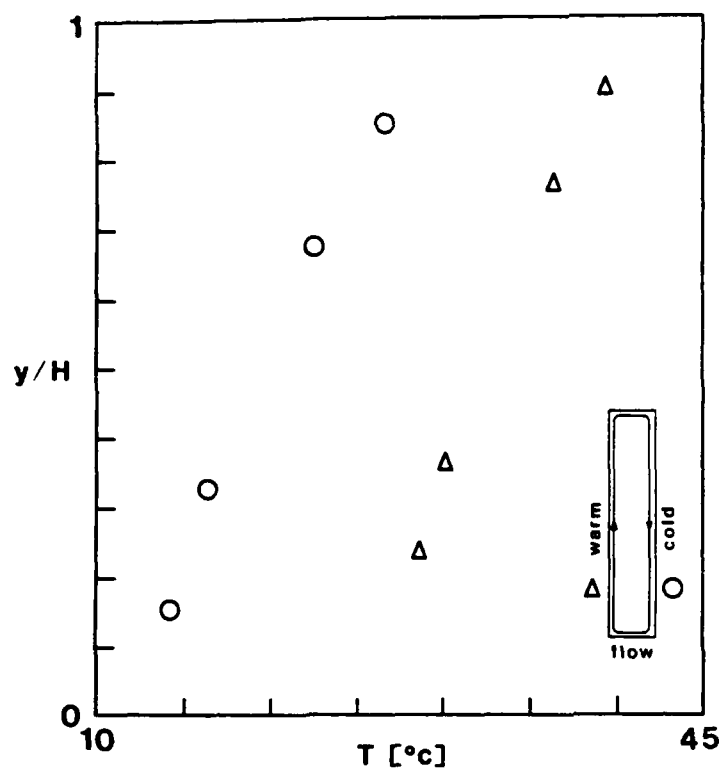


Figure 22. Example of wall temperature distribution with T_H and T_C consistently greater than T_m (Lankford and Bejan 1986).

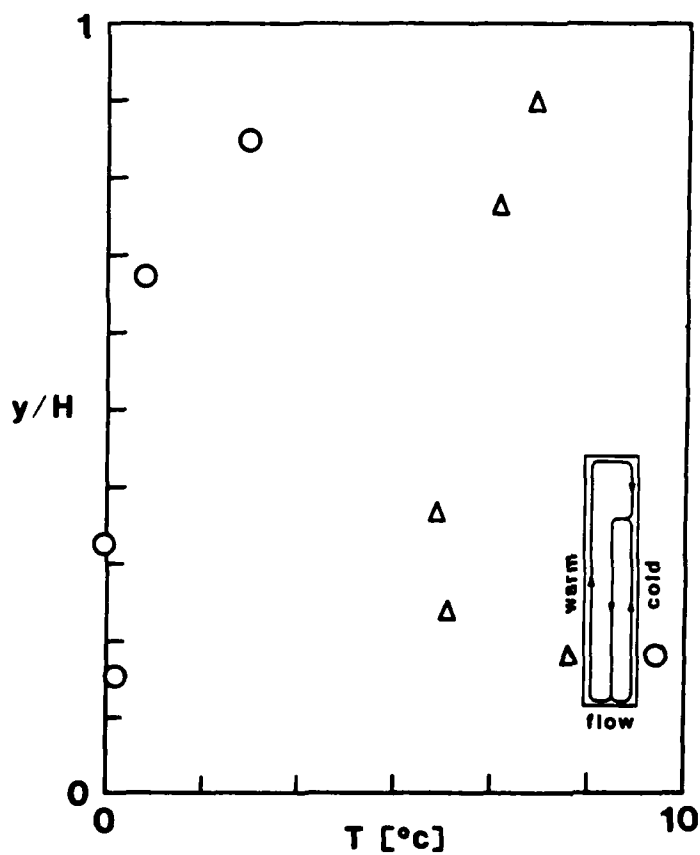


Figure 23. Example of wall temperature distribution when T_H and T_C embrace T_m (Lankford and Bejan 1986).

When the average enclosure temperature is slightly above 4°C the sinking core jet emerges from a point near the top of the cold wall. Along the warm wall, which is swept by a jet whose density decreases monotonically with temperature, the temperature distribution has the same features as those in an enclosure heated with uniform heat flux from the side and filled with fluid whose density conforms to the linear density-temperature. Along the cold wall, however, the collision of the two counterflowing jets is felt as a sharp change in vertical temperature gradient near the level of collision (see Fig. 23).

Figure 24 shows the experimental results for the case of an average water temperature well above 4°C along with empirical correlations recommended for the cases of isothermal walls and constant-heat-flux-walls. In this case, the heat transfer data can be well represented by

$$Nu = 0.203 Ra_H^{0.28} \quad (25)$$

in which

$$Nu = \frac{Q}{Wk(\bar{T}_h - \bar{T}_c)} \quad (26)$$

and

$$Ra_H = \frac{g\beta H^3 (\bar{T}_H - \bar{T}_C)}{\nu\alpha} \quad (27)$$

where Q = the overall heat transfer rate,
 W = the enclosure width,
 \bar{T}_H = the height,
 \bar{T}_C = height-averaged wall temperatures.

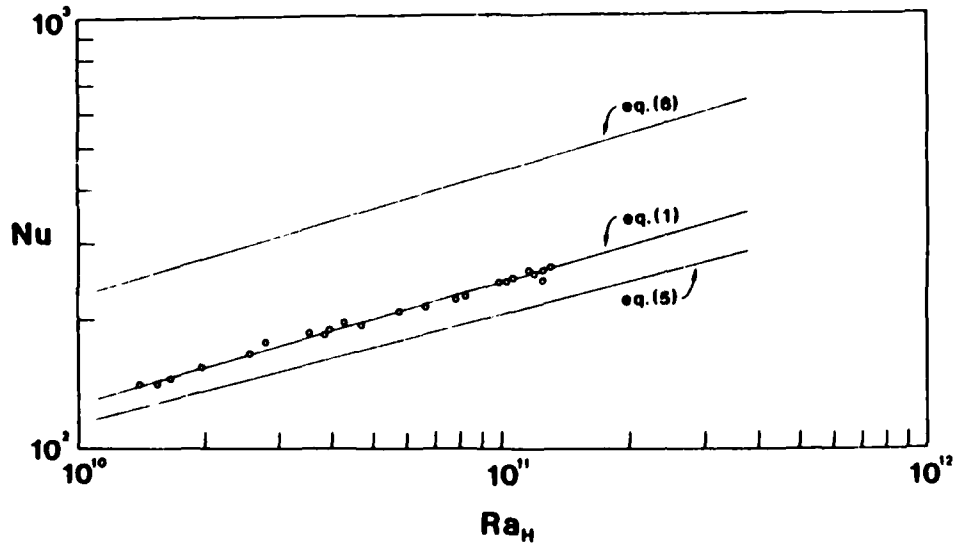


Figure 24. Correlation of heat transfer results in water at temperatures above 4°C (Lankford and Bejan 1986).

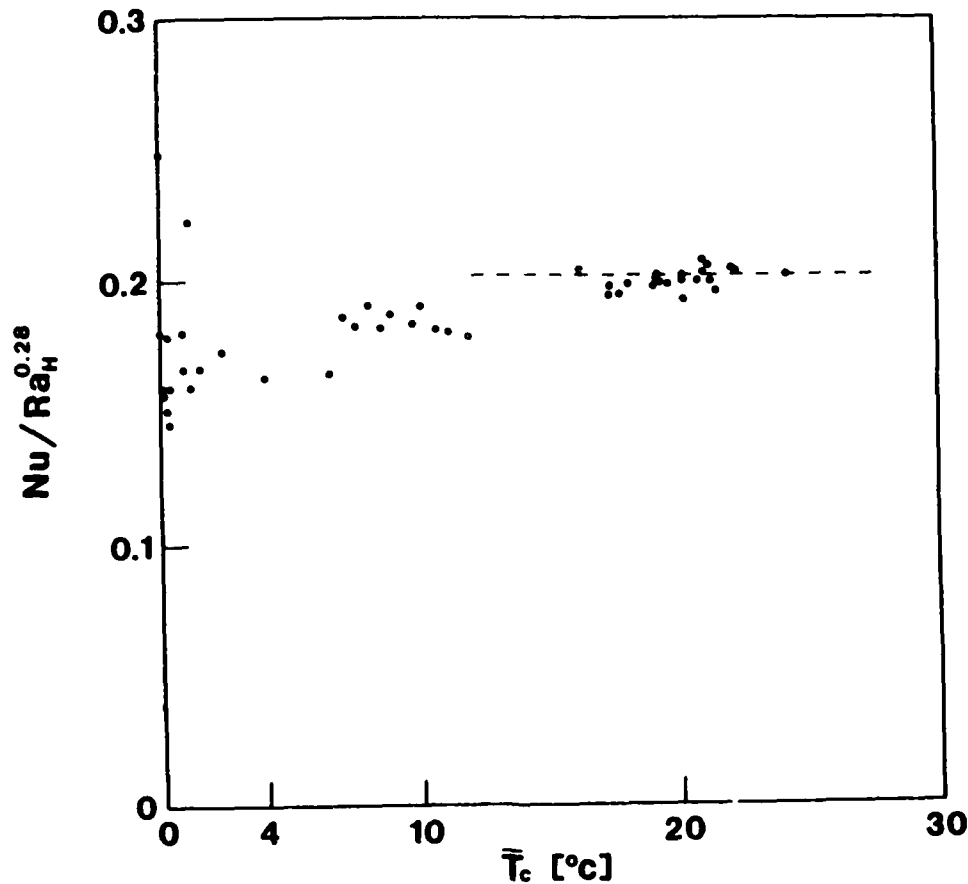


Figure 25. The breakdown of the Nu and Ra_H correlation (eq 25) as T_m is approached (Lankford and Bejan 1986).

The physical properties k , α , β , and ν were evaluated at the average enclosure temperature defined as

$$T_{avg} = \frac{1}{2} (\bar{T}_H + \bar{T}_C) \quad (28)$$

The experimental results are found to agree well with the isothermal wall correlation reported by Bejan (1979), i.e.,

$$Nu = 0.364 Ra_H^{1/4} \quad (29)$$

However, the slope of the empirical correlation of eq 25 is nearly identical to that of eq 30 reported by Kimura and Bejan (1984) for the case of constant-heat-flux wall, i.e.,

$$Nu = 0.25 \left(\frac{H}{L} \right)^{1/7} Ra_H^{2/7} \quad (30)$$

Figure 25, a plot of $Nu/Ra_H^{0.28}$ vs \bar{T}_C , shows clearly how these correlation methods deteriorate as temperatures approach 4°C. The maximum density flow pattern inhibits the transfer of heat, causing a decrease in Nusselt number that was not accounted for in the development of eq 25. Even in the range of temperatures immediately above 4°C, where the density maximum has not neces-

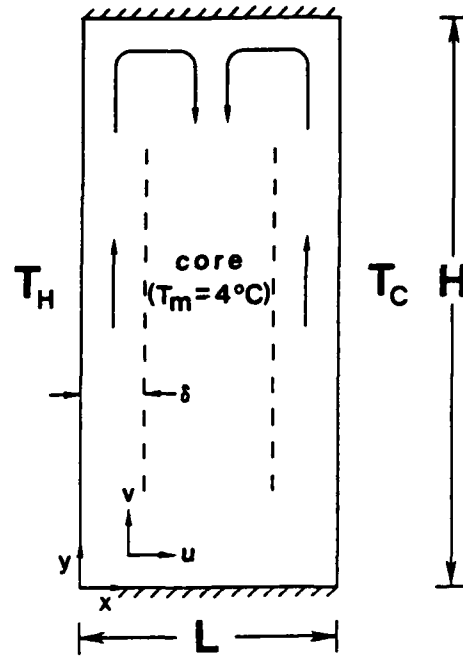


Figure 26. Schematic of the boundary layer regime in a vertical space filled with cold water at a mean temperature of 4°C (Lankford and Bejan 1986).

sarily been crossed, the data still tend to deviate from the constant value assumed by eq 25 (see the dotted line in Fig. 25). This is because the coefficient of thermal expansion β used in the linear density-temperature approximation (i.e., $\rho = \rho_0 [1 - \beta(T - T_0)]$ where ρ_0 and T_0 are the reference density and temperature, respectively), changes so rapidly near 4°C that averaging it in the normal fashion leads to significant errors.

To overcome this difficulty, Lankford and Bejan (1986) adopted the technique of scale analysis by considering the boundary layer regime for natural convection in near 4°C water. Figure 26 shows the case where the side-wall temperatures occur symmetrically above and below 4°C. It shows that the maximum density sinking jet originates from near the top of the enclosure. The convection pattern consists of two boundary jets rising along the differentially heated side walls, and a maximum density sinking core with $T_m \approx 4^\circ\text{C}$. Thermal boundary thickness δ_H and δ_C can be scaled from the classical case for fluid with $Pr > 1$ (Bejan 1984), i.e.,

$$\delta_H \approx H \left(\frac{gH^3 \Delta\rho/\rho}{\nu\alpha} \right)^{-1/4} \quad (31)$$

Expressing $\Delta\rho/\rho = \gamma(T - T_m)^2$ (from eq 2), eq. 31 becomes

$$\delta_H \approx H \left(\frac{g\gamma H^3 (T - T_m)^2}{\nu\alpha} \right)^{-1/4} \quad (32)$$

Similarly for the cold-side boundary layer we have

$$\delta_C \approx H \left(\frac{g\gamma H^3 (T_m - T_c)^2}{\nu\alpha} \right)^{-1/4} \quad (33)$$

The quantity in the square brackets in eq 32 and 33 is the Rayleigh number for fluids with parabolic density variation near the density maximum.

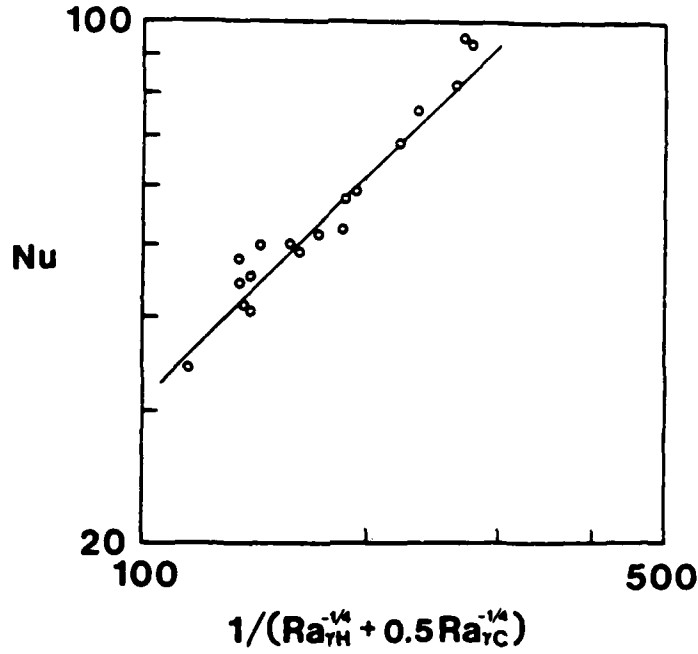


Figure 27. Correlation of heat transfer results in water at temperature near 4°C (Lankford and Bejan 1986).

The scale of overall heat transfer rate from T_H to T_c can be written as

$$Q \sim \frac{T_H - T_c}{R_H + R_c} \quad (34)$$

where $R_H \approx \delta_H/kHW$ and $R_c \approx \delta_c/kHW$. From eq 32 and 33, eq 34 can be expressed as

$$Nu = \frac{C_1}{Ra_{\gamma H}^{-1/4} + C_2 Ra_{\gamma c}^{-1/4}} \quad (35)$$

where

$$Ra_{\gamma H} = \frac{g\gamma H^3 (T_H - T_m)^2}{\nu\alpha}, \quad Ra_{\gamma c} = \frac{g\gamma H^3 (T_m - T_c)^2}{\nu\alpha} \quad (36)$$

Figure 27 shows an excellent correlation of the heat transfer results of water at near 4°C with eq 35 derived from scale analysis. The solid line drawn through the experimental points is a plot of eq 35 with assumed values of $C_1 = 0.31$ and $C_2 = 0.5$. These constants were chosen such that the standard deviation between eq 35 and the measurements was minimized when summed over all the experimental points.

In a vertical annulus

Lin and Nansteel (1987b) were the first to investigate systematically the effect of curvature and aspect ratio on the flow structure and heat transfer in a vertical annulus. Figure 28 shows the vertical annulus, coordinate system and thermal boundary conditions. Lin and Nansteel (1987b) assumed that the flow in the gap is laminar and axisymmetric, and all fluid properties are constant except for density in the buoyancy term of the vertical momentum balance. They introduced dimensionless variables

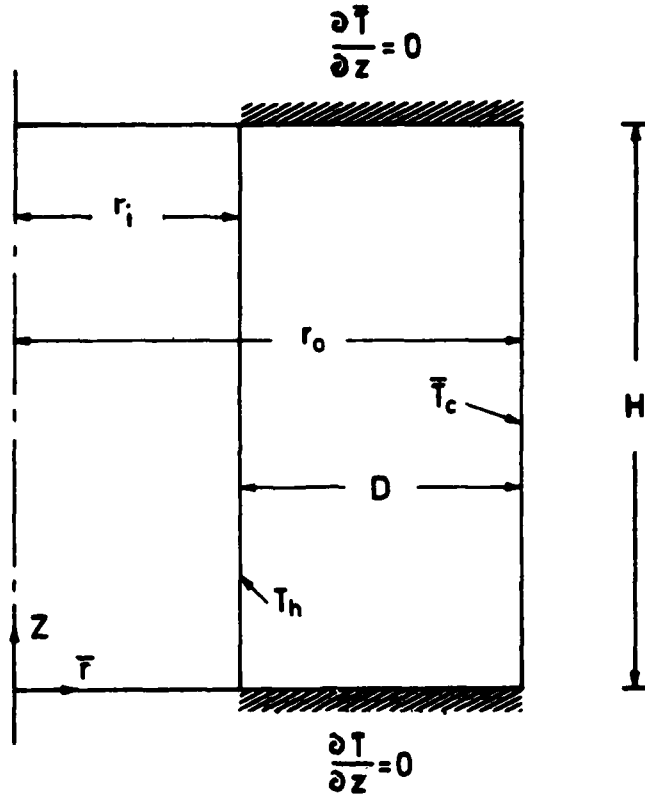


Figure 28. Vertical annulus, coordinate system and thermal boundary conditions (Lin and Nansteel 1987b).

$$R = \frac{r - r_i}{D}, \quad Z = \frac{z}{D}, \quad U = \frac{u D}{v_c}, \quad V = \frac{v D}{v_c}$$

$$\tau = \frac{v_c t}{D^2}, \quad P = \frac{p D^2}{\rho_c v_c^2}, \quad \theta = \frac{T - T_c}{T_h - T_c}$$

and represented the density-temperature relation as

$$\rho = \rho_m [1 - \alpha_1 |T - T_m|^q]. \quad (37)$$

The governing equations for conservation of mass, momentum and energy in the annulus are given as

$$\frac{\partial U}{\partial R} + \frac{\partial V}{\partial Z} + \frac{(K-1)}{(K-1)R+1} U = 0 \quad (38)$$

$$\frac{DU}{Dt} = -\frac{\partial P}{\partial R} + \frac{\partial^2 U}{\partial R^2} + \frac{(K-1)}{(K-1)R+1} \frac{\partial U}{\partial R} + \frac{\partial^2 U}{\partial Z^2} - \left[\frac{(K-1)}{(K-1)R+1} \right]^2 U \quad (39)$$

$$\frac{DV}{Dt} = -\frac{\partial P}{\partial Z} + \frac{Ra'}{Pr} [|\theta - R'q - 1 - R'q|] + \frac{\partial^2 V}{\partial R^2} + \frac{(K-1)}{(K-1)R+1} \frac{\partial V}{\partial R} + \frac{\partial^2 V}{\partial Z^2} \quad (40)$$

$$\frac{D\theta}{Dt} = \frac{1}{Pr} \left[\frac{\partial^2 \theta}{\partial R^2} + \frac{(K-1)}{(K-1)R+1} \frac{\partial \theta}{\partial R} + \frac{\partial^2 \theta}{\partial Z^2} \right], \quad (41)$$

where $U = V = 0$ on the boundary

$$\theta(0, Z) = 1, \theta(1, Z) = 0$$

$$\frac{\partial \theta}{\partial Z}(R, 0) = \frac{\partial \theta}{\partial Z}(R, A) = 0.$$

K = the ratio of r_o/r_i , which characterizes the degree of curvature,

Pr = the Prandtl number, ν_c/α_c

A = the aspect ratio H/D .

The Rayleigh number is defined as

$$Ra' = \frac{G\rho_m \alpha_1 (T_h - T_c)^q D^3}{\rho_c \nu_c \alpha_c} \quad (42)$$

and the density distribution parameter as

$$R' = \frac{T_m - T_c}{T_h - T_c} \quad (43)$$

which fixes the orientation of the maximum density temperature with respect to the wall temperatures T_h and T_c . For example, $R' = 1/2$ corresponds to the circumstance in which the hot and cold wall temperatures perfectly straddle the maximum density temperature for $0 < R' < 1$, (i.e., $T_h > T_m$), and the water density in the annulus increases with increasing temperature to a maximum $\rho = \rho_m$ at $T = T_m$ and then decreases with any further increase in temperature. On the other hand $R' = 0$ corresponds to the case in which the cold wall is at temperature T_m so that fluid density decreases monotonically with temperature everywhere in the annulus. For $R' = 0$, flow in the annulus is similar to the flow of a Boussinesq fluid, but only in a qualitative sense since density is a nonlinear function of temperature. When $R' = 1$, $T_h = T_m$ the density increases monotonically with temperature everywhere in the annulus.

Eliminating P in eq 30 and 40 and introducing the dimensionless vorticity ξ

$$\xi = \frac{\partial V}{\partial R} - \frac{\partial U}{\partial Z}$$

and stream function $\bar{\psi}$

$$U = \frac{(K-1)}{(K-1)R+1} \frac{\partial \bar{\psi}}{\partial Z}, \quad V = - \frac{(K-1)}{(K-1)R+1} \frac{\partial \bar{\psi}}{\partial R}$$

we have

$$\begin{aligned} \frac{D\xi}{Dt} - \frac{(K-1)}{(K-1)R+1} U\xi = \frac{Ra'}{Pr} q |\theta - R'|^{q-2} (\theta - R') \frac{\partial \theta}{\partial R} + \frac{\partial^2 \xi}{\partial R^2} \\ + \frac{\partial^2 \xi}{\partial Z^2} + \frac{(K-1)}{(K-1)R+1} \frac{\partial \xi}{\partial R} - \left[\frac{(K-1)}{(K-1)R+1} \right]^2 \xi \end{aligned} \quad (44)$$

with

$$\xi = - \frac{1}{(K-1)R+1} \left(\frac{\partial^2 \bar{\psi}}{\partial R^2} + \frac{\partial^2 \bar{\psi}}{\partial Z^2} - \frac{(K-1)}{(K-1)R+1} \frac{\partial \bar{\psi}}{\partial R} \right). \quad (45)$$

The Nusselt numbers at the inner and outer walls can be expressed as

$$Nu_i = \frac{q''_i D}{k(T_h - T_c)} = - \frac{1}{A} \int_0^A \frac{\partial \theta}{\partial R}(0, Z) dZ \quad (46)$$

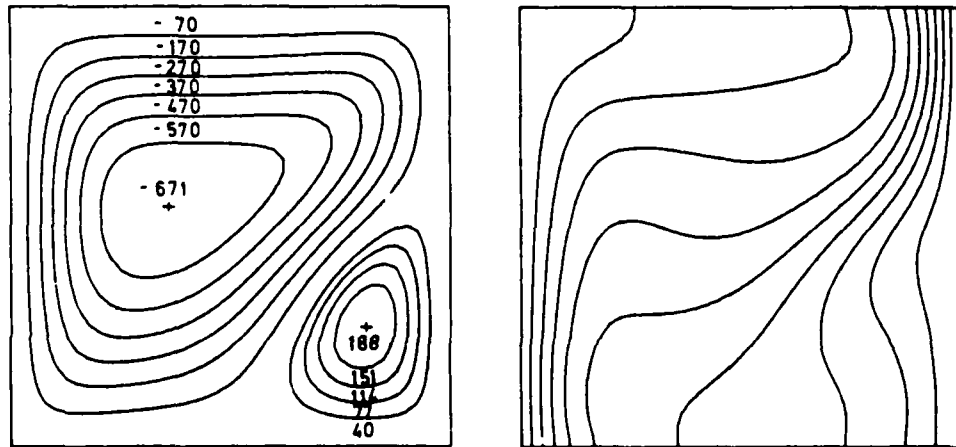
and

$$Nu_o = \frac{q''_o D}{k(T_h - T_c)} = - \frac{1}{A} \int_0^A \frac{\partial \theta}{\partial R}(1, Z) dZ. \quad (47)$$

Nu_i is related to Nu_o by

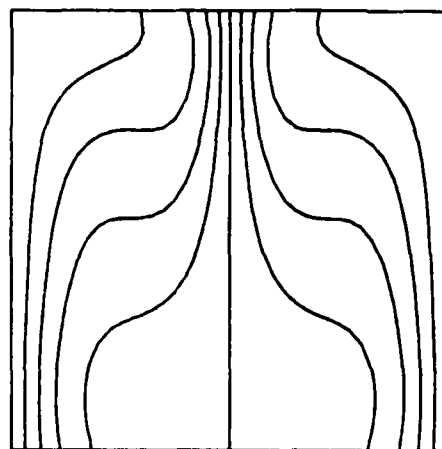
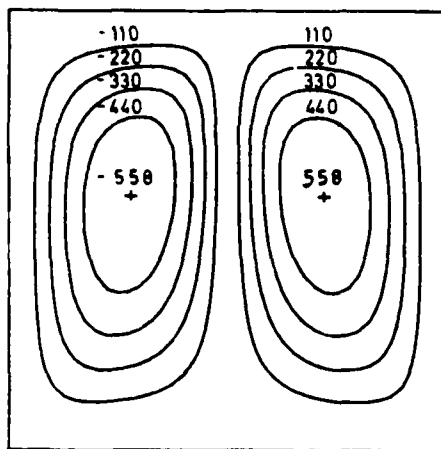
$$Nu_i = K Nu_o. \quad (48)$$

Numerical results were obtained by solving eq 41 and 45 with the finite difference method. Figure 29 shows the effect of R' on flow structure and temperature distribution for the case of $A=1$ (aspect ratio) and $K=1$ (no curvature effect) and $Ra'=10^5$. In Figure 29a, $R'=0.4$, the two counterrotating cells are separated roughly by the maximum density isotherm $\theta = R' = 0.4$. In Figure 29b, the relatively light fluid rises adjacent to the heated and cooled walls, while dense fluid $\rho = \rho_m$, $T \approx T_m$ falls near the enclosure vertical midplane in a symmetric dual-cell pattern. As R' increases, the counterclockwise rotating cell has grown substantially in size and strength at the expense of the clockwise rotating cell. In the case of $R' = 1$, the density increases with temperature everywhere, resulting in a single counterclockwise vortex. This flow pattern is qualitatively similar to the convection of a Boussinesq fluid except for the direction of circulation.

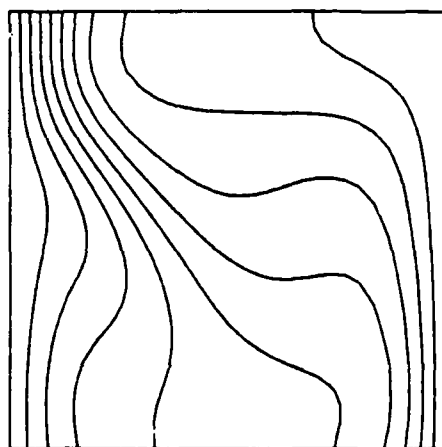
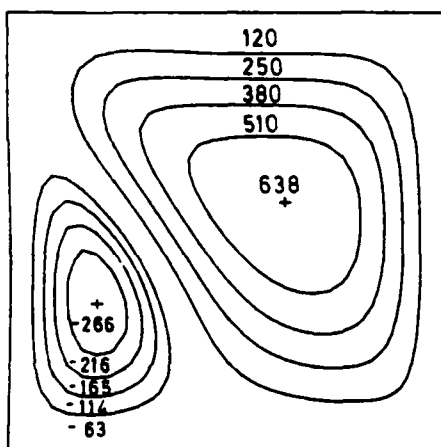


a. $R' = 0.4$.

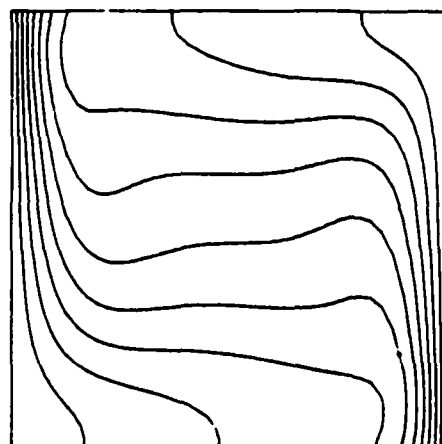
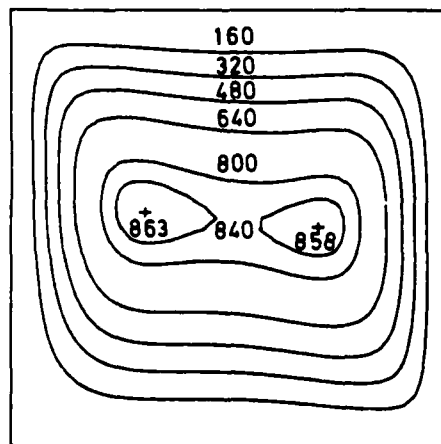
Figure 29. Stream function ($\bar{\psi} \times 10^3$) and temperature ($\theta = 0(0.1)1$) contours for $A = 1$, $K = 1$, and $Ra' = 10^5$ (Lin and Nansteel 1987b).



b. $R' = 0.5$.

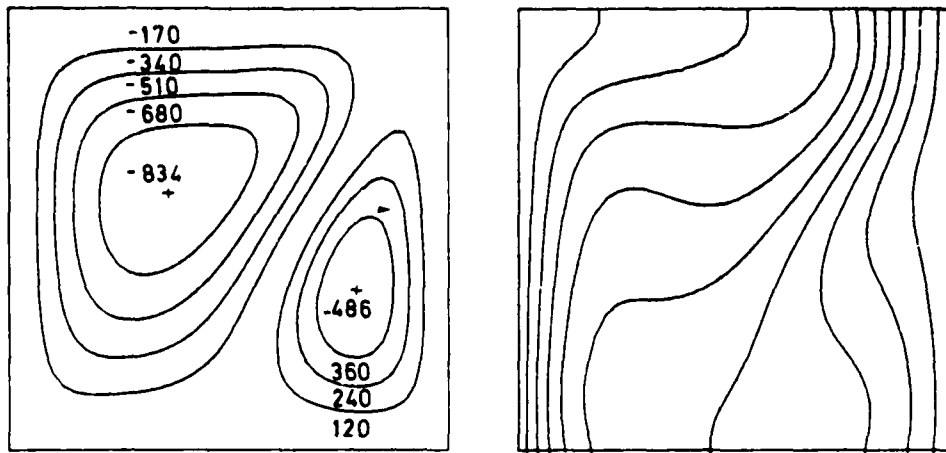


c. $R' = 0.55$.

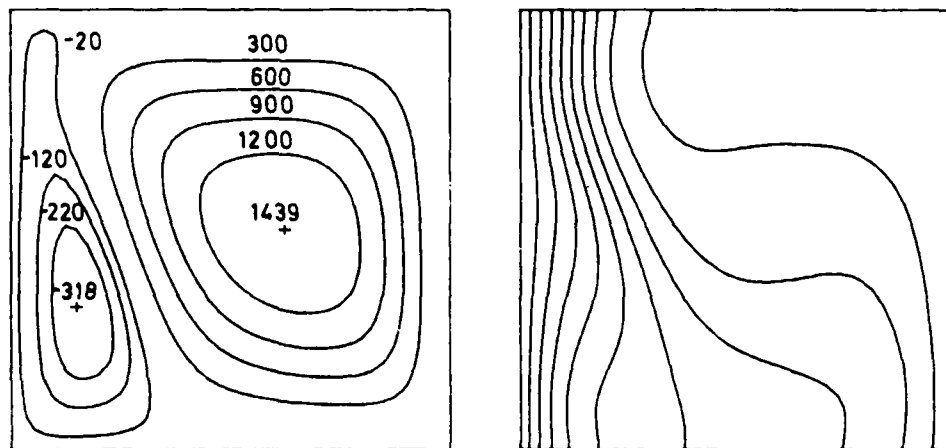


d. $R' = 1.0$.

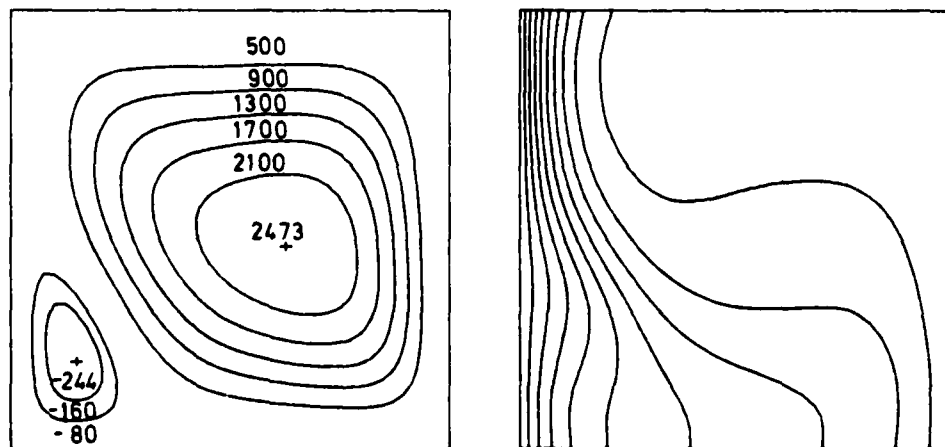
Figure 29 (cont'd). Streamfunction ($\bar{\psi} \times 10^3$) and temperature ($\theta = 0(0.1)1$) contours for $A = 1$, $K = 1$, and $Ra' = 10^5$ (Lin and Nansteel 1987b).



a. $K = 2$



b. $K = 4$.



c. $K = 8.0$.

Figure 30. Effect of K on distribution of stream function ($\bar{\psi} \times 10^3$) and temperature ($\theta = 0(0.1)1$) for $A = 1$, $R' = 0.4$ and $Ra' = 10^5$ (Lin and Nansteel 1987b).

Figure 30 shows the effect of K on flow structure and temperature contours for $A = 1$, $Ra' = 10^5$, and $R' = 0.4$. As indicated in eq 46, the average heat flux at the inner walls is K times larger than the average heat flux at the outer wall under steady conditions. As a result, with increasing K , isotherms will become increasingly crowded near the inner cylinder. As the maximum density water shifts toward the inner cylinder, so does the line of demarcation between the outer counterclockwise-rotating cell and the inner clockwise-rotating cell. Thus for fixed R' , the outer cell strengthens and the inner cell weakens with increasing curvature of the annulus (i.e., as K increases).

Figure 31 shows the effect of A on $\bar{\psi}$ and θ for the case of $K = 2$, $R' = 1/2$ and $Ra' = 10^4$. Clearly, increasing A tends to increase the convective intensity of the outer cell. This is because the quenching effect of the unheated horizontal surfaces lessens as A is increased and the temperature field becomes dominated by conduction over much of the vertical span of the annulus when $A \geq 4$. Only near the top of the annulus, where the counterclockwise outer cell sweeps cool fluid from the outer wall onto the heated inner wall, does the contribution of convection become significant. This phenomenon is not

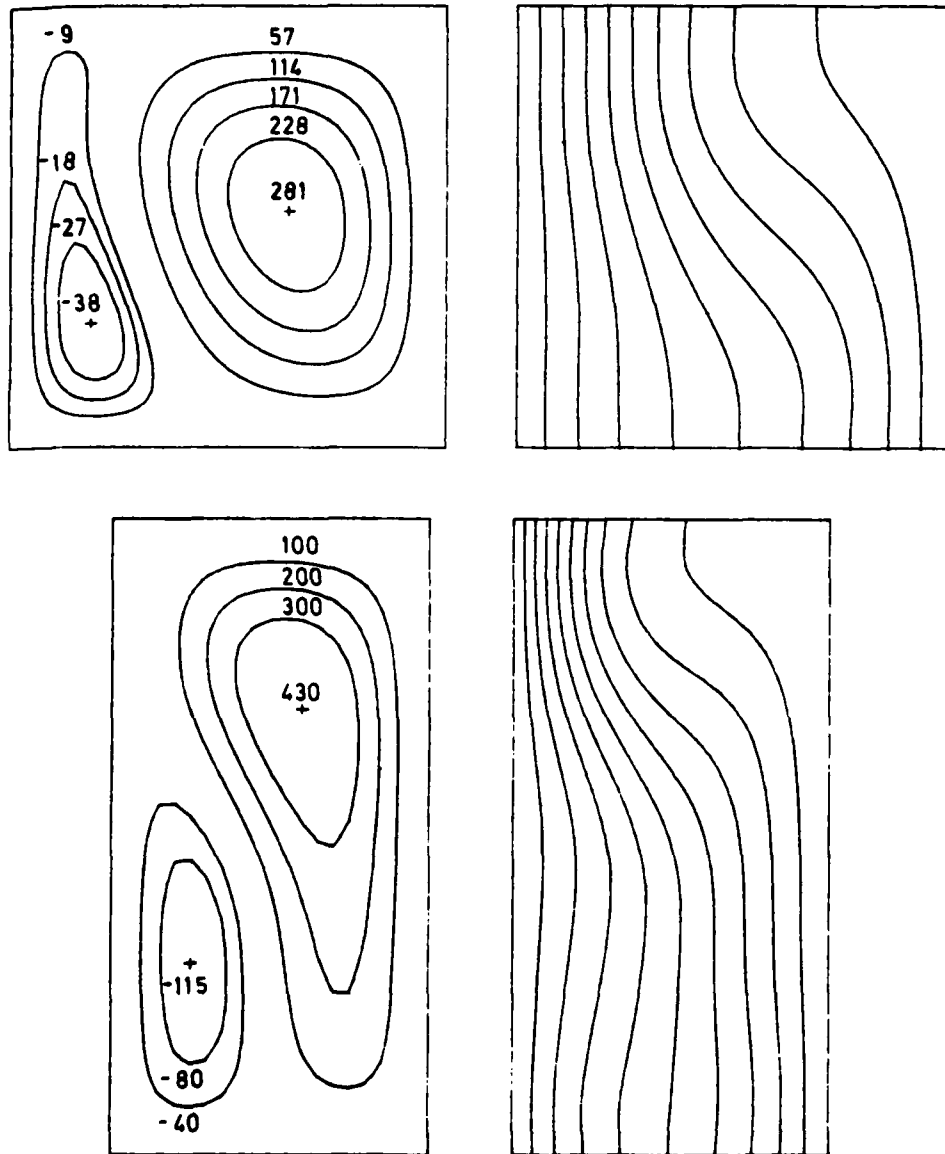


Figure 31. Effect of A on distribution of stream function ($\bar{\psi} \times 10^3$) temperature contour ($\theta = 0(0.1)1$) for $R' = 0.5$, $K = 2$ and $Ra' = 10^4$ (Lin and Nansteel 1987b).

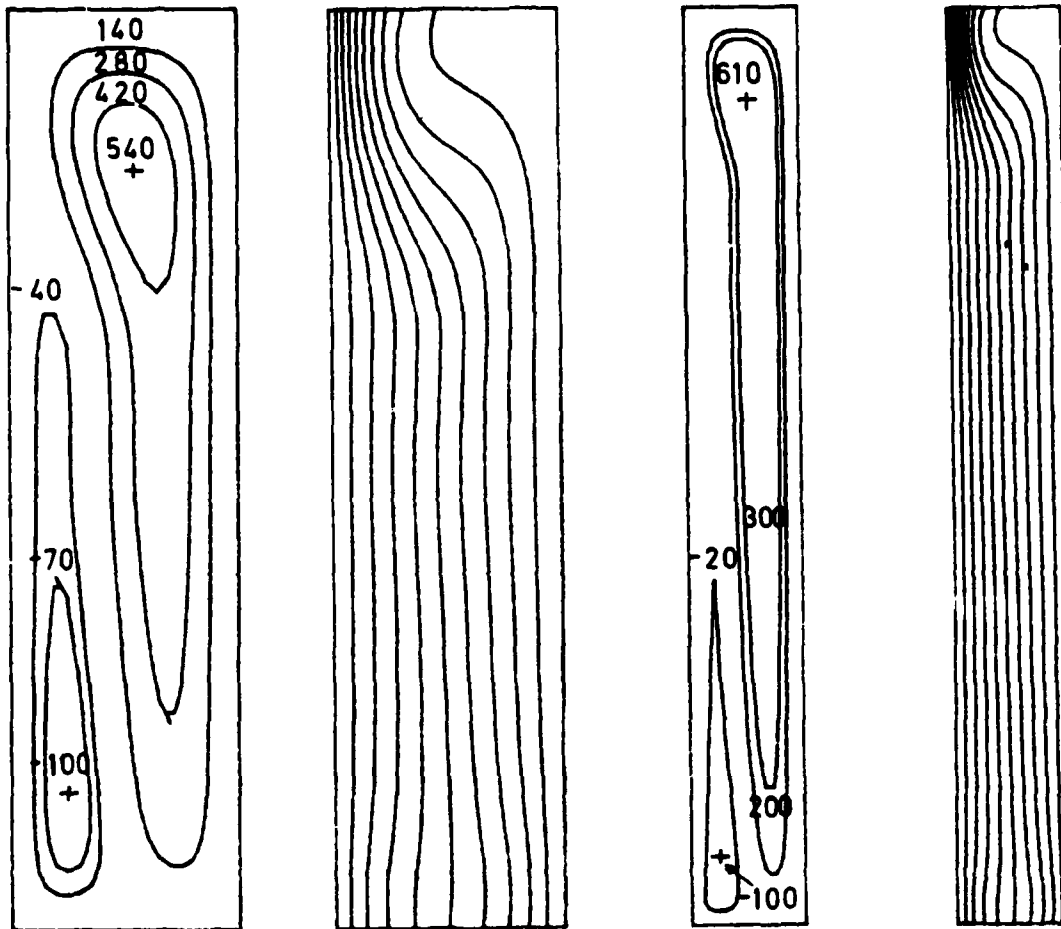


Figure 31 (cont'd).

observed near the bottom of the annulus space because of the existence of a dual-cell structure, which prevents the contact between the inner cell and outer, cooled wall.

Heat transfer

Figure 32 shows the variation of Nu_i with K ($K = r_o/r_i$) for the case $R' = 0.4$, $A = 1$ and a range of $10^3 \leq Ra' \leq 10^5$. In this particular condition, there is a transition from inner to outer cell dominance as curvature (i.e., as K) increases. This occurs in the range of $2 \leq K \leq 5$ for $10^3 \leq Ra' \leq 10^5$. The smooth transition takes place from a case where the inner cell wets both walls to one in which the outer cell wets both walls. Over much of this range of K , the cells are of roughly equal strength and the inner cell is effectively insulated from the outer wall by the outer cell and vice versa. This in turn leads to a diminished rate of convective heat transfer from the inner to the outer wall. The result is a minimum heat transfer rate near $K = 3.5$, but only a minimum rate of increase of Nu_i with K , since conduction heat transfer increases quite rapidly with increasing K . The curve for $Ra' = 10^3$ shows no point of inflection because the contribution of convection to Nu_i is rather small. The variation of $(Nu_i)_{\text{cond}}$ can be related to K by

$$(Nu_i)_{\text{cond}} = \frac{K - 1}{\ln K}. \quad (49)$$

The value of $(Nu_i)_{\text{cond}}$ is, in general, not in unity as it is in the case of $K = 1$ (rectangular enclosure). The effect of K and Ra' on Nu_i is easily observed by plotting $Nu_i/(Nu_i)_{\text{cond}}$ vs K as it is shown in Figure

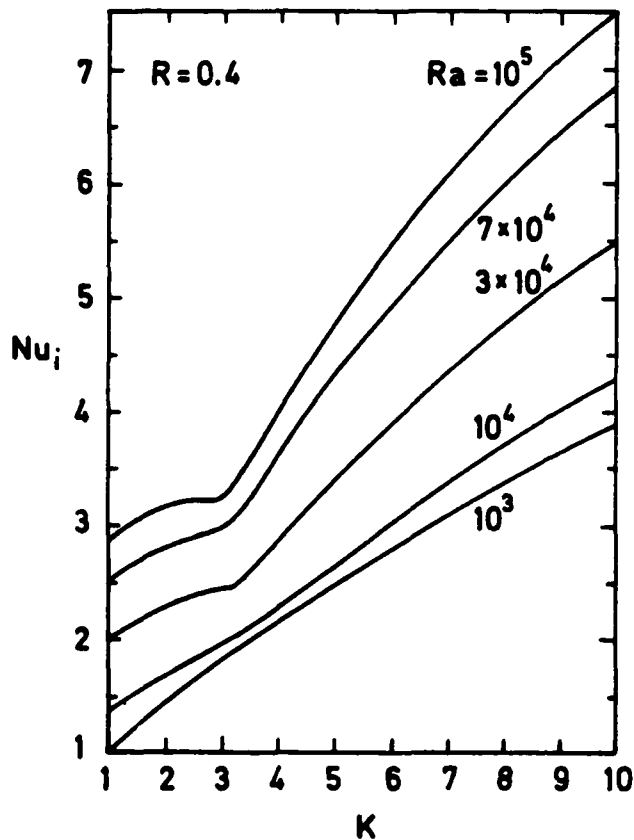


Figure 32. Variation of Nu_i with K for $R' = 0.4$, $A = 1$ using Ra' as a parameter (Lin and Nansteel 1987b).

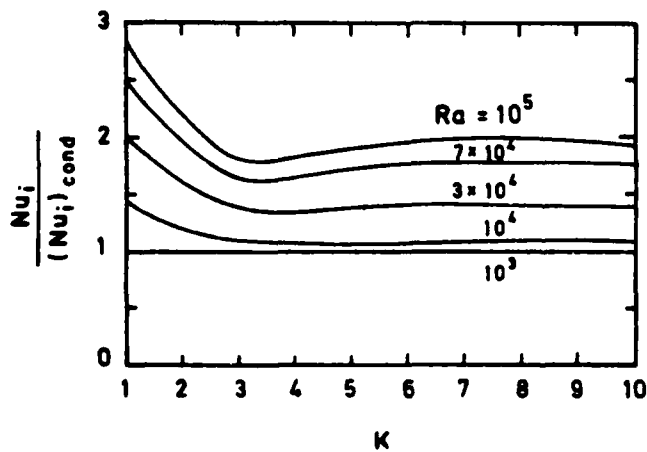


Figure 33. Variation of Ratio of $Nu_i / (Nu_i)_{cond}$ for $R' = 0.4$, $A = 1$ (Lin and Nansteel 1987b).

33. This figure shows the convective contribution to the decrease of heat transfer with increasing K for $K \leq 3.5$ and then the increase for larger K (behavior that is a direct consequence of the transition from inner to outer cell dominance). For large values of K , the ratio again decreases gradually since conduction heat transfer grows without bound while convective heat transfer is bounded. Consequently, all the curves will approach a value of unity asymptotically as $K \rightarrow \infty$.

Between horizontal concentric cylinders

Seki et al. (1975) reported their pioneer work on natural convection heat transfer between horizontal concentric cylinders of water near its maximum density. In their study the ratio of outer to inner

diameter (d_o/d_i) ranged from 1.18 to 6.39 with d_i values of 19.0, 38.0, 55.4, 69.6 and 99.7 mm and d_o of 65.5 and 121.5 mm., and the gap width $L [(d_o-d_i)/2]$ was varied from 5.0 to 51.2 mm. The surface temperature of the inner cylinder was kept at 0°C, whereas the outer cylinder surface was varied from 1° to 15°C. For each geometrical configuration, two sets of data were obtained (i.e., one set for $T_o \leq 4^\circ$, and the other set for $T_o \geq 4^\circ$).

Flow patterns

Figures 34 a, b, c, and d show a series of photographs and schematic views of flow patterns with the same $d_o = 121.5$ mm but with increasing d_i values of 38.0 to 55.4, 69.6 and 99.7 mm (i.e., with d_o/d_i

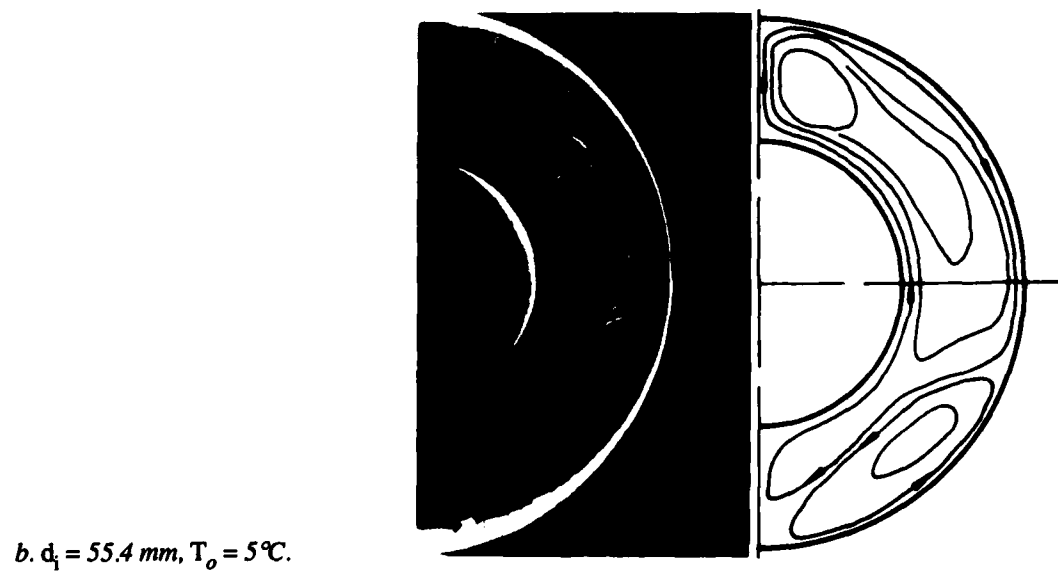
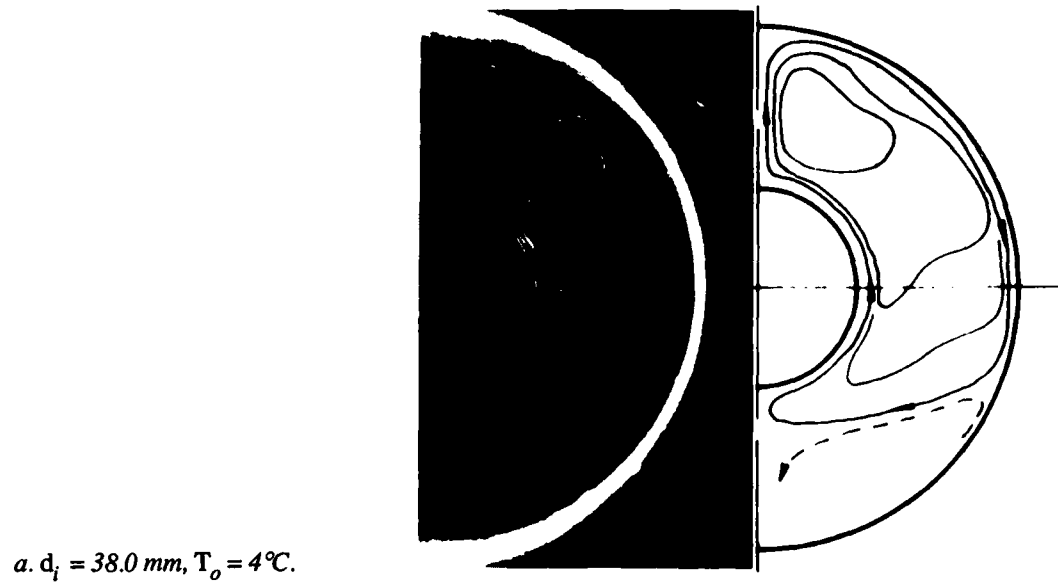
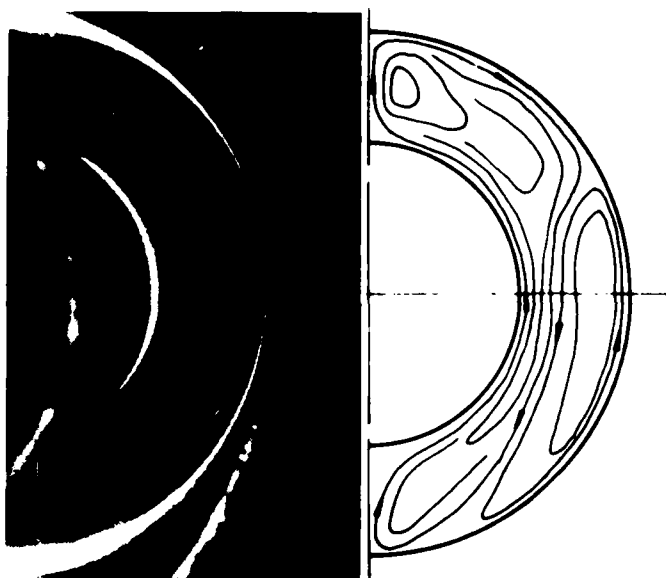
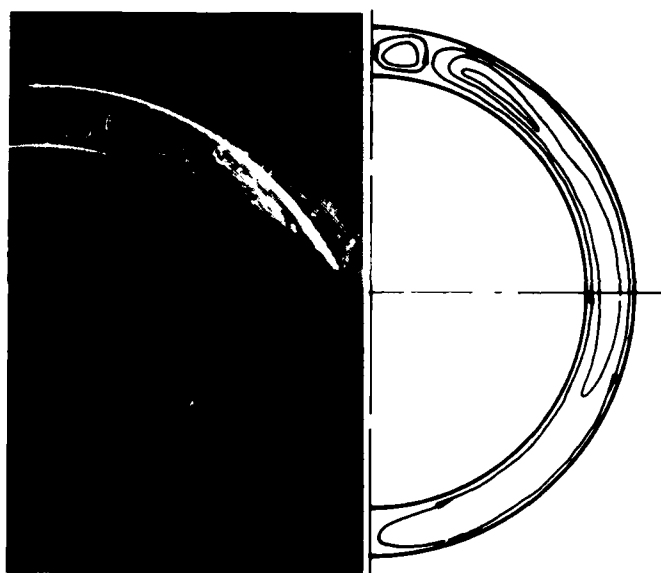


Figure 34. Photographs and schematic views of flow patterns for $d_o = 121.5$ mm (Seki et al. 1975).



c. $d_i = 69.6 \text{ mm}$, $T_o = 6^\circ\text{C}$.



d. $d_i = 99.7 \text{ mm}$, $T_o = 4^\circ\text{C}$.

Figure 34 (cont't). Photographs and schematic views of flow patterns for $d_o = 121.5 \text{ mm}$ (Seki et al. 1975).

ranging from 3.2 to 1.22 and L varying from 41.7 to 10.9). The temperature of T_o increased from 4°C in Figure 34a, to $T_o = 5^\circ\text{C}$ in Figure 34b, and $T_o = 6^\circ$ in Figure 34c; however, $T_o = 4^\circ\text{C}$ in Figure 34d, as in Figure 34a. In Figure 34a, the flow patterns are stable, with the eddy moving upward along the inner cylinder and downward along the outer cylinder. The water near the upper part of the vertical axis flows at higher speed than that on the other part in the gap. The center of the eddy is clearly observed in the upper part of the annuli, while in the lower part a secondary counter-eddy can be seen. For $T_o = 5^\circ\text{C}$ and $d_o/d_i = 2.19$ (Fig. 34b), the secondary counter-eddy in the lower part can be seen more clearly. When T_o ranges from 6° to 7°C , the influence of density inversion at 4°C becomes more evident. The eddy becomes large and finally two counter-eddies of almost equal strength exist in the gap (Fig. 34c). Flow patterns for $L = 10.9 \text{ mm}$ and $d_o/d_i = 1.22$ with $T_o = 4^\circ\text{C}$ (Fig. 34d) are considerably

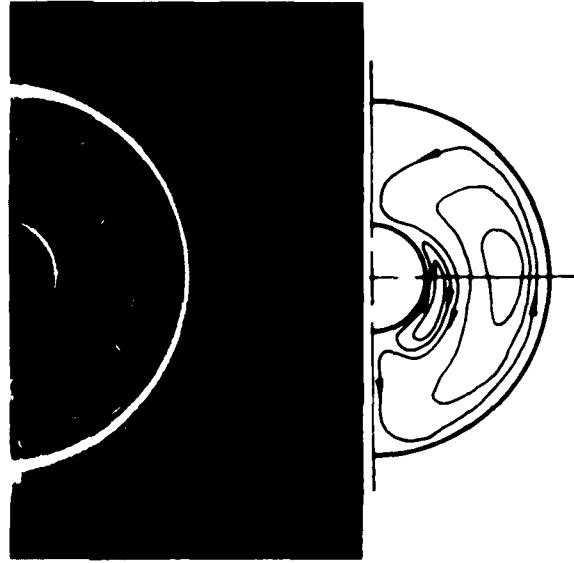


Figure 35. Photograph and schematic view for $d_o = 65.5$ mm, $d_i = 19.0$ mm and $T_o = 8^\circ\text{C}$ (Seki et al. 1975).

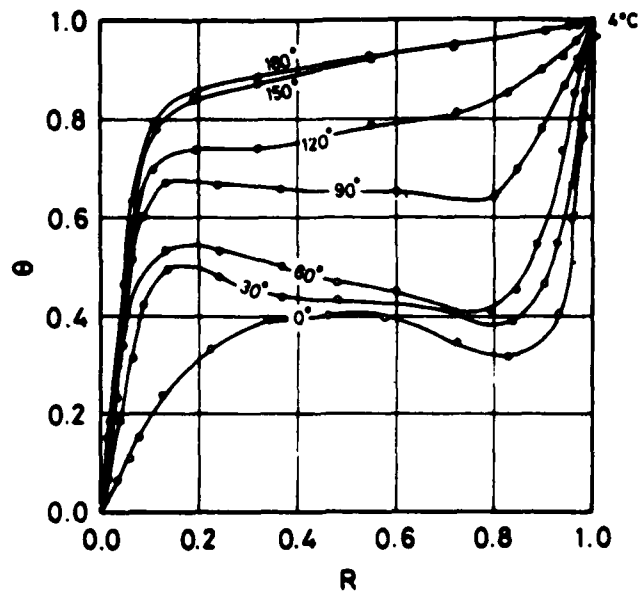
different from those in Figure 34a–c. A very small eddy that flows downward along the vertical axis is observed in the vicinity of the top annuli for all T_o . This is believed to be due to the effect of L and the cylinder curvature. Figure 35 shows the case of $d_o = 65.5$ mm, $d_i = 19.00$ mm ($d_o/d_i = 3.44$), $L = 23.2$ and $T_o = 8^\circ\text{C}$. Here the eddy is flowing upward along the outer cylinder and gradually extending its size, while the one moving upward along the inner cylinder becomes smaller and finally disappears as T_o increases.

Temperature distribution and local Nusselt number

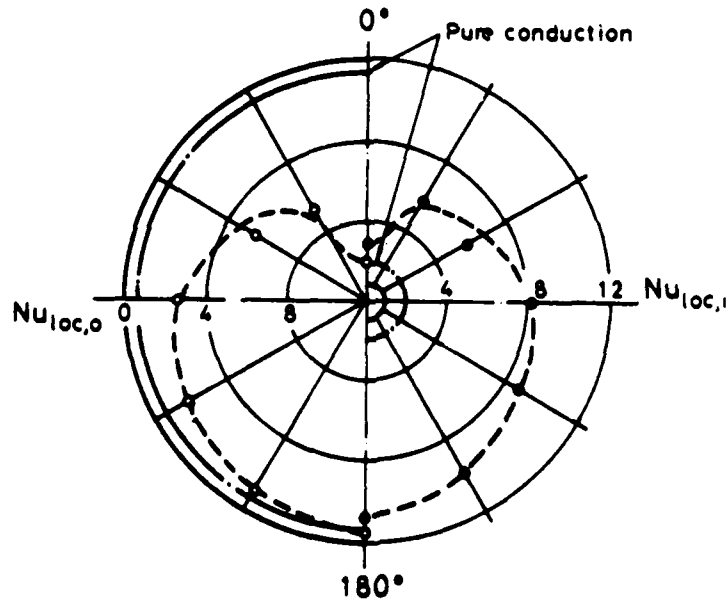
Figures 36a–38a show the effect of T_o on the dimensionless temperature distribution θ as a function of the dimensionless radius R . The corresponding local Nusselt number Nu_{loc} as a function of angular position (measured from the upper vertical axis) is shown in Figures 36b–38b. The local Nu_{loc} is defined as

$$Nu_{loc} = \frac{qL}{K\Delta T} \quad (50)$$

where q is a local heat flux. Different means were used to evaluate this quantity to determine the local Nusselt number for the inner cylinder ($Nu_{loc,i}$) and outer cylinder ($Nu_{loc,o}$). In Figure 36a, a temperature inversion is observed in the range from 0 to 90° , which is reduced as angular position increases. In the 160 – 180° range, little convective flow occurs. Figure 36b shows a minimum Nu at 0° on the inner cylinder and 180° on the outer cylinder. This phenomenon fits well with the observed temperature distribution in Figure 36a. Figure 37b shows the case of $T_o = 6^\circ\text{C}$, where two standing eddies of almost the same size coexist. The $Nu_{loc,o}$ has its lowest value at around 90° angular position, while the increase of $Nu_{loc,i}$ with increasing angular position is minimal at 0° and highest at 180° . Figure 38a is the case when $T_o = 8^\circ\text{C}$; here the temperature at 0° angular position is the highest one in the gap between the cylinders and it decreases as the angular position increases. In the range of angular position from 0° to 30° , temperature is much higher than those in either angular positions and it implies that there is a stagnant region where the conduction heat transfer is dominant. The local Nusselt number for the outer cylinder decreases as the angular position decreases and reaches a minimum value at 0° . On the other hand, the $Nu_{loc,i}$ values decreases gradually from 90° to 180° , while between 90° to 0° it increases significantly and reaches a maximum at 0° (See Fig. 38b). Figure 39 shows the variations of average Nusselt number \bar{Nu} (based on inner diameter) with $\Delta T (= T_o)$. The Nu is defined as



a. Temperature profiles.

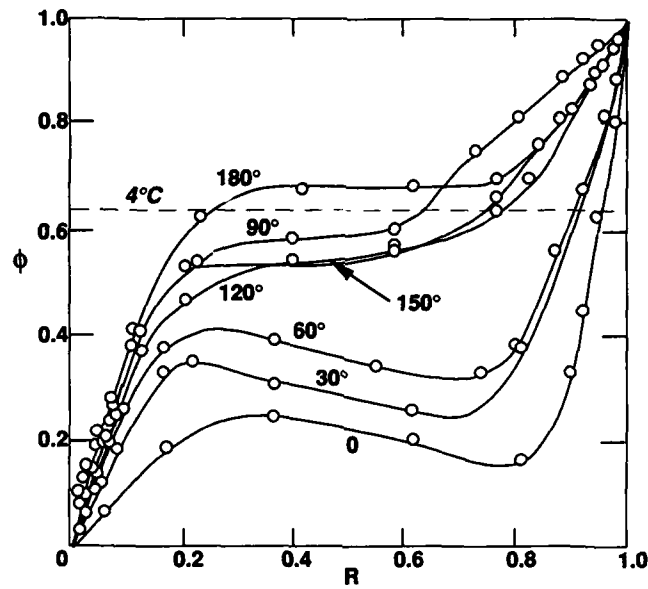


b. Local Nusselt numbers.

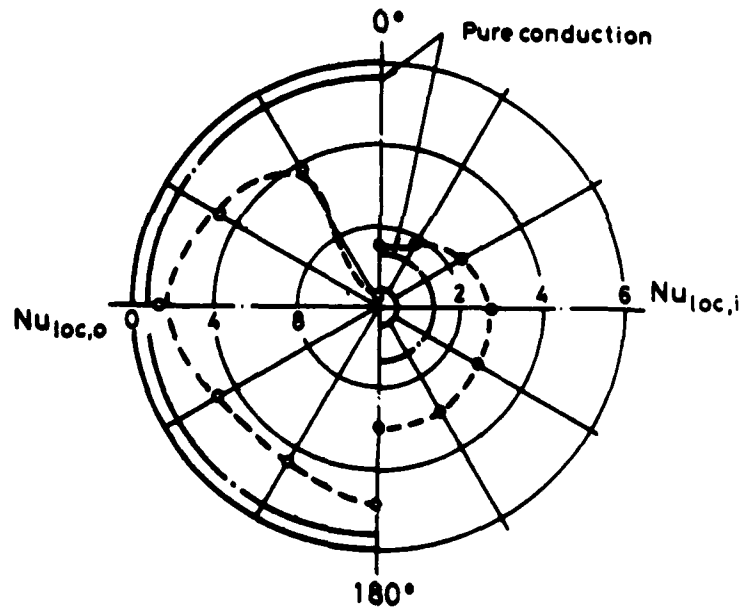
Figure 36. Temperature profiles and local Nusselt numbers for $d_o/d_i = 3.20$ and $T_o = 4^\circ\text{C}$ (Seki et al. 1975).

$$\overline{Nu} = \frac{Q_1 L}{\pi d_i \Delta T k} \quad (51)$$

where Q_1 is total heat transfer rate per unit length of the cylinder. Figure 39 shows that \overline{Nu} does not increase monotonically with increasing ΔT (as is common in fluids) when a single large eddy occupies the major portion of the gap, as in the case of $T_o \leq 4^\circ\text{C}$ or $T_o \geq 9^\circ\text{C}$. The peak value of \overline{Nu} is found at $\sim 4^\circ\text{C}$ and the minimum values appear between approximately 6° and 7°C . Values of \overline{Nu} , including minimum \overline{Nu} values, generally increase with increasing gap width L .



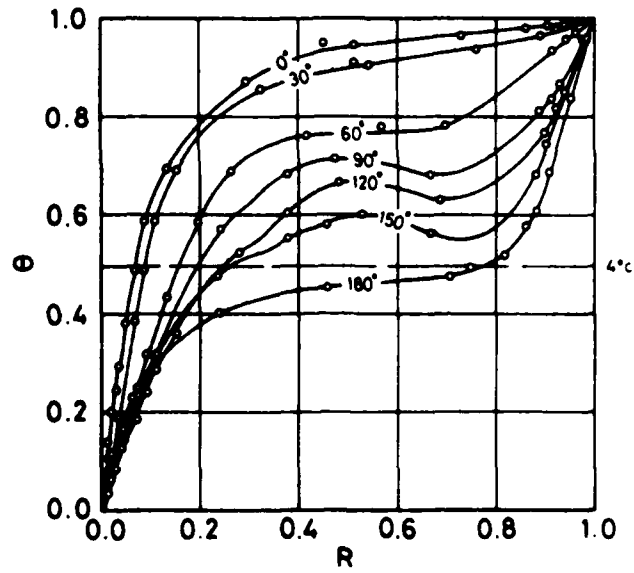
a. Temperature profiles.



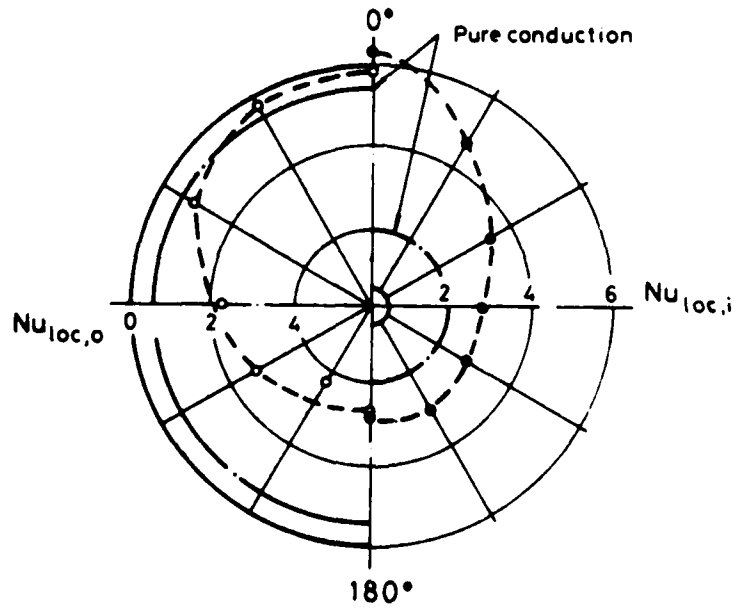
b. Local Nusselt numbers.

Figure 37. Temperature profiles and local Nusselt numbers for $d_o/d_i = 1.75$, and $T_o = 6^\circ\text{C}$ (Seki et al. 1975).

Nguyen et al. (1982) were the first to conduct an analytical study on the natural convection of cold water between two horizontal concentric cylinders with constant surface temperatures at low Rayleigh numbers. The governing equations were solved by the perturbation method and the solutions of dimensionless temperature θ' and stream function $\bar{\psi}$ were expressed as a power series of the nonlinear Rayleigh number Ra_n as



a. Temperature profiles.



b. Local Nusselt numbers.

Figure 38. Temperature profiles and local Nusselt numbers for $d_o/d_i = 3.44$ and $T_o = 8^\circ\text{C}$ (Seki et al. 1975).

$$\theta' = \sum_{m=1}^{\infty} Ra_n^{m-1} \theta'_m \quad (52)$$

$$\bar{\psi} = \sum_{m=1}^{\infty} Ra_n^m \bar{\psi}_m \quad (53)$$

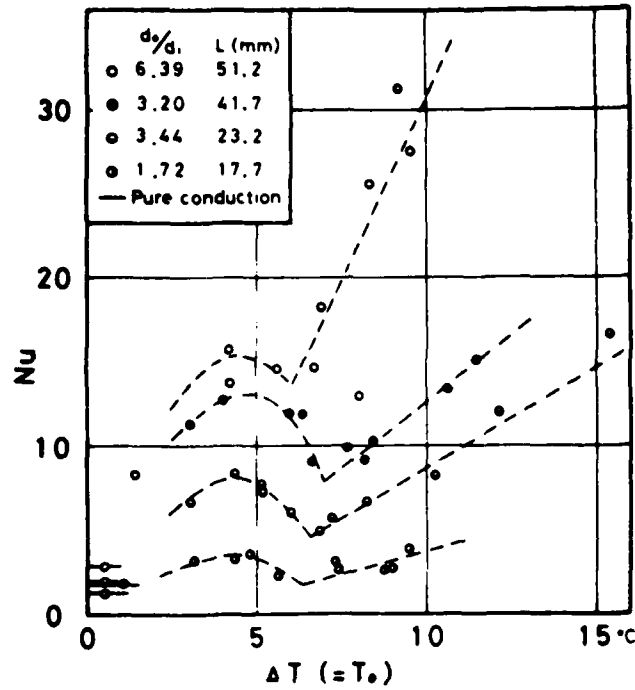


Figure 39. Variation of \overline{Nu} with ΔT (or T_o) (Seki et al. 1975).

where θ' is defined as $(T - T_o)/(T_i - T_o)$, and Ra_n is defined as

$$Ra_n = g\beta_2 r_i^3 (T_i - T_o)^2 / \nu \alpha$$

in which β_2 is the volumetric coefficient of expansion of the following density-temperature relation

$$\rho = \rho_r [1 - \beta_1 (T - T_1) - \beta_2 (T - T_r)^2] \quad (54)$$

where T_r and ρ_r are the reference temperature and density respectively. β_1 is related to β_2 by

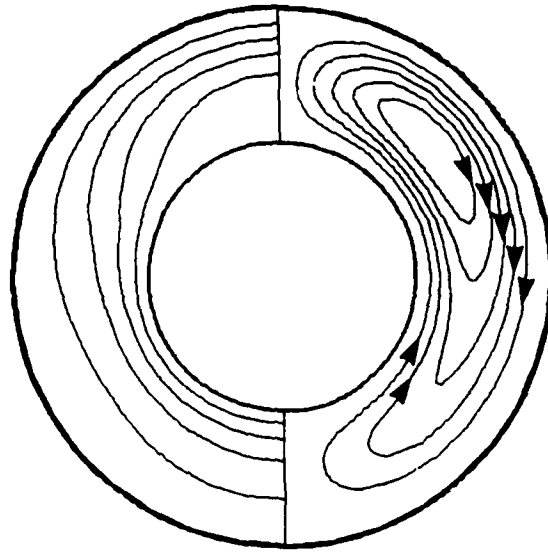
$$\beta_1 = 2(T_r - T_m)\beta_2$$

with $\beta_2 = 8 \times 10^{-6} \text{C}^{-2}$ and $T_m = 3.98^\circ\text{C}$.

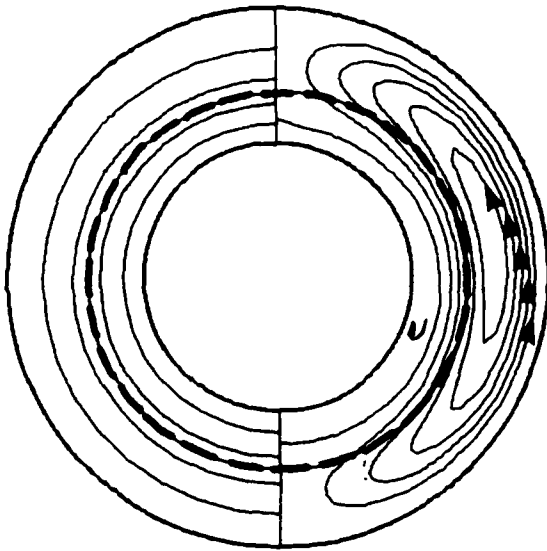
Although the disadvantage of eq 54 is its limited use for the range of temperatures from 0° to 8°C , an advantage is that this equation can predict all the essential features associated with an inversion of density by introducing just one more parameter than the equation for a classical normal fluid. Figures 40a-40c show the effect of inversion parameter γ defined as $\beta_1/\beta_2(T_i - T_o)$ or $-2(T_m - T_o)/(T_i - T_o)$ on flow patterns and isotherms in which the increments between adjacent isotherms and streamlines are, respectively,

$$\Delta\theta = \frac{(\theta_i - \theta_o)}{5} = 0.2$$

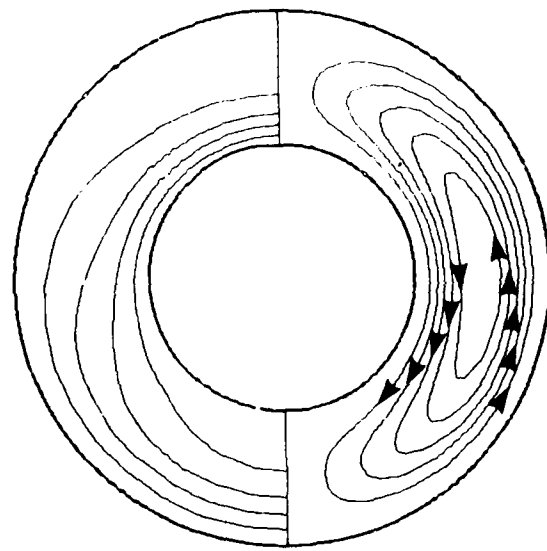
and



a. $\gamma' = 0$ and $\bar{\Psi}_{\max} = 4.6$.



b. $\gamma' = -1$, $\bar{\Psi}_{\max} = -0.045$ and $\bar{\Psi}_{\min} = -0.71$.



c. $\gamma' = -2$ and $\bar{\Psi}_{\min} = -4.8$.

Figure 40. Streamlines and isotherms for $Ra_n = 2000$, $R'' = 2$ (after Nguyen et al. 1982).

$$\Delta\bar{\Psi} = (|\bar{\Psi}_{\max}| + |\bar{\Psi}_{\min}|) / 5,$$

$\bar{\Psi}_{\max}$ and $\bar{\Psi}_{\min}$ being the values of the stream functions at the centers of the clockwise and counter-clockwise vortices, respectively.

Figure 40a shows the case when the density maximum is situated at the outer cylinder (i.e., $\gamma' = 0$). The flow consisted of two symmetrical counterrotating vortices with a downward motion near the outer cylinder. The resulting flow pattern is of a tadpole shape lying in the upper part of the annulus where the fluid motion is strongest. The maximum heat transfer occurs, however, both at the top of the outer cylinder and at the bottom of the inner cylinder. Since there is no density inversion in this case, the flow is similar to that observed in an ordinary fluid.

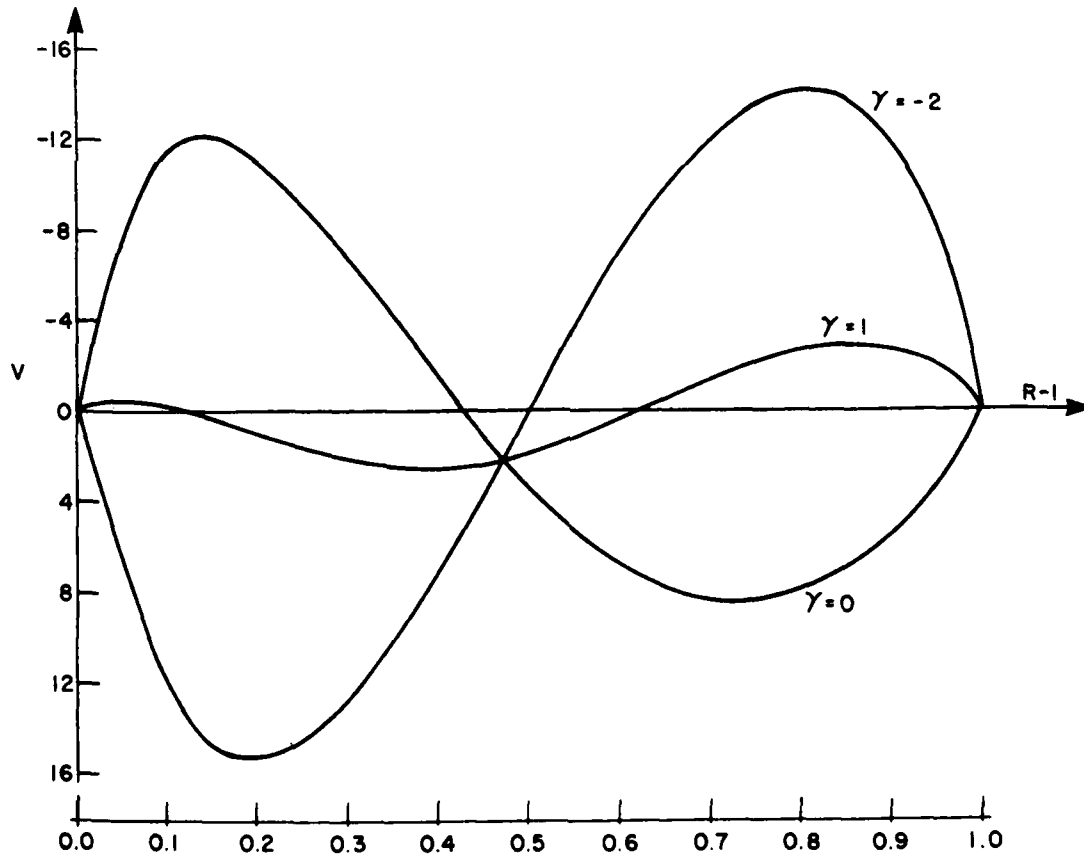
Figure 40b is the case of complete inversion with $\gamma' = -1$. The heavy dashed line represents the 4°C isotherm corresponding to the region of maximum density. In the neighborhood of this region, the fluid moves downward, while near both the inner and outer cylinders the fluid moves upward. The effect of the inversion is the sharp decrease in heat transfer as indicated by the almost concentric isotherms in contrast with the rather distorted patterns shown in Figure 40a. Figure 40c is the case of $\gamma' = -2$, (i.e., when the maximum density is situated at the inner cylinder) where the flow and isotherm patterns are just opposite to those observed in Figure 40a.

Figure 41a shows the angular velocity profiles at $\theta = 90^\circ$ for $Ra_n = 8000, R'' = 2$ with γ' as a function of $(r/r_i - 1)$. Figure 41b provides the variation of angular velocity as a function of angular position.

The effect of Ra_n on the flow and isotherms pattern can be seen by comparing Figures 42a and 40b. By increasing Ra_n , the inner cell is pushed down while the outer one moves up and gradually changes from the well-known kidney shape to that of a tadpole. The heat convection is enhanced in such a way that the isotherms are squeezed to the top of the inner cylinder and to the bottom of the outer one. The effects of changing radius ratio $[R' = (r_o/r_i)]$ on the inversion phenomenon can be seen from Figures 42a and 42c or 42b and 42d.

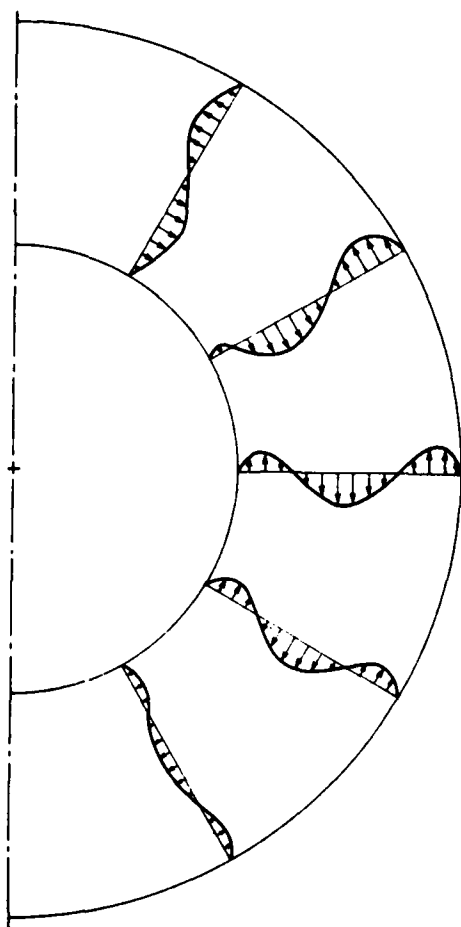
An average or overall Nusselt number can be defined as

$$\overline{Nu} = 1 + \epsilon Ra_G^2 \quad (55)$$



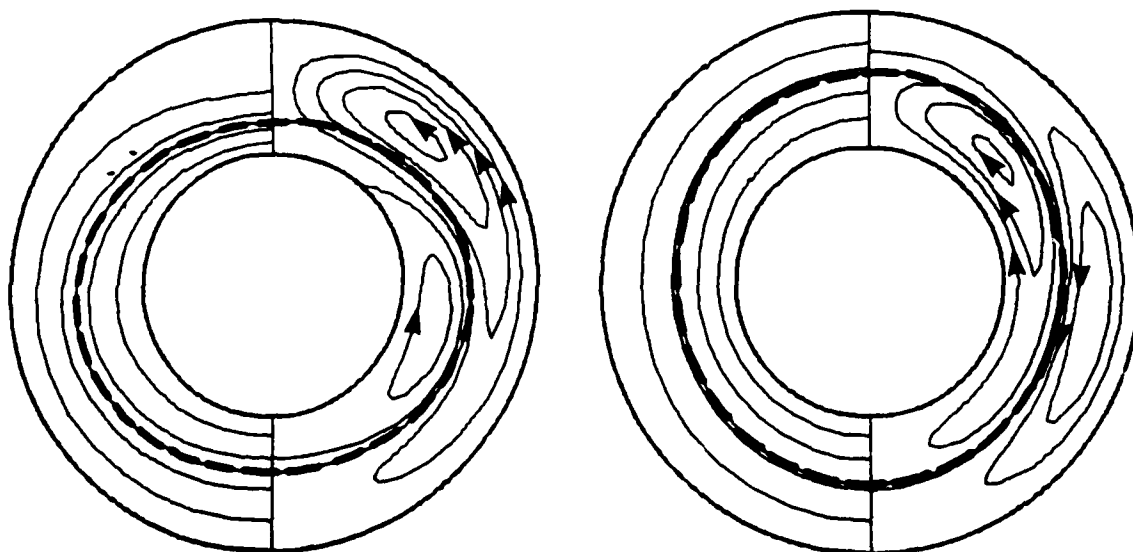
a. $\phi = 90^\circ$ with γ' as a parameter.

Figure 41. Angular velocity profiles for $Ra_n = 8000$ and $R'' = 2$ (Nguyen et al. 1982).



b. $\gamma' = -1$ at various angular positions.

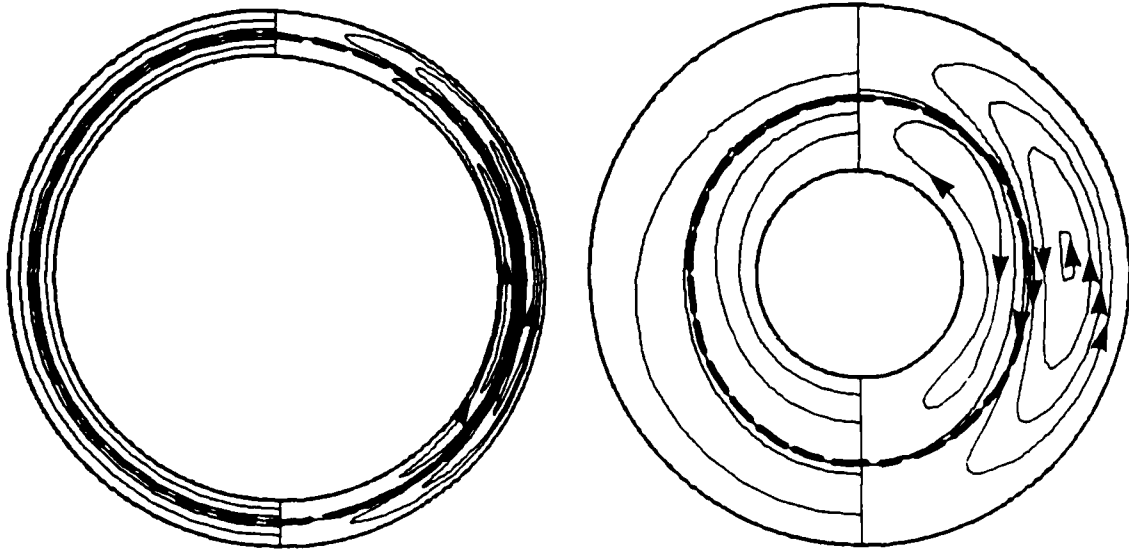
Figure 41 (cont'd). Angular velocity profiles for $Ra_n = 8000$ and $R'' = 2$ (Nguyen et al. 1982).



a. $R'' = 2, \gamma' = -1, \bar{\psi}_{\max} = 1.1$ and $\bar{\psi}_{\min} = -2.7$.

b. $R'' = 2, \gamma' = -0.857, \bar{\psi}_{\max} = 1.5$ and $\bar{\psi}_{\min} = -1.4$.

Figure 42. Streamlines and isotherms for $Ra_n = 8000$ (Nguyen et al. 1982).



c. $R'' = 1.2, \gamma' = -1, \bar{\psi}_{\max} = 0.0087, \text{ and } \bar{\psi}_{\min} = -0.013$. d. $R'' = 2.6, \gamma' = 0.857, \bar{\psi}_{\max} = 3.2 \text{ and } \bar{\psi}_{\min} = -6.7$.

Figure 42 (cont'd).

where Ra_G is the Rayleigh number based on gap width ($r_o - r_i$), i.e.,

$$Ra_G = g\beta_2(r_o - r_i)^3(T_i - T_o)^2/\nu\alpha$$

where $\beta_2 = 3 \times 10^{-6} \text{ } ^\circ\text{C}^{-2}$ and ϵ is a function of R'' and γ' . Equation 55 explicitly shows that the overall Nusselt number is made of two terms, the first term representing heat transfer due to pure conduction and the second arising from heat transfer by convection. Figure 43 shows the effects of density inversion, for R'' values ranging from $R'' = 1.25$ to 10 , on the overall convective heat transfer coefficient $\epsilon = (Nu - 1)/Ra_G^2$. All three curves present a very sharp minimum in the vicinity of $\gamma' = -1$, indicating a deep cut of the heat transfer rate due to the complete inversion of fluid density. For example, the minimum value of ϵ at $\gamma' = -1$ is about 10^3 times smaller than the value of ϵ at $\gamma' = -2$. This steep drop is essentially due to the presence of two counterrotating vortices that arise from the inversion of the fluid density.

Vasseur et al. (1983) extended Nguyen et al.'s (1982) and Seki et al.'s (1975) experimental work by conducting an analytical study of the same problem. Vasseur et al. (1983) assumed symmetry along the vertical plane through the axis, neglecting the viscous dissipation and compressibility effects. All fluid properties except the water density were taken to be constant and evaluated at the arithmetic mean temperature of the two cylinders. The governing equations for the present problem, using the Oberbeck-Boussinesq approximation, are

$$\frac{\partial \Omega}{\partial \tau} + \frac{1}{R''} \left[\frac{\partial (UR''' \Omega)}{\partial R'''} + \frac{\partial (\Omega V)}{\partial \phi} \right] = Pr \nabla^2 \Omega + A \left[\sin \phi \frac{\partial \bar{\Delta p}}{\partial R'''} + \frac{\cos \phi}{R'''} - \frac{\partial \bar{\Delta p}}{\partial \phi} \right] \quad (56)$$

$$\frac{\partial \theta}{\partial \tau} + \frac{1}{R'''} \left[\frac{\partial (UR''' \phi)}{\partial R'''} + \frac{\partial (V \theta)}{\partial \phi} \right] = \nabla^2 \theta \quad (57)$$

$$\Omega = \nabla^2 \psi \quad (58)$$

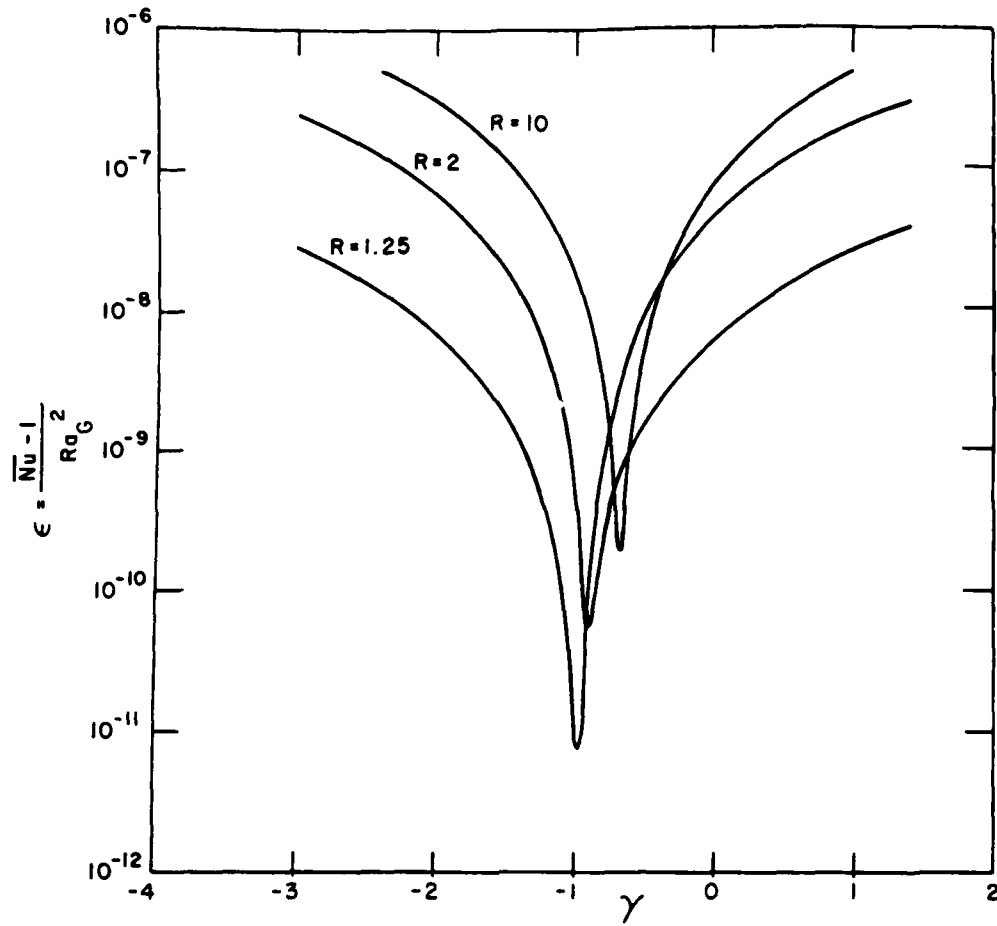


Figure 43. Coefficient of convective heat transfer ϵ as function of γ' and R'' (Nguyen et al. 1982).

$$U = \frac{1}{R'''} \frac{\partial \psi}{\partial \phi}, \quad V = - \frac{\partial \psi}{\partial R'''} \quad (59)$$

The initial and boundary conditions are

$$U = V = \psi = \Omega = 0; \quad \theta = 0, \text{ at } \tau = 0$$

$$U = V = \psi = 0; \quad \theta = 0, \quad 0 < \phi < \pi, \quad R''' = \frac{1}{R'' - 1} \quad (60)$$

$$U = V = \psi = 0; \quad \theta = 1, \quad 0 < \phi < \pi, \quad R''' = \frac{R''}{R'' - 1}$$

$$\frac{\partial U}{\partial \phi} = V = \psi = \Omega = 0; \quad \frac{\partial \theta}{\partial \phi} = 0 \text{ at } \phi = 0, \pi \text{ (symmetry lines)}$$

where Ω = dimensionless vorticity, $\omega L^2/\alpha$

ω = the vorticity

L = the gap width ($r_0 - r_i$)

- R''' = dimensionless radial coordinate, r/L
 U, V = dimensionless radial and angular velocity, uL/α and vL/α
 u, v = radial and angular velocity
 α = the thermal diffusivity
 ϕ = the angular coordinate,
 $\bar{\Delta}\rho$ = defined as $[\bar{\rho} - \rho(\theta)]/\bar{\rho}$
 ρ = the water density
 $\bar{\rho}$ = an average water density.
 θ = dimensionless temperature, $(T-T_i)/\Delta T$ ($\Delta T = T_o - T_i$)
 ψ = dimensionless stream function ($= \bar{\psi}/\alpha$)
 $\bar{\psi}$ = the stream function
 R'' = radius ratio (r_o/r_i).

This work covers a temperature range from 0° to 20°C with the density–temperature relation represented by

$$\frac{\rho_o}{\rho} = 1 + \beta'_1 T + \beta'_2 T^2 + \beta'_3 T^3 + \beta'_4 T^4 \quad (61)$$

where $\rho_o = 0.9998396$ (g/cm³) is water density at 0°C, with β' values given by

$$\begin{aligned}
 \beta'_1 &= -0.6789452 \times 10^{-4} (1/^\circ\text{C}) \\
 \beta'_2 &= 0.907294338 \times 10^{-5} (1/^\circ\text{C}^2) \\
 \beta'_3 &= 0.964568125 \times 10^{-7} (1/^\circ\text{C}^3) \\
 \beta'_4 &= 0.873702983 \times 10^{-9} (1/^\circ\text{C}^4).
 \end{aligned}$$

A nonlinear Rayleigh number Ra_n and an inversion parameter γ' were used to characterize their computed results:

$$Ra_n = \frac{A}{(R'' - 1)^3} \frac{\beta'_2}{Pr} \Delta T^2 \quad (62)$$

and

$$\gamma' = 2 \left(\frac{T_m - T_o}{\Delta T} \right) \quad (63)$$

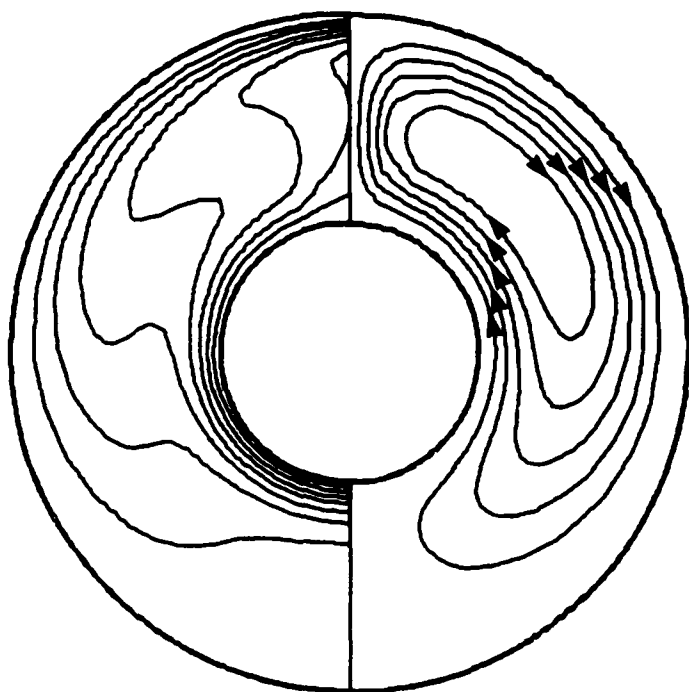
where A = a size parameter defined as gL^3/α^2

β_2 = a coefficient defined in eq 61

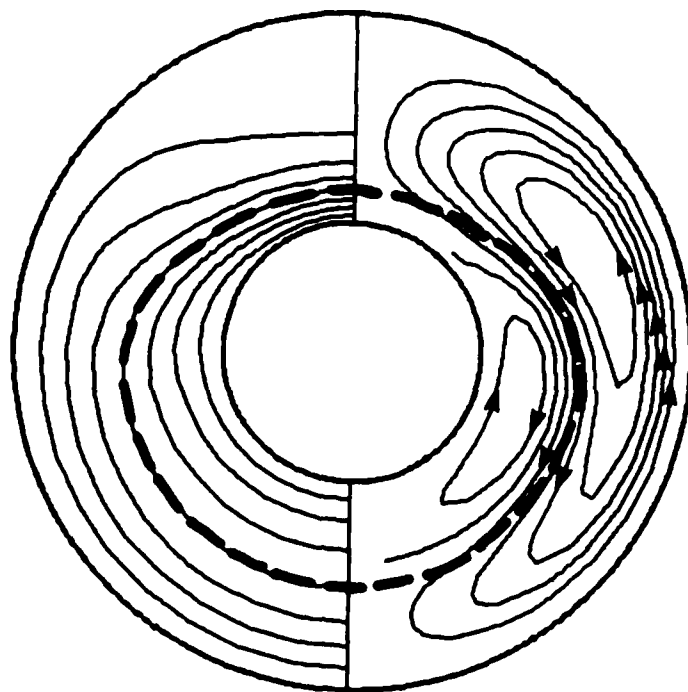
$$\Delta T = T_o - T_i$$

and γ' is related to R' defined in eq 43 by $\gamma' = -2R'$.

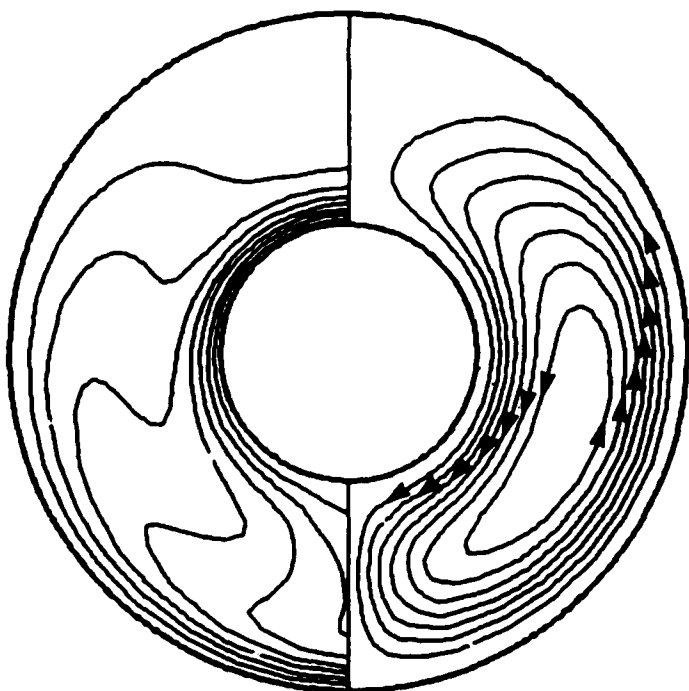
In their study, the value of γ' varies between $-2 \leq \gamma' \leq 0$. When $\gamma' = -1$, T_m is half way between T_o and T_i and the densities on the inner and outer cylinder are the same. When $\gamma' \leq -2$ and $\gamma' \geq 0$, no inversion occurs. When $|\gamma'| \gg 1$ the fluid behavior tends to that of a common fluid with a linear equation of state. Figures 44a–44d show the variation of the isotherm and streamlines as a function of Ra_n , R'' and γ' . In Figure 44a, $\gamma' = 0$ (i.e., $T_o = 4^\circ\text{C}$), and the fluid near the outer cylinder is heavier and therefore is moving downward while the relatively higher fluid near the inner cylinder is moving upward (this is nearly equivalent to Fig. 34a and 36a). The distortion of isotherms reveals a strong convective motion in the cavity. The maximum heat transfer, indicated by closely spaced isotherms,



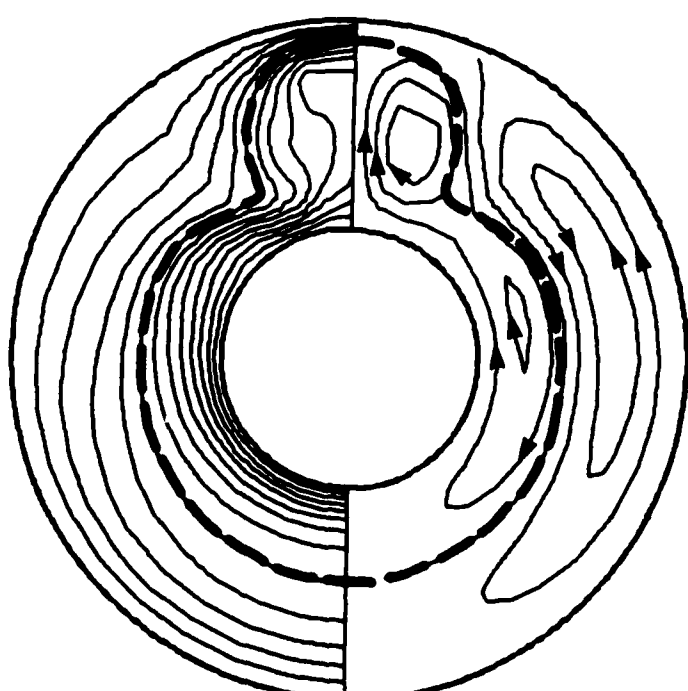
a. $Ra_n = 6350, R'' = 2.6, \gamma' = 0; \bar{\psi}_{\max} = 5.50, \Delta\bar{\psi} = 0.583.$



b. $Ra_n = 6350, R'' = 2.6, \gamma' = -1; \bar{\psi}_{\max} = 1.80, \bar{\psi}_{\min} = -0.0012, \Delta\bar{\psi} = 0.225.$



c. $Ra_n = 6350, R'' = 2.6, \gamma' = -2.0; \bar{\psi}_{\max} = 1.90, \Delta\bar{\psi} = 0.238.$



d. $Ra_n = 17250, R'' = 2.6, \gamma' = -0.77; \bar{\psi}_{\max} = 6.70, \bar{\psi}_{\min} = -0.75$ and $\Delta\bar{\psi} = 1.242.$

Figure 44. Variation of isotherms and streamlines as function of Ra_n, R'' and γ' (Nguyen et al. 1982).

occurs at the top of the cavity for the outer cylinder and at the bottom of the inner one. Figure 44b has the same parameters of Ra_n , R'' , but γ' is changed from 0 to -1 (this is equivalent to Fig. 38a and 38b). The flow pattern is a direct consequence of the maximum density of water at 4°C (the heavy dashed line represents the 4°C isotherm and this define the regions of maximum density). The convective motion inside the cavity is now considerably lessened as compared with the case of $\gamma' = 0$.

Figure 44c depicts the case of $\gamma' = -2$ (this is the case when $T_i = T_m$). The local heat transfer is maximal at the bottom of the outer cylinder and at the top of the inner one. This situation is completely opposite the case described in Figure 44a. For the limited range of $-0.75 < \gamma' \leq 0.90$, the tendency for the clockwise circulation pattern to form two cells is shown in Figure 44d. The distortion of the isotherm pattern in the upper part of the cavity is the result of the intensive convection generated by the clockwise vortex located in the region. This is somewhat similar to the flow patterns exhibited in Figure 34c.

Figure 45a shows the variation of dimensionless temperature θ as a function of dimensionless radius R for $Ra_n = 6350$, $R'' = 2.6$ and $\gamma' = 0$. The temperature distribution is very similar to those of the experimental values shown in Figure 36a. Figure 45b is the corresponding local Nusselt number distribution as a function of angular coordinate. The $Nu_{loc,o}$ reaches a minimum at 180° while the inner cylinder has a minimum heat transfer at 0° (this is nearly identical to the distributions shown in Fig. 36b).

The values of $Nu_{loc,i}$ and $Nu_{loc,o}$ are defined as

$$Nu_{loc,i} = -\ln R'' \left[R + \frac{\partial \theta}{\partial R^+} \right]_{R^+ = R_i^+ = 1/(R'' - 1)} \quad (64)$$

and

$$Nu_{loc,o} = \ln R'' \left[R + \frac{\partial \theta}{\partial R^+} \right]_{R^+ = R_o^+ = R''/(R'' - 1)} \quad (65)$$

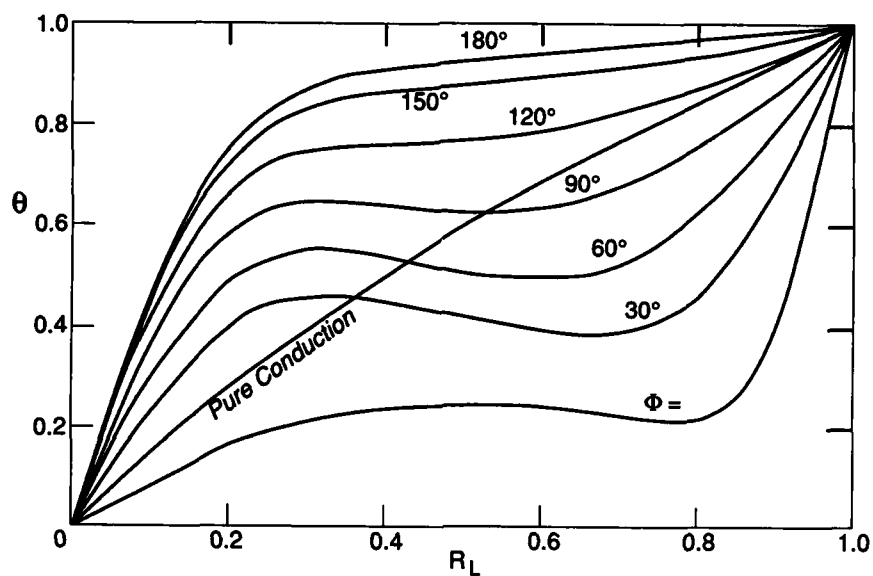
An overall average \overline{Nu} can be expressed as

$$\begin{aligned} \overline{Nu} &= -\frac{\ln R''}{\pi} \int_0^\pi \left[R + \frac{\partial \theta}{\partial R^+} \right]_{R^+ = 1/(R'' - 1)} d\phi \\ &= -\frac{\ln R''}{\pi} \int_0^\pi \left[R + \frac{\partial \theta}{\partial R^+} \right]_{R^+ = R''/(R'' - 1)} d\phi. \end{aligned} \quad (66)$$

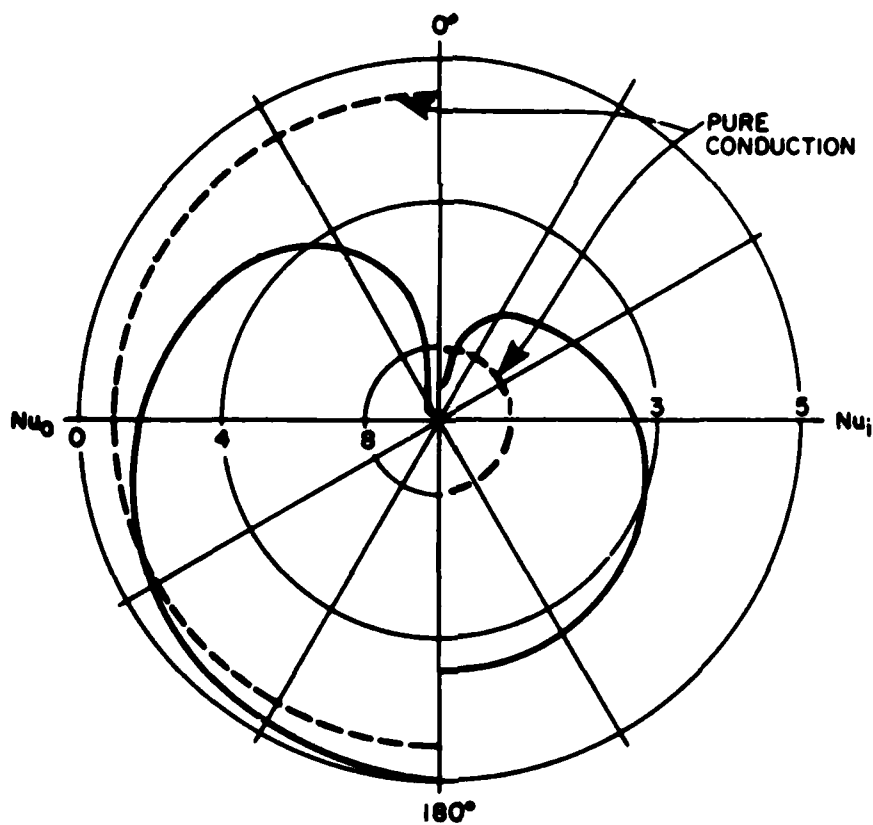
Figure 46a shows the effect of nonlinear Rayleigh number on \overline{Nu} as a function of γ' for the case of $R'' = 2.6$, where \overline{Nu} and the minimum \overline{Nu} values increase as Ra_n increases. For all the Ra_n range studied, the minimum \overline{Nu} occurred at γ' values somewhat greater than -1 (≈ -0.75). The influence of R'' on \overline{Nu} is shown in Figure 46b for the case $Ra_n = 10^4$. It is clearly shown that \overline{Nu} occurs at values of $\gamma' > -1$ but approaches $\gamma' = -1$ as R'' increases.

In a square enclosure

Watson (1972) performed the first analysis on the effect of inversion temperature on the convection of water in an enclosed square cavity. In this study, the effect of temperature-dependent

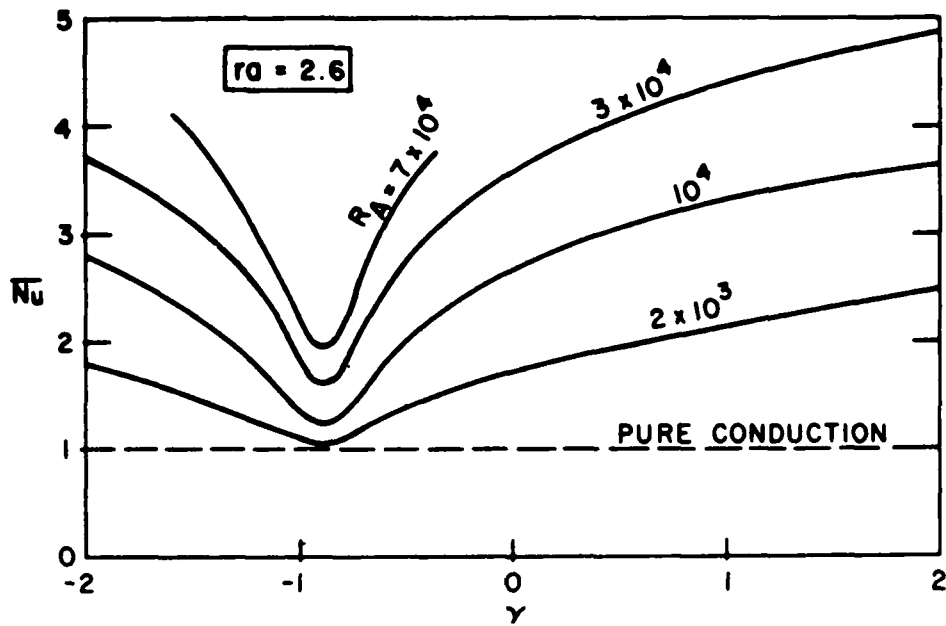


a. Temperature profile.

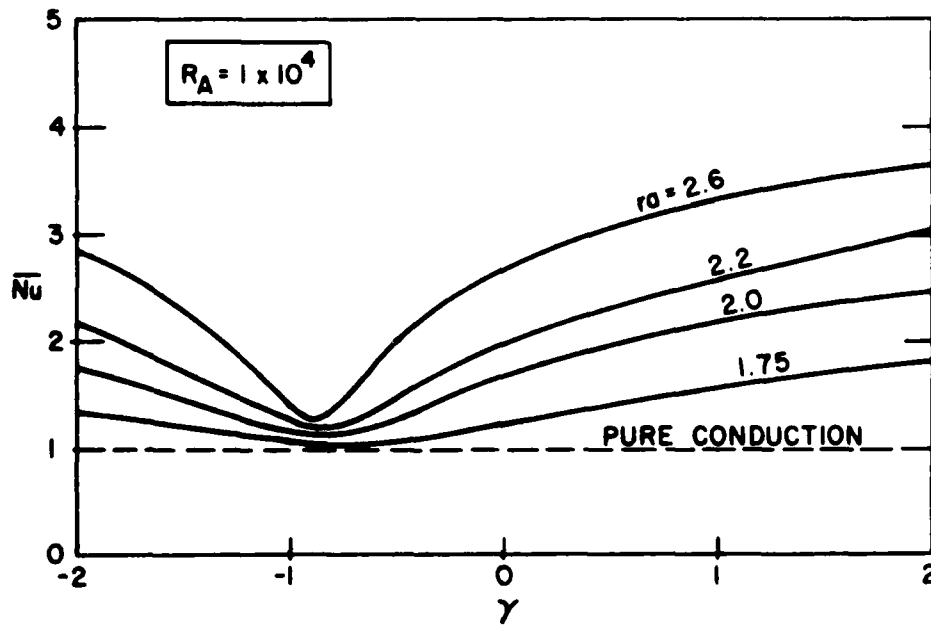


b. Distribution of local Nusselt number.

Figure 45. Variation of dimensionless temperature θ as function of dimensionless radius, R for $Ra_n = 6350$, $R'' = 2.6$ and $\gamma' = 0$ (Nguyen et al. 1982).



a. For $R'' = 2.6$ with Ra_n as parameter.



b. For $Ra_n = 1 \times 10^4$ with R'' as parameter.

Figure 46. Variation of overall Nusselt number \bar{Nu} with γ' (Nguyen et al. 1982).

viscosity was found to result in changes in magnitude rather than the characteristics of the flow. The decrease in viscosity in the vicinity of the hotter wall, accompanied by higher fluid velocities, gave rise to the increases in heat transfer indicated by the dashed curve in Figure 47. It can be seen that the Boussinesq model displayed a completely different heat transfer phenomenon in a system containing a density extremum.

Lin and Nansteel (1987a) analyzed the problem of natural convective heat transfer in a square enclosure that contained water near its density maximum. The square enclosure had two sides of length

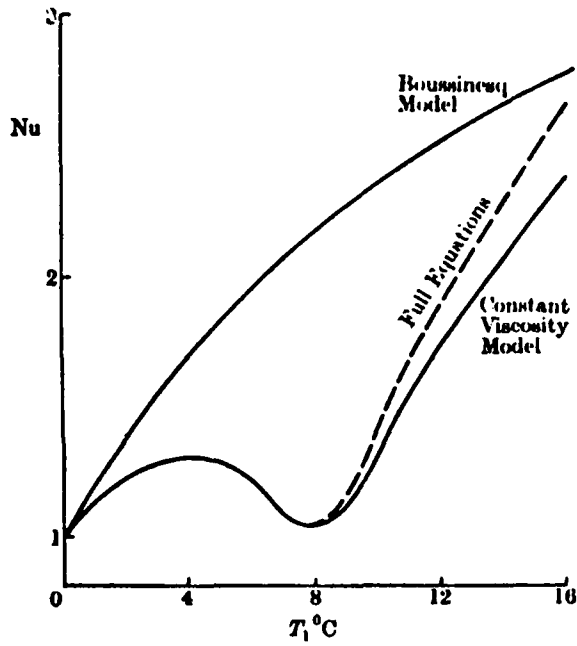


Figure 47. Comparison of Nu from Boussinesq model, full equation and constant viscosity model as function of T_1 (Watson 1972).

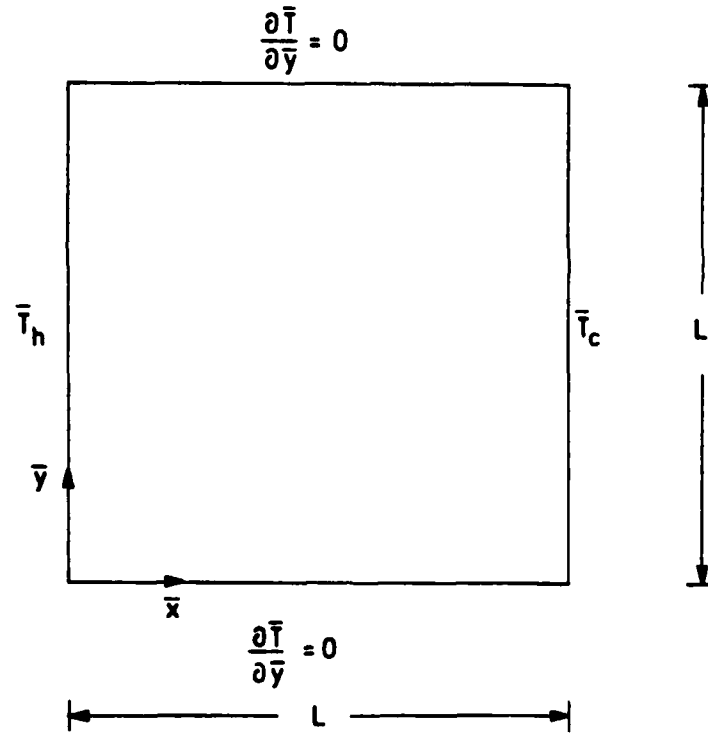


Figure 48. Schematics of the square enclosure with thermal conditions (Lin and Nansteel 1987a).

L with the two opposing vertical walls maintained at T_h and T_c for the temperature range $0^\circ \leq T_c < T_h \leq 20^\circ\text{C}$. The horizontal walls were insulated (see Fig. 48). The enclosure was supposed to be sufficiently deep to ensure an essentially identical flow field in planes of different depth. In addition, the following assumptions were made: 1) the flow is laminar and two dimensional, 2) physical properties, except for the density in the buoyancy force term, are constant and evaluated at the cold wall temperature T_c , and 3) the viscous dissipation can be neglected.

The dimensionless governing equations are

$$\frac{D\xi}{D\tau} = \frac{Ra''' }{Pr} q |\theta - R|^{q-2} (\theta - R) \frac{\partial \theta}{\partial X} + \nabla^2 \xi \quad (67)$$

$$\frac{D\theta}{D\tau} = \frac{1}{Pr} \nabla^2 \theta \quad (68)$$

$$\nabla^2 \psi = -\xi. \quad (69)$$

The initial and boundary conditions are

$$U = V = 0, \quad \theta = \frac{1}{2}, \quad \text{at } \tau = 0$$

$$\theta(0, Y) = 1, \quad \theta(1, Y) = 0, \quad \text{at } \tau > 0$$

$$\frac{\partial \theta}{\partial Y}(X, 0) = \frac{\partial \theta}{\partial Y}(X, 1) = 0. \quad (70)$$

$$\psi = \frac{\partial \psi}{\partial X} = \frac{\partial \psi}{\partial Y} = 0 \quad \text{on the boundary with the dimensionless variables defined as}$$

$$X = \frac{x}{L}, \quad Y = \frac{y}{L}$$

$$U = \frac{uL}{v}, \quad V = \frac{vL}{v}, \quad \theta = \frac{T_1 - T_c}{T_h - T_c}$$

$$\psi = \frac{\bar{\psi}}{v}, \quad \xi = \frac{\bar{\xi} L^2}{v}, \quad \tau = \frac{v t}{L^2}$$

in which $\bar{\psi}$ is the stream function, and $\bar{\xi}$ is the vorticity. Additional dimensionless parameters appearing in eq 67 and 68 are the Rayleigh and Prandtl numbers:

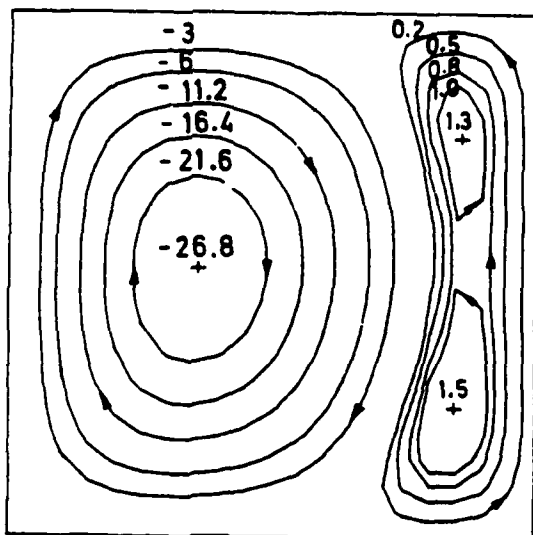
$$Ra''' = \frac{g \rho_m \alpha_1 L^3 (T_h - T_c)^q}{\rho_c v \alpha}, \quad Pr = \frac{v}{\alpha}$$

in which α_1 and q are from the density-temperature relation

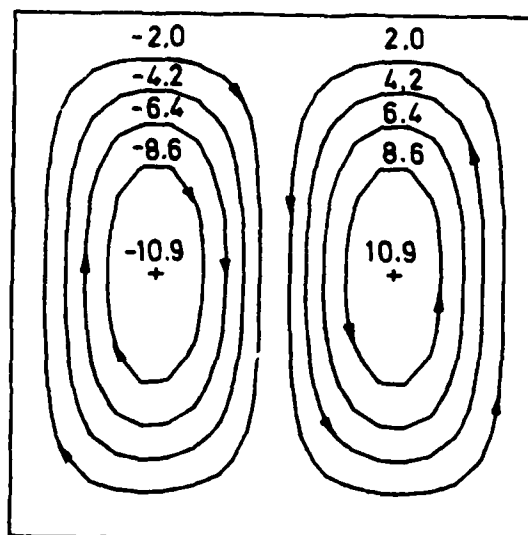
$$\rho = \rho_m [1 - \alpha_1 |T - T_m|^q] \quad (71)$$

with $\rho_m = 999.9720 \text{ kg m}^{-3}$, $\alpha_1 = 9.297173 \times 10^{-6} (\text{°C})^{-q}$, $T_m = 4.029325 \text{°C}$ and $q = 1.894816$. The density distribution parameter is defined as

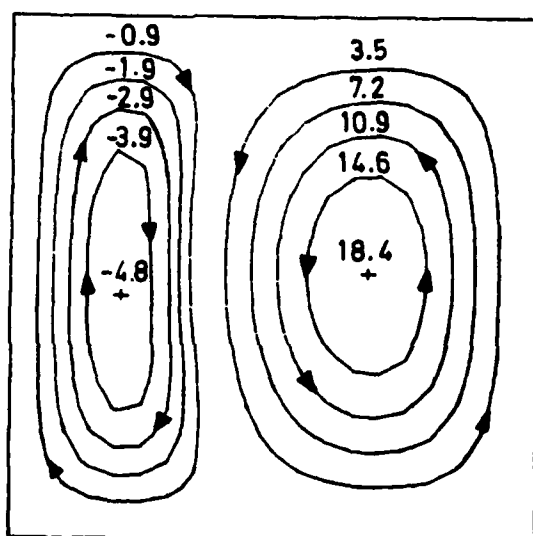
$$R' = \frac{T_m - T_c}{T_h - T_c} \quad (72)$$



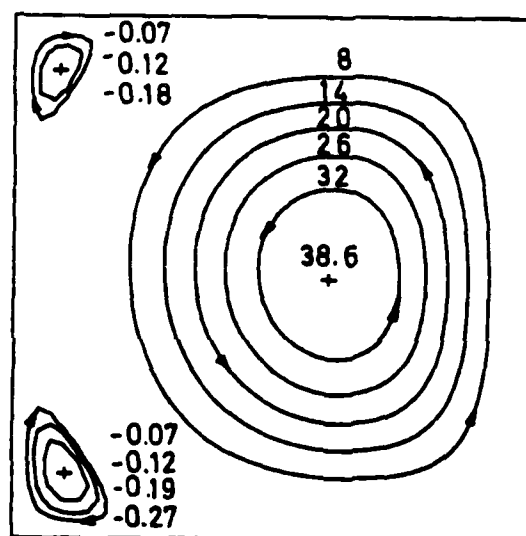
$R' = 0.4$



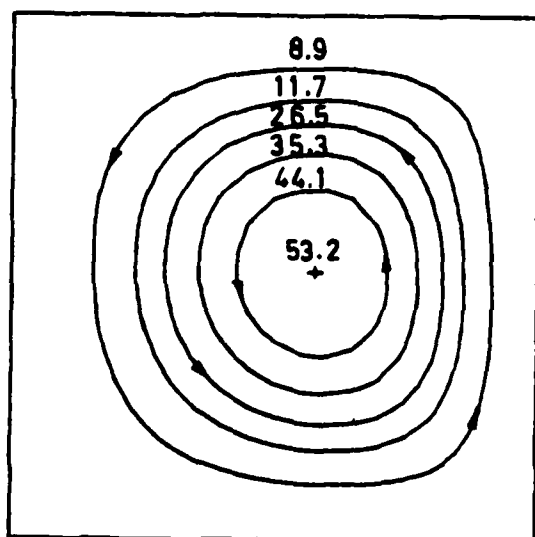
$R' = 1/2$



$R' = 0.55$



$R' = 2/3$



$R' = 3/4$

Figure 49. Dimensionless stream function ($\psi \times 10^3$) for $Ra''' = 10^3$ with $R' = 0.4, 0.5, 0.55, 2/3$ and $3/4$ (Lin and Nansteel 1987a).

which is equivalent to $-1/2 \gamma'$ defined in eq 63. In the case $R' < 0$ (i.e., for the condition of $T_h > T_c > T_m$), the fluid density increases monotonically with X across the enclosure. The density distribution results in a clockwise circulation pattern. When $R' > 1$ (i.e., for $T_m > T_h > T_c$), the distribution is reversed, and hence a counterclockwise pattern results. When R' is in the range of $0 < R' < 1$, density increases to $\rho = \rho_m$ at $T = T_m$ and then decreases. Hence, this heavier fluid in the enclosure interior descends while the lighter fluid adjacent to vertical boundaries ascends, giving rise to a pair of counterrotating vortices arranged horizontally in the enclosure.

Streamlines and isotherms

For small values of Ra''' , the inertial effects are relatively unimportant, and so an approximate balance between viscous and buoyancy forces results. Figure 49 shows a series of dimensionless streamlines for $Ra''' = 10^3$ but for a range of R' values from 0.4, 0.5, 0.55, $2/3$ and 0.75. At $Ra''' = 10^3$, the temperature fields deviate from the pure conduction field; i.e., $\theta = 1 - X$ only slightly. However, the convection effects on the temperature fields increase as $|R' - 1/2|$ increases. As R' increases (or decreases), the maximum density contour moves toward the hot (or cold) wall. As a result, the counterclockwise-rotating cell on the right for the case of $R' = 0.4$ becomes stronger and larger at the expense of the clockwise-rotating cell on the left as R' increases. For $R' = 2/3$, the cell on the left was divided into two separate clockwise-rotating cells in the upper and lower left-hand corners of the enclosure. In this case, although the maximum density contour ($\theta_m = 2/3$) is located approximately at $X = 1/3$, upward flow on the hot walls occurs only near the corners of the enclosure. The circulation of the counterclockwise right-hand vortex has become so strong that it drags (by virtue of the fluid's viscosity) relatively light fluid down along the hot walls. When $\theta_m = R' = 3/4$, even the two tiny corner cells are eliminated by the strong counterclockwise-rotating cell on the right, resulting in a completely unicellular flow. In the instance $R' = 1$, density increases with temperature and hence decreases with X , resulting in a single counterclockwise rotating cell.

Figure 50 shows the ψ and θ fields for $R' = 1/2$ and $Ra''' = 10^4$ and 10^6 . The bicellular flow structure observed for $Ra''' = 10^3$ and $R' = 1/2$ still prevails for $10^4 \leq Ra''' \leq 10^6$ with the cells becoming more angular in shape. The flows in the left and right halves of the enclosure are identical except for the opposite direction of rotation. The large temperature gradients near $X = 1/2$, $Y \leq 1$ are due to the internal circulation of the two counterrotating cells that bring warm and cold water from the hot and cold walls, respectively.

For a slight increase in R' from $R' = 1/2$ to $R' \approx 0.55$, there is no spatial symmetry (see Fig. 51) because the maximum density contour $\theta_m = R' = 0.55$ has now shifted toward the hot wall. The large counterclockwise cell adjacent to the cold wall becomes more dominant. Cold water is swept across the upper boundary and into the upper left-hand corner, which shifts the maximum density contour $\theta_m = 0.55$ toward the hot wall in the upper half of the enclosure. As a result, there is no upflow along the upper portion of the hot wall for $Ra''' = 10^6$ because the strong counterclockwise vortex overcomes the (upward) buoyancy force in the fluid directly adjacent to the upper portion of the hot wall.

Heat transfer

The local heat flux in the horizontal direction can be expressed as the superposition of conductive and convective modes, i.e.,

$$q = -k \frac{\partial T}{\partial x} + \rho_0 c_p (T - T_c) u. \quad (73)$$

Expressed in dimensionless form, the Nusselt number can be rewritten as

$$Nu(X, Y) = \frac{qL}{k(T_h - T_c)} = -\frac{\partial \theta}{\partial X} + Pr \theta U. \quad (74)$$

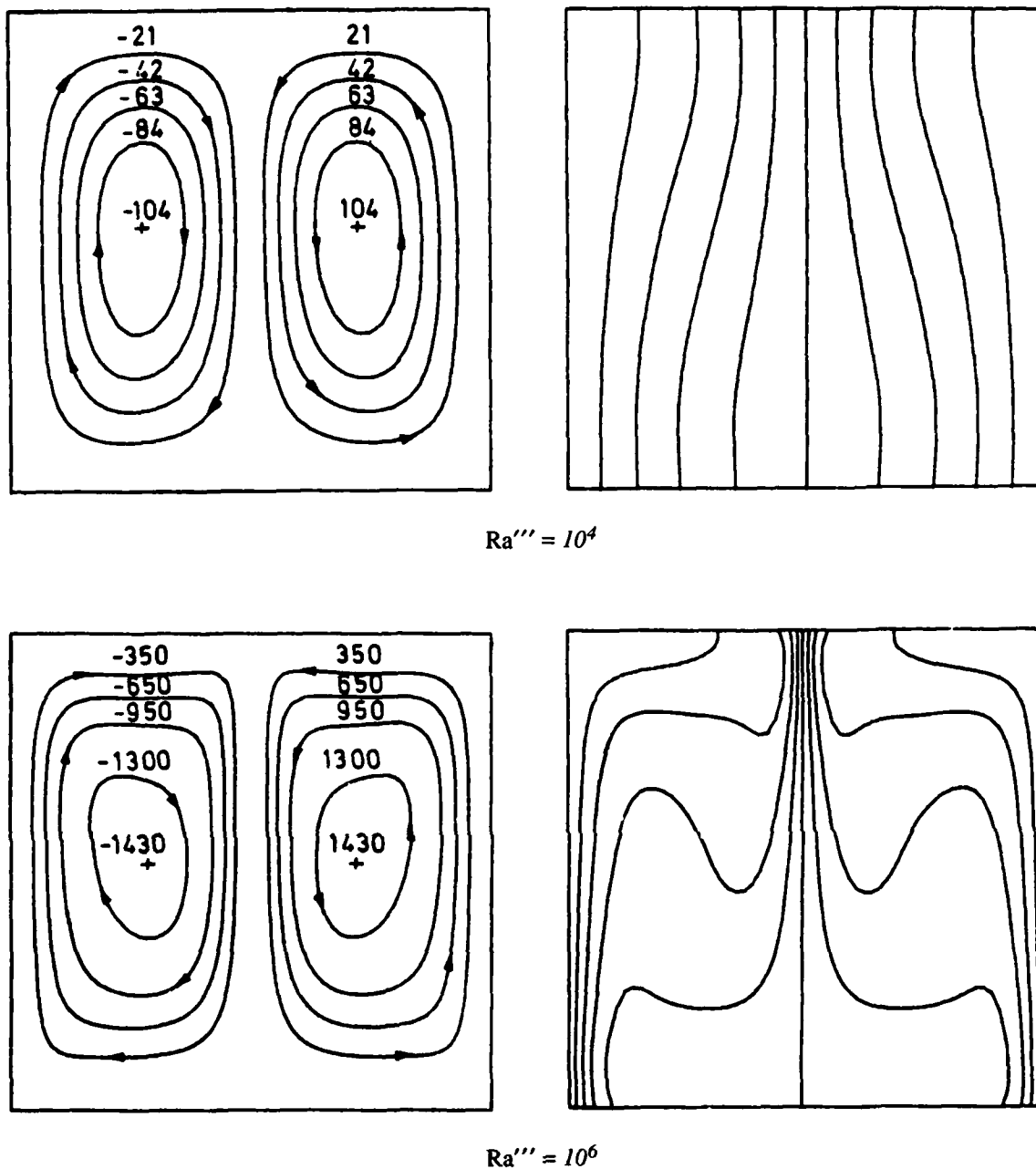


Figure 50. Dimensionless stream function ($\psi \times 10^3$) and temperature [$\theta = 0(0.1)1$] contours for $Ra''' = 10^4$ and 10^6 and $R' = 1/2$ (Lin and Nansteel 1987a).

The average Nusselt number over a vertical cross section is

$$Nu(X) = \int_0^1 Nu(X, Y) dY. \quad (75)$$

Figure 52 shows the variation of Nu with R' for Ra''' at 10^3 , 10^4 , 10^5 and 10^6 . The most striking feature of this figure is the minimum in heat transfer at $R' = 1/2$, which is caused by the symmetric, dual-cell flow structure that results when T_h and T_c straddle the maximum density temperature. The dual-cell structure prevents direct convective transfer between the hot and cold walls. Each cell acts like an

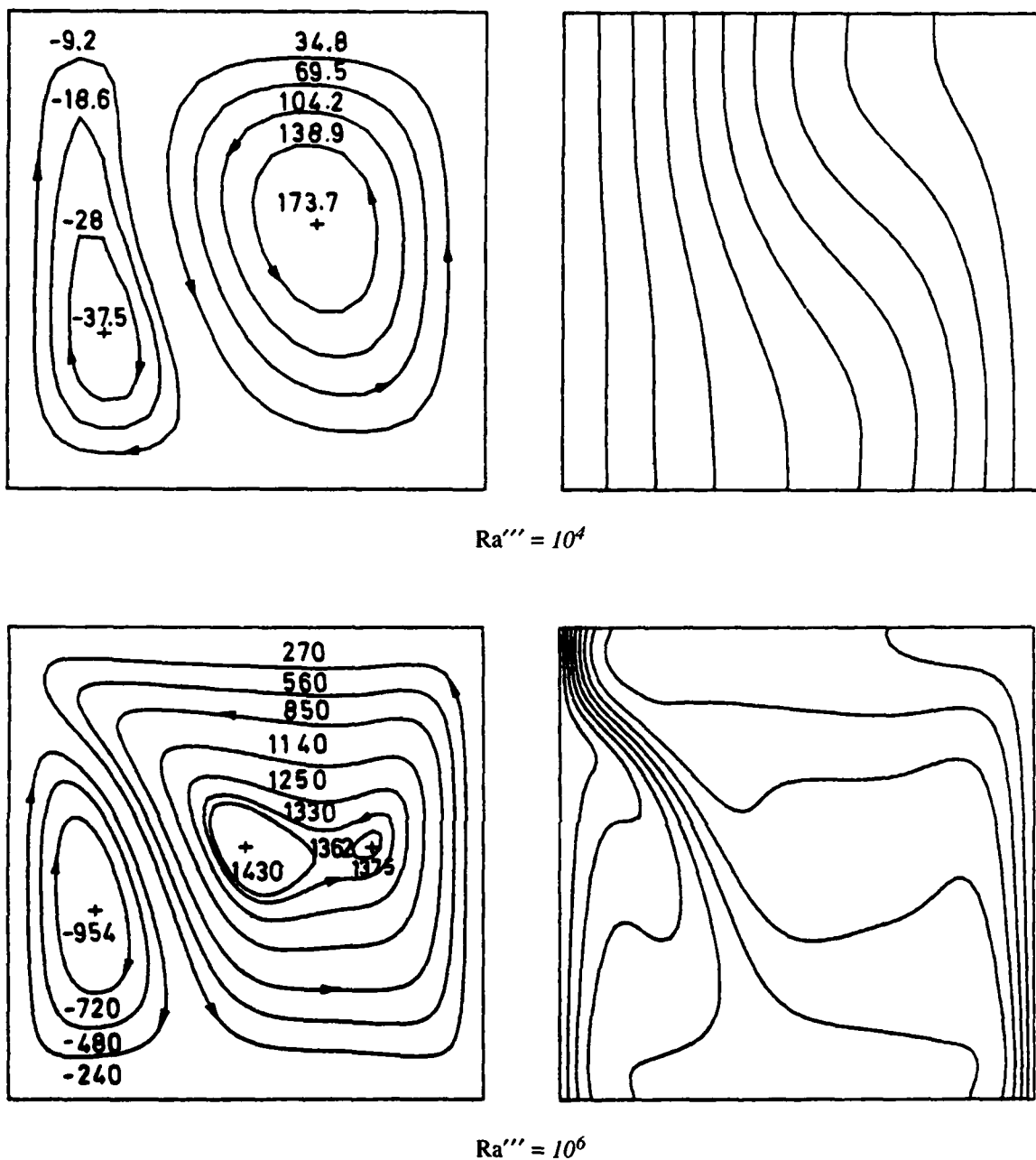


Figure 51. Dimensionless stream function ($\psi \times 10^3$) and temperature [$\theta = 0(0.1)1$] contours for $Ra''' = 10^4$ and 10^6 and $R' = 0.55$ (Lin and Nansteel 1987a).

insulator, preventing warm (or cool) fluid from the hot (or cold) wall from coming in contact with the cold (or hot) wall. The only direct thermal communication between the two walls occurs at $X = 1/2$ where the warm and cold streams meet and energy is transferred primarily by conduction. Nu increases very sharply for $1/2 < R' < 1/2$ and when Ra''' is large, because one of the two cells in the enclosure wets both walls (see Fig. 51).

Figure 53 shows the variation of Nu with Ra''' with R' as a parameter. It can be observed that as Ra''' becomes larger, the heat transfer behavior is similar to that observed for a Boussinesq fluid, that is

$$Nu \propto (Ra''')^{0.29}$$

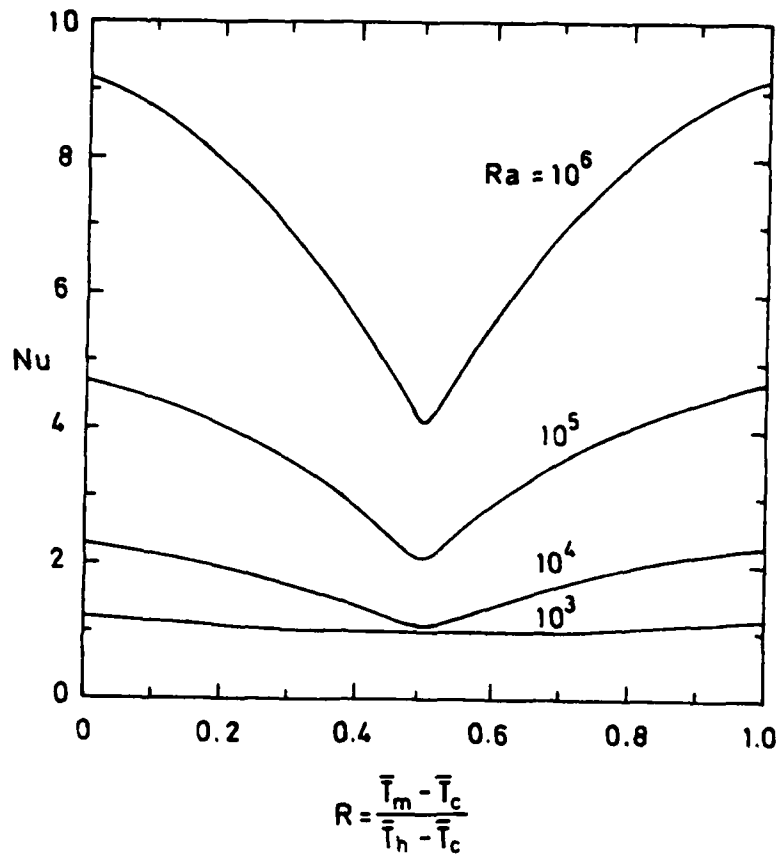


Figure 52. Variation of Nu with R' using Ra''' as a parameter (Lin and Nansteel 1987a).

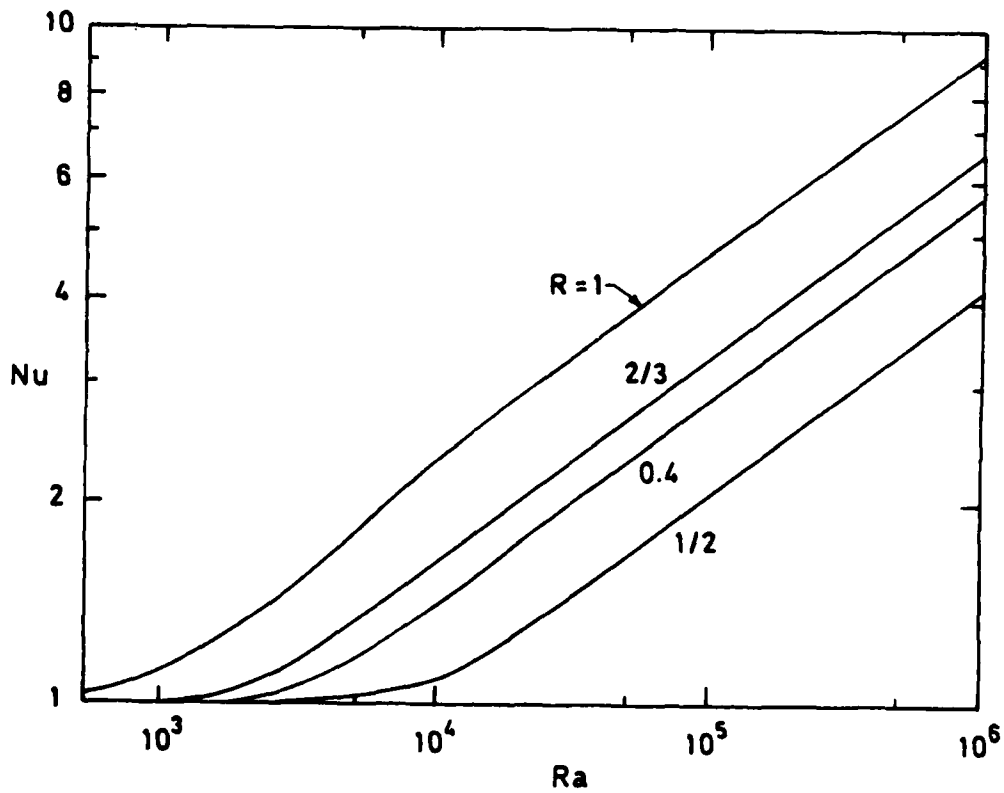


Figure 53. Variation of Nu with Ra''' using R' as a parameter (Lin and Nansteel 1987a).

independent of R' . The behavior for large Ra''' is seen to blend smoothly into the conduction-dominated regime, $Nu \sim 1$, for smaller Ra''' .

In a rectangular enclosure

Desai and Forbes (1971) reported the first numerical investigation on free convection of water (in the vicinity of maximum density) in a rectangular enclosure. The vertical walls were maintained at different temperatures and the horizontal walls insulated. Two sets of cold and hot wall temperature combinations (i.e., $T_o = 2^\circ\text{C}$, $T_h = 6^\circ\text{C}$ and $T_c = 0^\circ\text{C}$ and $T_h = 8^\circ\text{C}$) were used for each aspect ratio of 1 or 3. Desai and Forbes (1971) used two representations of density-temperature relations:

$$\rho_s = \left[0.999841 + 0.000132 \sin \left(\frac{\pi T}{8} \right) \right]$$

and

$$\rho_p = 0.99984247 + 6.460 \times 10^{-5} T - 8.0 \times 10^{-6} T^2.$$

Their finite difference approximation solution leads to the heat transfer across the enclosure as

$$Nu = \left(-\frac{1}{2} \frac{\partial \theta}{\partial X} \right) \Big|_{X=0}$$

in which

$$X = \frac{x}{W}$$

(where W is the width of the enclosure), and θ is the dimensionless temperature defined as

$$\theta = \frac{T - \bar{T}}{T_h - \bar{T}} \text{ when } \bar{T} = (T_h + T_c)/2.$$

Table 2 gives the steady-state mean Nusselt numbers as a function of aspect ratio A (defined as height/width), T_c , T_h and the density temperature representation. Clearly, the Nu values are higher for the 0° and 8°C combination regardless of the function of density it is based on.

Nansteel et al. (1987) theoretically extended the work of Lin and Nansteel (1987a) to the case of rectangular enclosure at low Rayleigh numbers. The schematic representation of the problem is the same as shown in Figure 48 except for an additional variable, the aspect ratio A .

Table 2. Steady-state mean Nusselt numbers (Desai and Forbes 1971).

$A (= H/W)$	$T_c (^\circ\text{C})$	$T_h (^\circ\text{C})$	Nu (based on ρ_s^*)	Nu (based on ρ_p^*)
1	2	6	1.5164	1.3096
1	0	8	2.7738	2.5989
3	2	6	1.1314	1.0179
3	0	8	2.1439	1.9733

* Density based on sine and polynomial function, respectively.

With the assumption of steady, laminar and two-dimensional flow and constant physical properties (except for the density in the buoyancy force term) evaluated at the extremum temperature and with the density-temperature relation represented by eq 2, i.e.,

$$\rho = \rho_m [1 - \gamma (T - T_m)^2]$$

the dimensionless equations of motion and energy transfer are

$$\frac{\partial \psi}{\partial Y} \left(\frac{\partial}{\partial X} (\nabla^2 \psi) \right) - \frac{\partial \psi}{\partial X} \left(\frac{\partial}{\partial Y} (\nabla^2 \psi) \right) = Pr \left(\nabla^4 \psi - 2 Ra (\theta - R') \frac{\partial \theta}{\partial X} \right) \quad (76)$$

and

$$\frac{\partial \psi}{\partial Y} \frac{\partial \theta}{\partial X} - \frac{\partial \psi}{\partial X} \frac{\partial \theta}{\partial Y} = \nabla^2 \theta \quad (77)$$

in which the Rayleigh number Ra and the density distribution parameter are given as

$$Ra = g \gamma L^3 (T_h - T_c)^2 / \nu \alpha$$

and

$$R = (T_m - T_c) / (T_h - T_c).$$

The solutions of eq 76 and 77 are assumed to be expanded in powers of Ra and θ , i.e.,

$$\psi = \psi_1 Ra + \psi_2 Ra^2 + \dots \quad (78)$$

$$\theta = \theta_0 + \theta_1 Ra + \theta_2 Ra^2 + \dots \quad (79)$$

The average heat flux at the hot wall is

$$q = \frac{k}{H} \int_0^H \frac{\partial T}{\partial x}(0, y) dy.$$

If expressed in terms of Nusselt numbers, this becomes

$$Nu = \frac{qL}{k(T_h - T_c)} = -\frac{1}{A} \int_0^A \frac{\partial \theta}{\partial X}(0, Y) dY. \quad (80)$$

Substituting eq 79 into eq 80 yields

$$Nu = Nu_0 + Nu_1 Ra + Nu_2 Ra^2 + \dots \quad (81)$$

where

$$Nu_1 = -\frac{1}{A} \int_0^A \frac{\partial \theta_1}{\partial X} (0, Y) dY.$$

The leading term $Nu_0 = 1$ is the contribution to the heat transfer from the conduction temperature field $\theta_0 = 1 - X$. The first correction $Nu_1 = 0$ is necessary because of the antisymmetry of θ_1 with respect to $Y = A/2$. Therefore the first non-zero correction to heat transfer is

$$Nu_2 = -\frac{1}{A} \int_0^A \frac{\partial \theta_2}{\partial X} (0, Y) dY$$

which can be determined in terms of θ_1 and ψ_1 by

$$Nu_2 = \frac{1}{A} \int_0^1 \int_0^A \theta_1 \frac{\partial \psi_1}{\partial Y} dY dX. \quad (82)$$

Flow patterns

Figure 54 shows the variation of ψ_1 with $R' = 1/2$, for $A = 1/2$, and 2. The strength of the counterrotating flow appears to decrease with decreasing A . Circulation strength is effectively quenched with decreasing A because of the choking effect of the horizontal boundaries as they approach one another. Figure 55 shows the variation of ψ_1 with $R' = 0.65$ (a slight increase from Fig. 54) and $A = 1/2$ and 2. It indicates a transition from a two-cell to three-cell structure with increasing A . This is because the large counterclockwise cell on the right is close to the hot wall and able to drag the warm and lighter fluid downward, overcoming the upward buoyancy force.

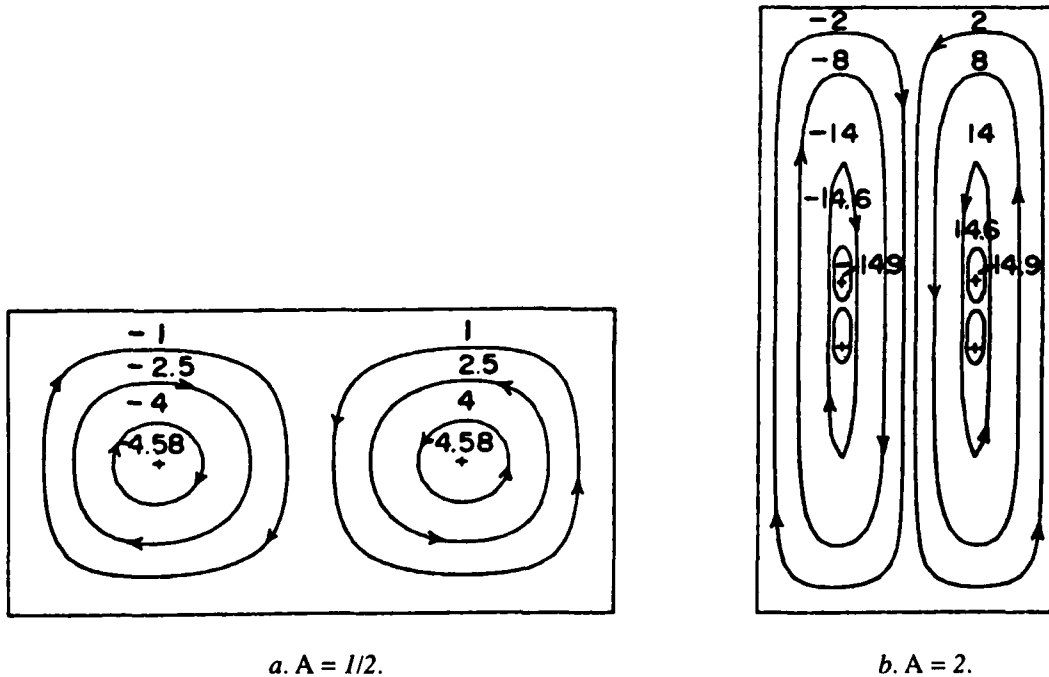


Figure 54. Variation of dimensionless streamfunction ($\psi_1 \times 10^5$) for $R' = 1/2$ (Nansteel et al. 1987).

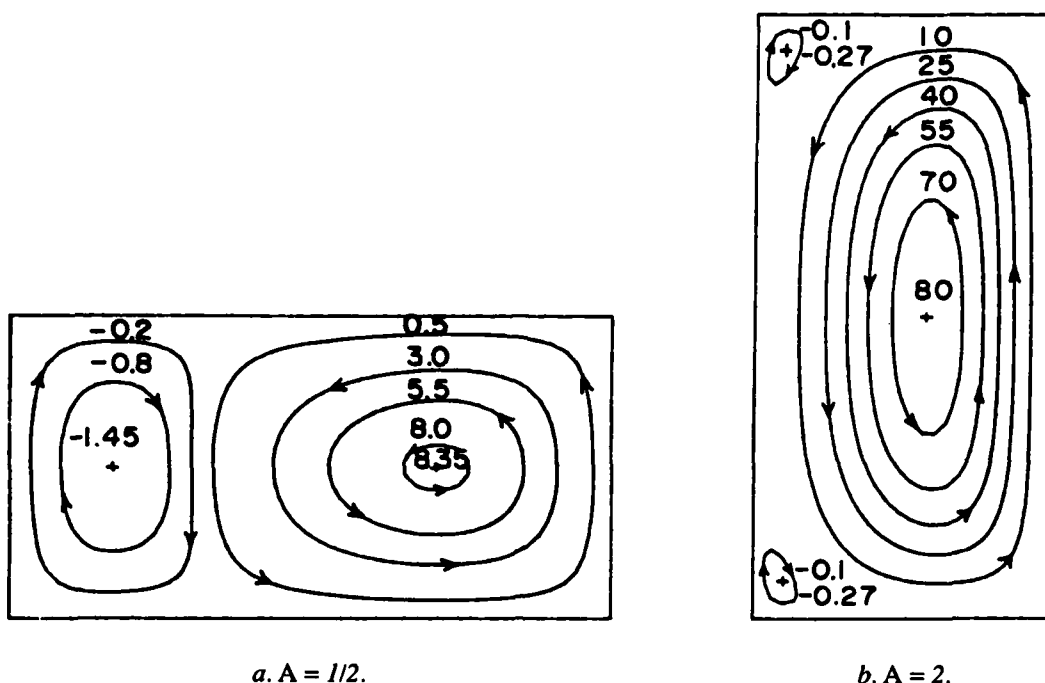


Figure 55. Variation of dimensionless streamfunction ($\psi_1 \times 10^5$) for $R' = 0.65$ (Nansteel et al. 1987).

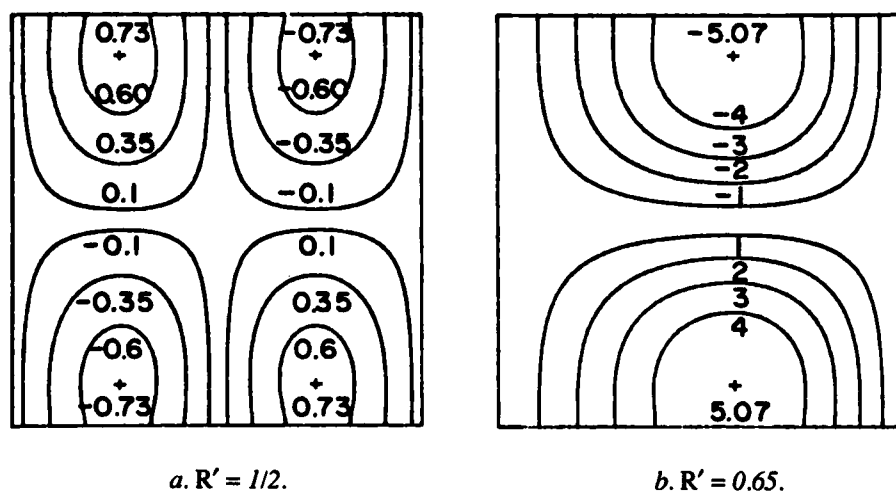


Figure 56. Dimensionless first correction θ_1 as function of R' with $A = 1$ (Nansteel et al. 1987).

Heat transfer

Figure 56 shows the first correction θ_1 to the conduction temperature field $\theta = 1 - X$ for a square enclosure. Figure 56a, for $R' = 1/2$, clearly shows that θ_1 is antisymmetric with respect to the enclosure midplanes $X = 1/2$ and $Y = A/2$. As a consequence, θ_1 is a positive (or negative) perturbation on θ_0 in the upper left-hand (or right-hand) and lower right-hand (or left-hand) quadrants of the enclosure. Hence, isotherms (θ) will be slightly compressed toward the vertical midplane, $X = 1/2$, in the upper half of the enclosure and displaced outward from the midplane in the lower half. Figure 56b shows θ_1 contours for the case of $R' = 0.65$. It indicates that θ_1 results in a negative perturbation

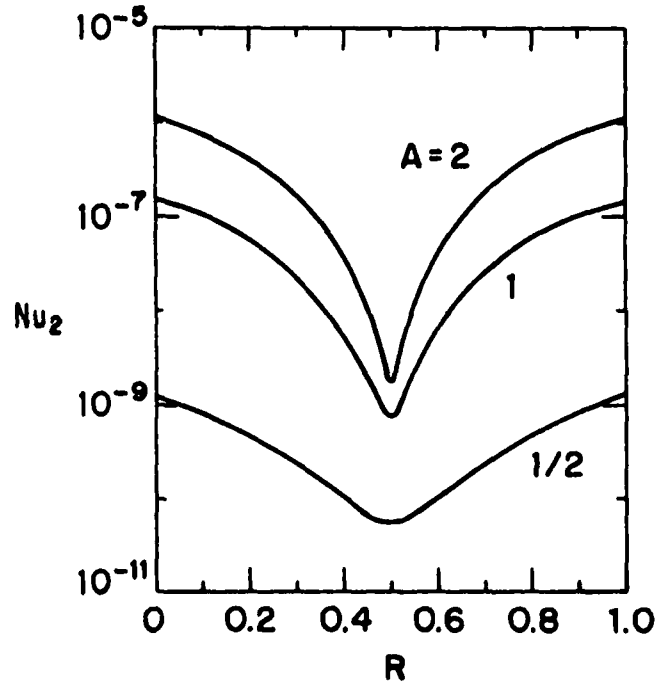


Figure 57. First correction to heat transfer, Nu_2 as function of R' (Nansteel et al. 1987).

to the temperature field in the upper half of the enclosure and a positive perturbation in the lower half. This results in isotherms being displaced slightly toward the hot wall in the enclosure's upper half and toward the cold wall in the lower half. Figure 57 shows the variation of the first correction to the heat transfer Nu_2 with R' for $A = 1/2, 1$, and 2 . Nu_2 reaches a minimum at $R' = 1/2$. It should be noted that the perturbation, Nu_2 , to the pure conduction heat transfer rate increases rapidly and symmetrically with respect to $R' = 1/2$. The magnitude of Nu_2 as well as the sharpness of the minimum at $R' = 1/2$ is clearly seen to be an increasing function of A . For fixed $R' \geq 1/2$ with increasing A , there may be radical change in the basic structure of the flow. As indicated in Figures 54a and 55b, the flow changes from a dual-cell to tri-cell structure in which the large counterclockwise right-hand cell wets both the hot and cold walls. This direct contact of cells with both vertical boundaries greatly enhances the convective contribution to the cross-cavity energy transfer.

In a horizontal layer

Forbes and Cooper (1975) presented the first analytical study on natural convection, caused by cooling from above, of a horizontal water layer initially at temperatures of either 4°C or 8°C . The water was confined laterally and underneath by rigid insulators and the upper horizontal surface was subjected to 1) a constant 0°C temperature and a rigid conducting boundary, and 2) a free water-to-air convection boundary condition, in which the convective heat transfer was held constant at values of 5.68 or $284 \text{ W/m}^2\text{K}$ while the temperature of the ambient air is kept at 0°C . In their study, the ratios of width to depth (W/D) were $1, 3$ and 6 (W/D is the reciprocal of aspect ratio A).

If the flow is considered to be laminar and two-dimensional (this restricts the dimension of D to the order of 1 cm), and density variations are considered only in the buoyancy term, the governing dimensionless equations of motion and energy can be written as

Vorticity

$$\frac{\partial \Omega}{\partial \tau} + \frac{U}{Pr} \frac{\partial \Omega}{\partial X} + \frac{V}{Pr} \frac{\partial \Omega}{\partial Y} = \frac{\partial}{\partial X} (Ra^*) + \nabla^2 \Omega \quad (83)$$

and

Energy

$$Pr \frac{\partial \theta}{\partial \tau} + U \frac{\partial \theta}{\partial X} + V \frac{\partial \theta}{\partial Y} = \nabla^2 \theta \quad (84)$$

Stream function

$$\Omega = -\nabla^2 \psi \quad (85)$$

Velocities

$$U = \frac{\partial \psi}{\partial Y}, \quad V = -\frac{\partial \psi}{\partial X} \quad (86)$$

The above equations have been made dimensionless through the use of the following dimensionless variables:

$$\begin{aligned} X &= \frac{x}{D}, \quad Y = \frac{y}{D} \\ U &= \frac{uD}{\alpha}, \quad V = \frac{vD}{\alpha}, \quad \tau = \frac{\nu t}{D^2} \\ \psi &= \frac{\bar{\psi}}{\alpha}, \quad \Omega = \frac{\bar{\Omega} D^2}{\alpha} \end{aligned} \quad (87)$$

The initial and boundary conditions may be written as

$$\psi(X, Y, 0) = 0, \quad \theta(X, Y, 0) = 1$$

$$U(X, Y, 0) = V(X, Y, 0) = 0$$

$$U = V = 0 \text{ on all boundaries}$$

and

$$\frac{\partial \theta}{\partial X}(0, Y, \tau) = \frac{\partial \theta}{\partial Y}\left(\frac{w}{D}, Y, \tau\right) = \frac{\partial \theta}{\partial Y}(X, 0, \tau) = 0.$$

At the free surface ($Y = 1$) the boundary condition is either:

$$\theta'''(X, 1, \tau) = 0 \quad \text{where} \quad \theta''' = \frac{T - T_s}{T_o - T_s} \quad (88)$$

for fixed surface temperature or

$$h(T_{y=D} - T_a) = -k \left(\frac{\partial T}{\partial y} \right)_{y=D} \quad (89)$$

If θ''' is defined as

$$\theta''' = \frac{T - T_a}{T_o - T_a},$$

eq 89 becomes

$$\frac{hD}{R} = Nu = - \left(\frac{1}{\theta'''} \frac{\partial \theta'''}{\partial Y} \right)_{Y=1}. \quad (90)$$

Here

$$Ra^* = Pr \frac{\bar{\rho} [\bar{\rho} - \rho(\theta''')] g D^3}{\mu^2}$$

where $\bar{\rho}$ is the density at $(T_s + T_o)/2$ in which T_o and T_s are the initial water and water surface temperature, respectively. The temperature-density relation is expressed by

$$\rho(T) = 0.99984247 + 6.46 \times 10^{-5} T - 8.0 \times 10^{-6} T^2.$$

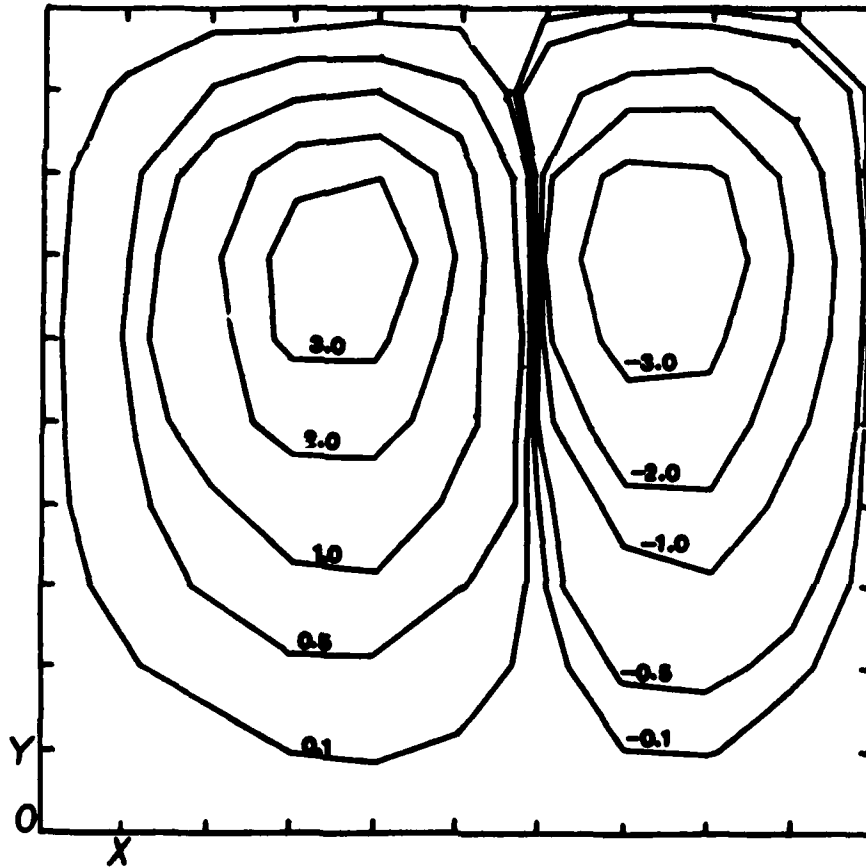
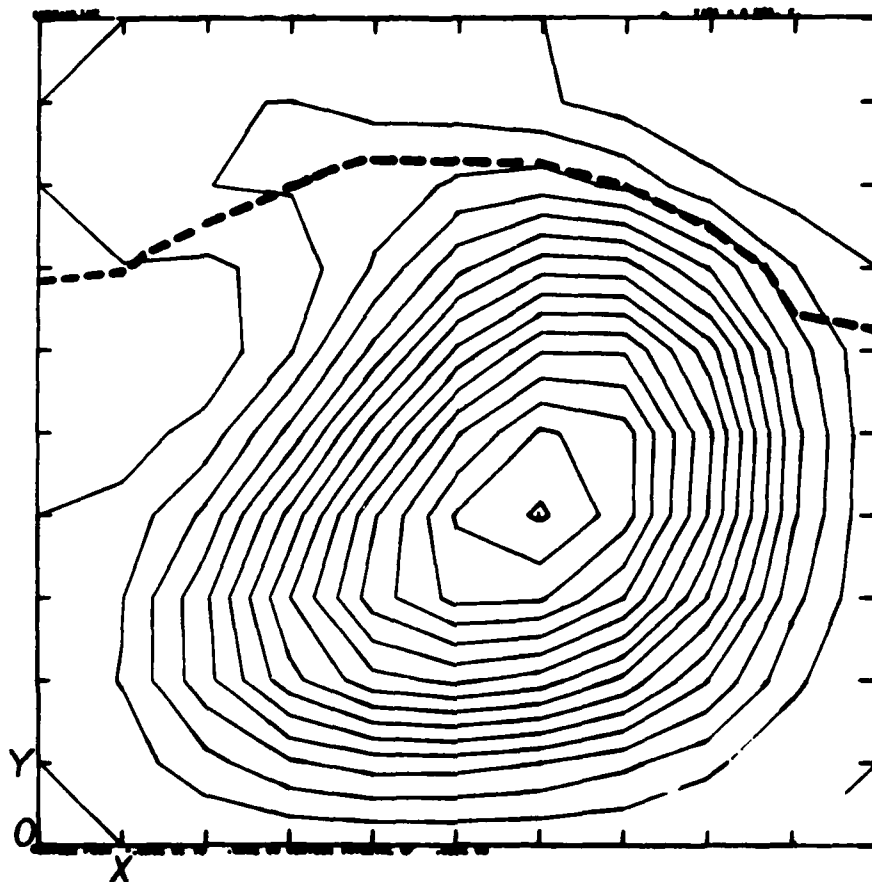


Figure 58. Transient dimensionless stream lines: $W/D = 1.0$, $T_o = 8^\circ\text{C}$, $t = 0.55 \text{ s}$ ($\tau = 0.002$), $T_s = 0^\circ\text{C}$ (Forbes and Cooper 1975).



a. Transient streamlines.

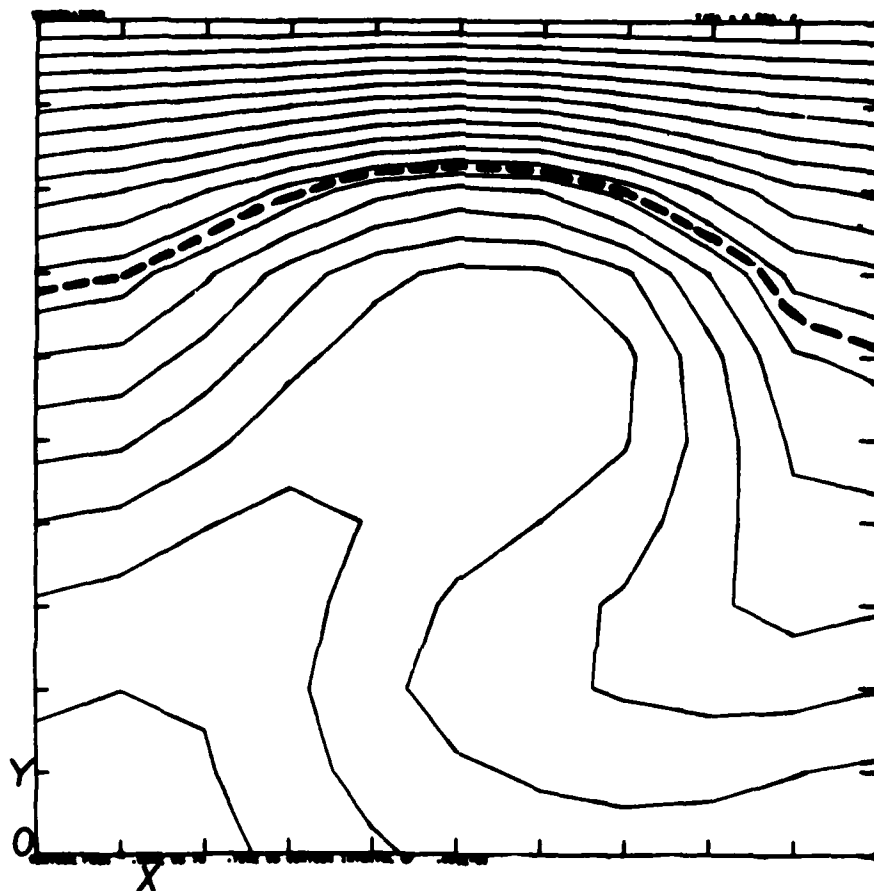
Figure 59. Transient dimensionless streamlines and isotherms: $W/D = 1.0$, $T_o = 8^\circ\text{C}$, $t = 250\text{ s}$ ($\tau = 1.0$), and $T_s = 0^\circ\text{C}$ (Forbes and Cooper 1975).

Streamlines and isotherms

The implicit alternating direction method was used to solve the governing equations, and the results are expressed in transient streamlines and isotherms. Figures 58–61 show a series of transient streamlines and the corresponding isotherms for $W/D = 1.0$, $T_o = 8^\circ\text{C}$, and a constant surface temperature of $T_s = 0^\circ\text{C}$, with time values of 0.5 s ($\tau = 0.002$), 250 s , and 62.5 min . The streamlines shown in Figure 58 are identical to the flow configurations observed in both experimental and theoretical investigations of natural convection in horizontal layers of fluid heated from below. In this figure, the 4°C isotherm lies very near the water surface, and the entire cavity region is hydrodynamically unstable. The water current ascends in the central region between the two eddies, and descends adjacent to the two lateral sides of the cavity.

At $\tau = 0.1$ or 250 s , (Fig. 59a and b), the eddy that appeared on the left side of the flow field at $\tau = 0.002$ has momentarily disintegrated. The heavy dotted line shows the 4°C isotherm; this region of maximum density provides the driving force for the eddy motion. As the region of the maximum density descends further, the 4°C isotherm separates the two eddies as shown in Figure 60a. The eddy entirely beneath the 4°C isotherm is therefore the result of unstable density gradients.

This circulation flow exerts a viscous shearing stress upon the stable water above the region of maximum density, and this shearing stress provides the energy necessary for eddy formation in the region of hydrodynamic stability. The straight parallel isotherms that appear in the upper portion of



b. Transient isotherms.

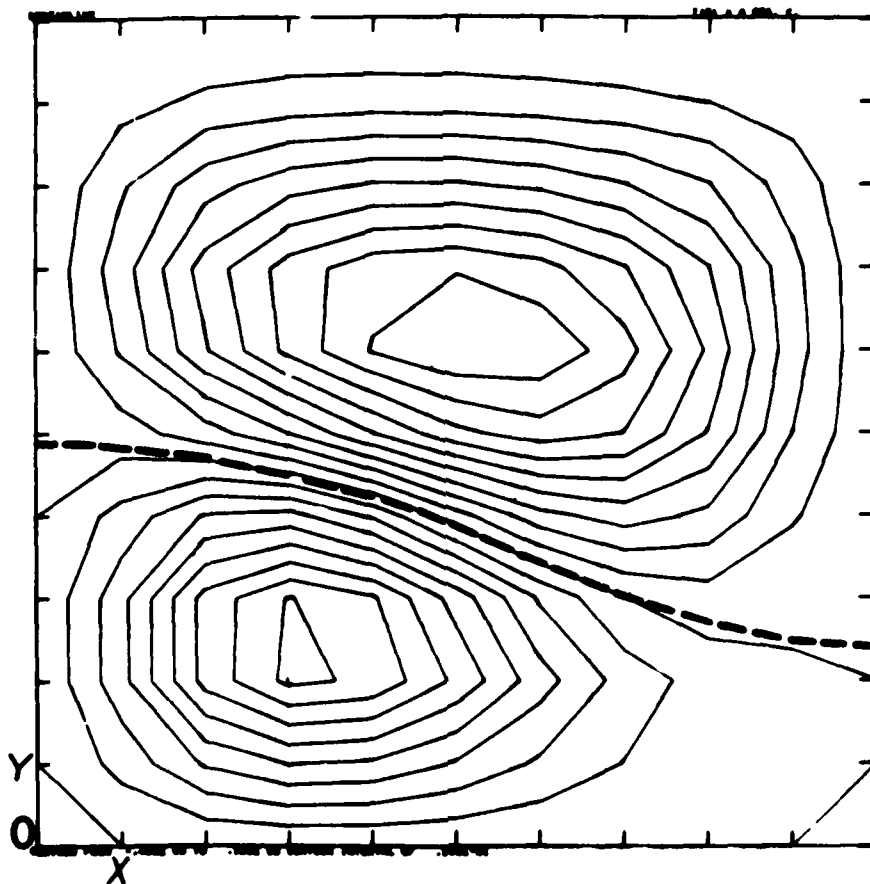
Figure 59 (cont'd).

Table 3a. Maximum and minimum values of stream functions, with a constant temperature boundary (Desai and Forbes 1971).

<i>Figure</i>	<i>W/D</i>	<i>T_o</i>	ψ_{max}	ψ_{min}	$\Delta\psi$
58	1	8	3.0	-3.0	1.0
59(a)	1	8	0.0	-6.0	0.40
60(a)	1	8	0.5	-0.4	0.05
61(a)	1	8	0.00128	0.0	0.00008

Table 3b. Maximum and minimum dimensionless temperatures, with a constant temperature boundary (Desai and Forbes 1971).

<i>Figure</i>	<i>W/D</i>	<i>T_h</i>	θ_{max}'''	θ_{min}'''	$\Delta\theta'''$
59(b)	1	8	0.72	0.0	0.04
60(b)	1	8	0.60	0.0	0.03
61(b)	1	8	0.034	0.0	0.002



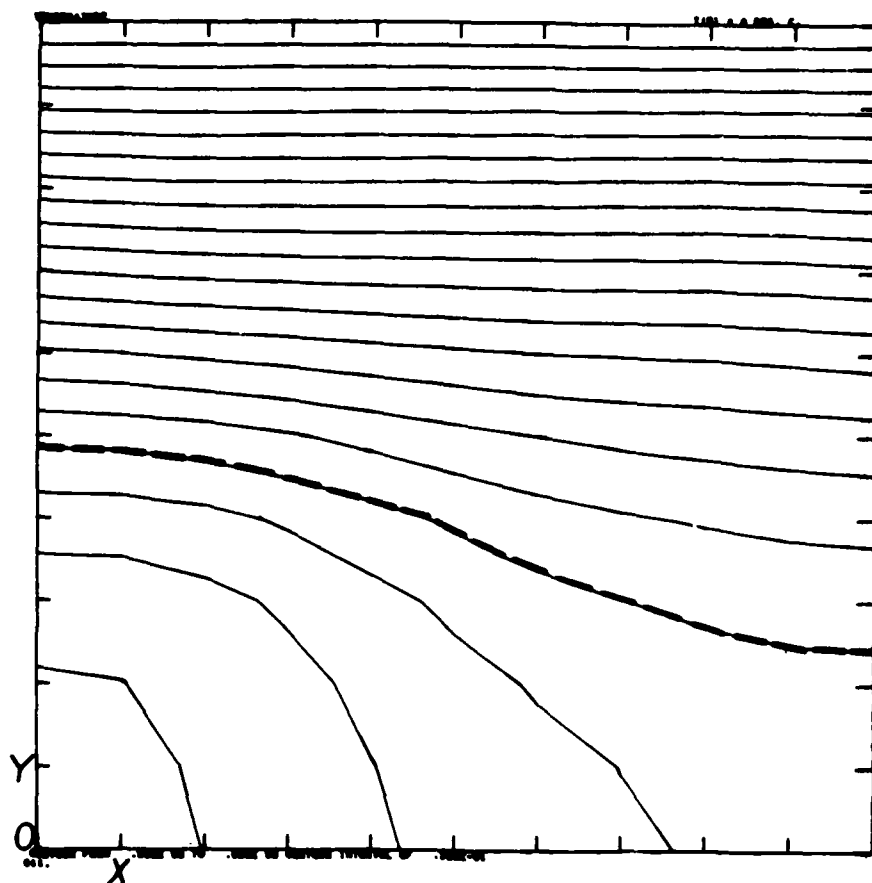
a. Transient streamlines.

Figure 60. Transient dimensionless streamlines and isotherms: $W/D = 1.0$, $T_o = 8^\circ\text{C}$, $t = 500 \text{ s}$ ($\tau = 2.0$) and $T_s = 0^\circ\text{C}$ (Forbes and Cooper 1975).

Figure 60b indicates that the heat transfer in the stable region is largely by conduction. The eddy in the unstable region continues to distort the temperature distribution and, therefore, heat is transferred in this region primarily by convection. Figures 61a and b depict the flow pattern and the temperature distribution, respectively, at $\tau = 5.0$ (or 62.5 min). The 4°C region has now passed out of the domain of the system and, therefore, the fluid body is entirely stable. The large eddy appearing in Figure 61a is the same eddy that previously appeared above the region of maximum density (Fig. 60a). The momentum of this eddy, at this time, has not yet been dissipated by the opposing viscous forces. Consideration of the magnitudes of the stream function (see Table 3a, 3b) reveals that the fluid velocities are much smaller than those depicted in Figure 60a. Indeed, the fluid motion is so minute that the temperature field appears undisturbed (Fig. 61b) and the water seems to have stratified. Heat transfer, therefore, at these times is purely conductive.

In the case of $T_o = 4^\circ\text{C}$, the imposition of 0°C upper surface boundary temperature cannot lead to eddy formation, as the density gradient in this case is always stable. The fluid motion is not sufficient to cause distortion of the temperature field and the heat transfer is purely conductive.

For the case of $T_o = 8^\circ\text{C}$, numerical results obtained for the $W/D = 3$ and 6 enclosures were essentially identical to those for $W/D = 1$, differing only in the number of eddies produced by the motion. Three and seven pairs of coupled eddies were produced in $W/D = 3$ and 6, respectively, and the 4°C isotherm descended through the layer. In all cases studied, the motion was "damped out" as the 4°C isotherm reached the bottom, with a stable water layer resulting for the entire cavity.



b. Transient isotherms.

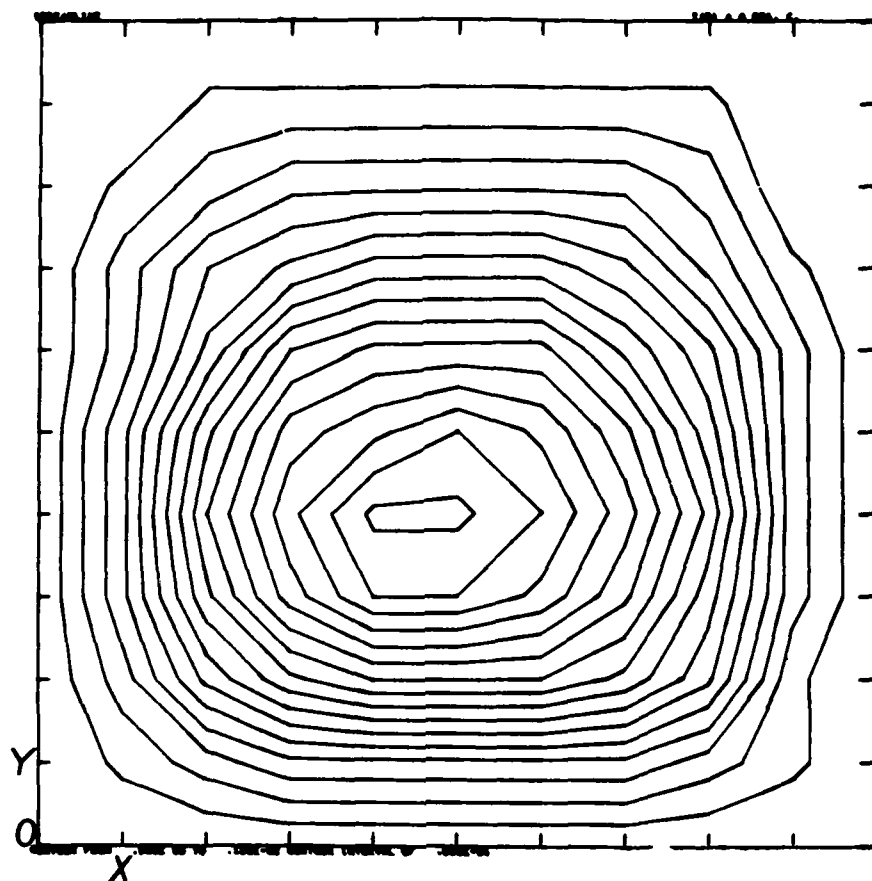
Figure 60 (cont'd).

Convective boundary

For the case of $h = 5.68 \text{ W/m}^2\text{K}$, Forbes and Cooper (1975) reported that it took much longer to set up the region of maximum density. The following results will summarize the work on $h = 284 \text{ W/m}^2\text{K}$. As indicated eq 90, i.e.,

$$\left. \frac{\partial \theta'''}{\partial Y} \right|_{Y=1} = - \left[\frac{hD}{K} \right] (\theta''')_{Y=1}.$$

The value of $(\theta''')_{Y=1} = 1.0$ for both values of h . Since D and k are constants, a 50-fold increase in the magnitude in h will produce 50-fold increase in the magnitude of the initial temperature gradient at the water surface. Figures 62a and b, 63a and b, 64a and b show the streamline and isotherms for $W/D = 3$, $T_0 = 8^\circ\text{C}$, $h = 284 \text{ W/m}^2\text{K}$ for a real time of 3, 4 and 5 minutes, respectively. Figures 65a and b show the case of $W/D = 6.0$, $T_0 = 8^\circ\text{C}$, $h = 284 \text{ W/m}^2\text{K}$ with $t = 4 \text{ min}$. Tables 4a and b show the maximum and minimum values of stream functions and dimensionless temperature, respectively. Figures 62a and b reveal the flow pattern and temperature distribution 3 min after the initiation. Since the region of maximum density is very near the upper surface at this time, the flow pattern shown in Figure 62a is very similar to the flow that occurs in horizontal fluid layers heated from below. At $t = 4 \text{ minutes}$ after initiation, the 4°C isotherm descends far enough through the liquid to produce two layers of eddies. The lower eddies are the result of an unstable density gradient and the upper eddies



a. Transient streamlines.

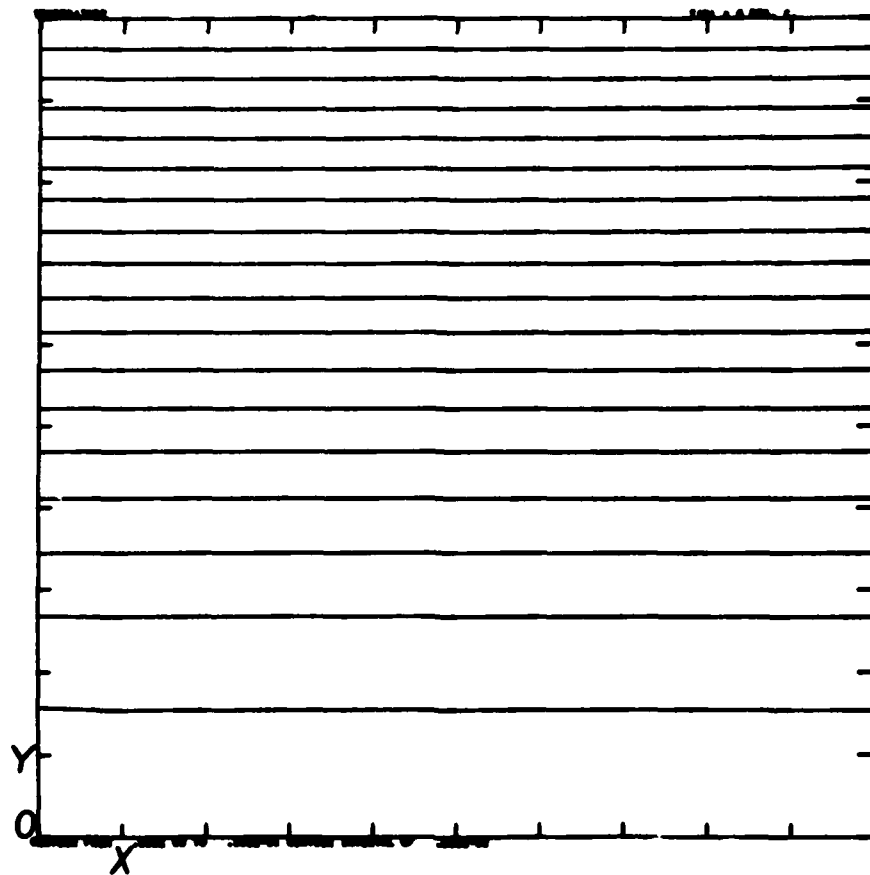
Figure 61. Transient dimensionless streamlines and isotherms: $W/D = 1.0$, $T_o = 8^\circ\text{C}$, $t = 62.5 \text{ min}$ ($\tau = 5.0$) and $T_s = 0^\circ\text{C}$ (Forbes and Cooper 1975).

Table 4a. Maximum and minimum values of stream functions, with a constant temperature boundary (Desai and Forbes 1971).

Figure	W/D	T_o	ψ_{max}	ψ_{min}	$\Delta\psi$
62(a)	3	0.006775	1.8	-2.4	0.2
63(a)	3	0.006775	0.2	-0.22	0.02
64(a)	3	0.006775	0.21	-0.10	0.01
65(a)	6	0.006775	0.22	-0.22	0.02

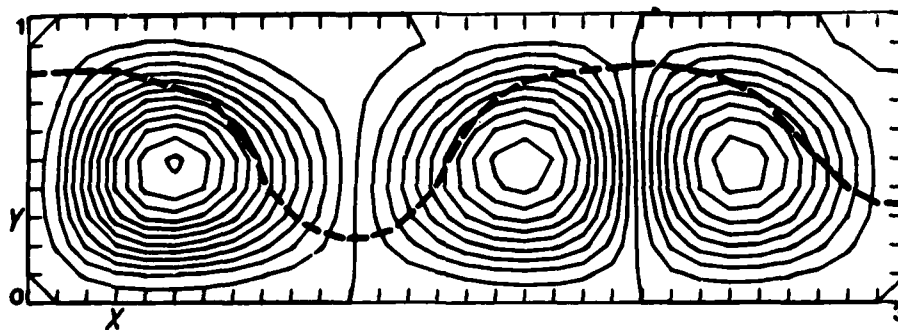
Table 4b. Maximum and minimum dimensionless temperatures, with a constant temperature boundary (Desai and Forbes 1971).

Figure	W/D	θ_{max}'''	θ_{min}'''	$\Delta\theta'''$
62(b)	3	0.78	0.18	0.03
63(b)	3	0.63	0.15	0.03
64(b)	3	0.56	0.12	0.02
65(b)	6	0.62	0.14	0.02



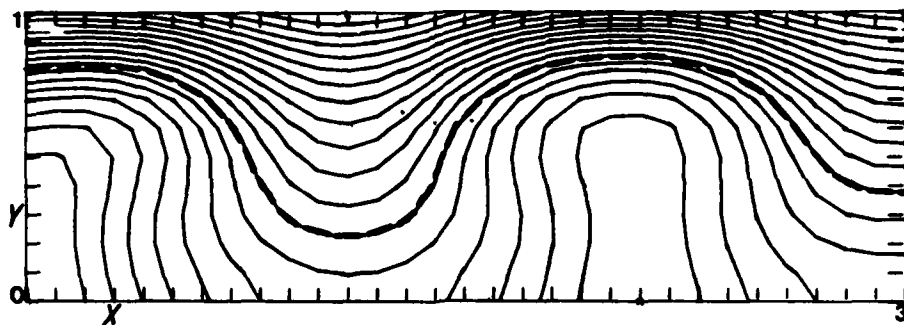
b. Transient isotherms.

Figure 61 (cont'd).



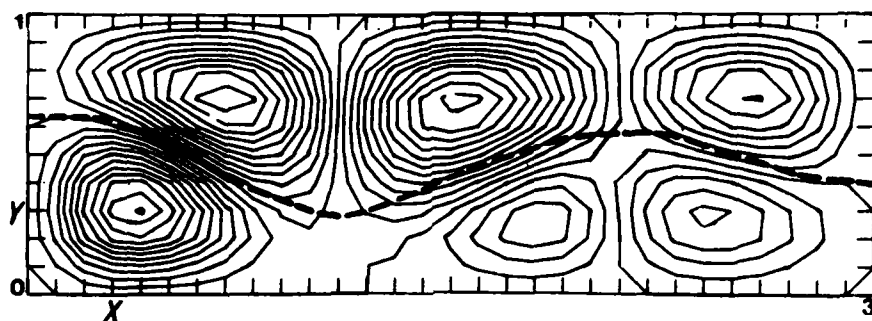
a. Transient streamlines.

Figure 62. Transient dimensionless streamlines and isotherms: $W/D = 3.0$, $T_o = 8^\circ\text{C}$, $t = \min$, and $h = 284 \text{ W/m}^2\text{k}$ (Forbes and Cooper 1975).

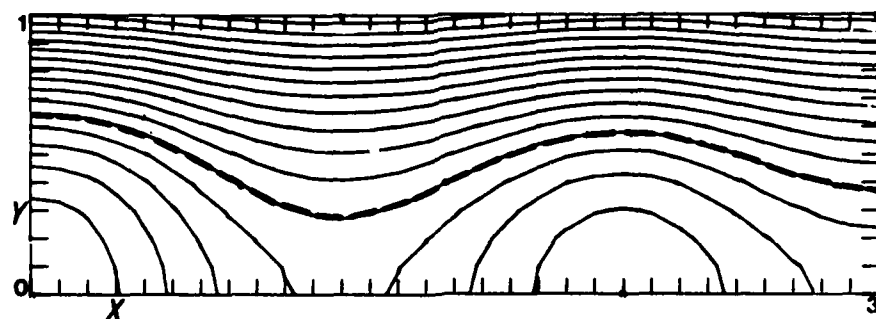


b. Transient isotherms.

Figure 62 (cont'd). Transient dimensionless streamlines and isotherms: $W/D = 3.0$, $T_o = 8^\circ\text{C}$, $t = \text{min}$, and $h = 284 \text{ W/m}^2\text{k}$ (Forbes and Cooper 1975).



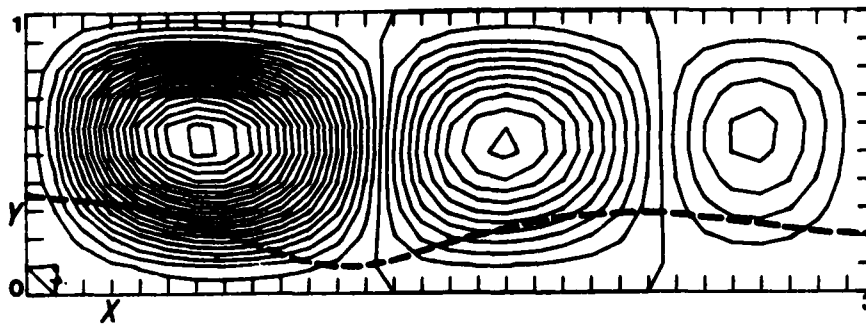
a. Transient streamlines.



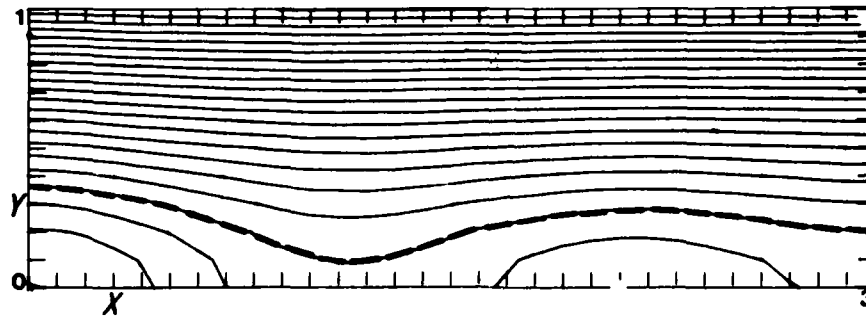
b. Transient isotherms.

Figure 63. Transient dimensionless streamlines and isotherms: $W/D = 3.0$, $T_o = 8^\circ\text{C}$, $t = 4 \text{ min}$, and $h = 284 \text{ W/m}^2\text{K}$ (Forbes and Cooper 1975).

are caused by the action of viscous shearing stress upon the water above the unstable region. Figures 64a and b provide an even clearer picture of the effect of the region of maximum density on free convection in water. The 4°C isothermal line is observed to exist near the bottom of the enclosure and the dimensionless temperature gradient ($\partial\theta'''/\partial Y$) is almost constant in the hydrodynamically stable portion of the water. Figures 65a and b show the case for $W/D = 6$. The transient formation of streamlines and dimensionless temperature distribution are very similar in nature as in the case of $W/D = 3$. However, it contains seven pairs of eddies instead. No conclusive reason is given for the asymmetrical nature of the streamline and the temperature distribution.



a. Transient streamlines.



b. Transient isotherms.

Figure 64. Transient dimensionless streamlines and isotherms: $W/D = 3.0$, $T_o = 8^\circ\text{C}$, $T = 5 \text{ min}$, and $h = 284 \text{ W/m}^2\text{K}$ (Forbes and Cooper 1975).

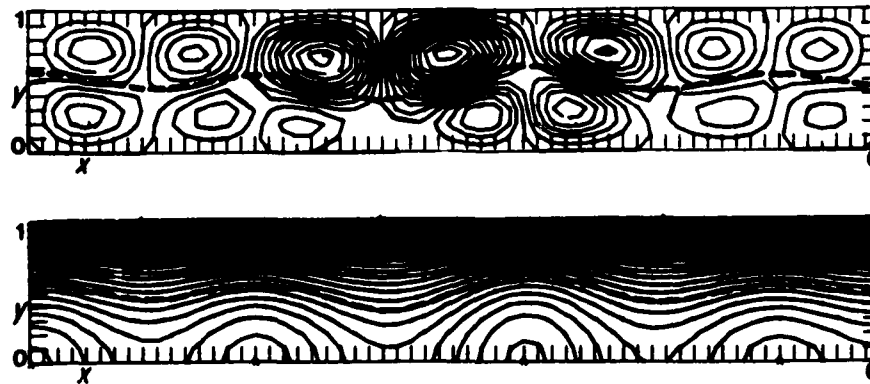


Figure 65. Transient dimensionless streamlines and isotherms: $W/D = 6.0$, $T_o = 8^\circ\text{C}$, $t = 4 \text{ min}$, and $h = 284 \text{ W/m}^2\text{K}$ (Forbes and Cooper 1975).

In a circular and confined melt layer

Yen (1968) and Yen and Galea (1969) were the first to investigate the natural convection and the temperature distribution caused by the density inversion of the continuously deepening layer (originally there is only a single phase, i.e., a solid ice melt layer forming upon the application of a constant surface temperature). In their study, both modes of melting were employed (i.e., melting from below and the top). They found that the onset of convection and the transition from a conductive to convective heat transfer mode depends on the imposed boundary temperatures, a rather strong function

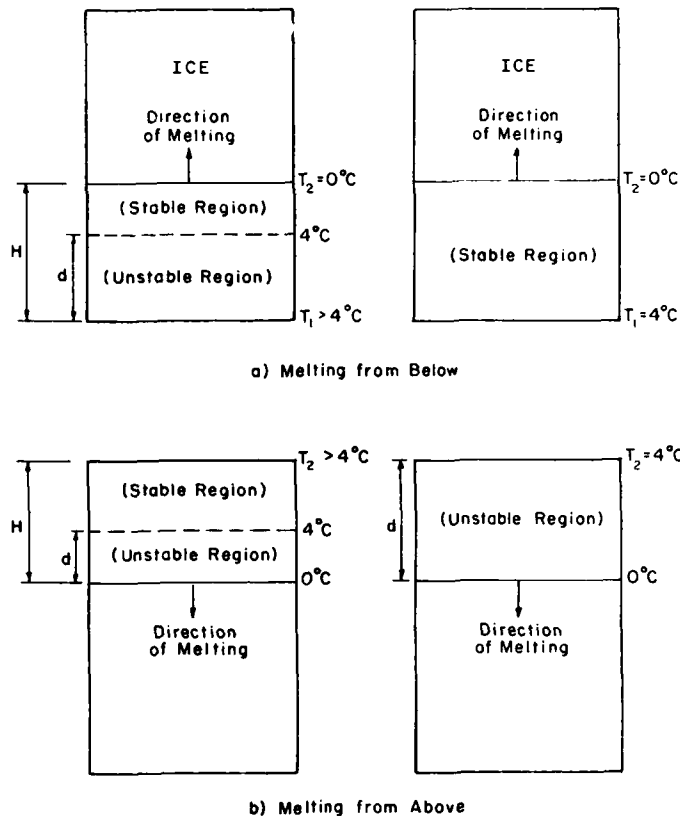
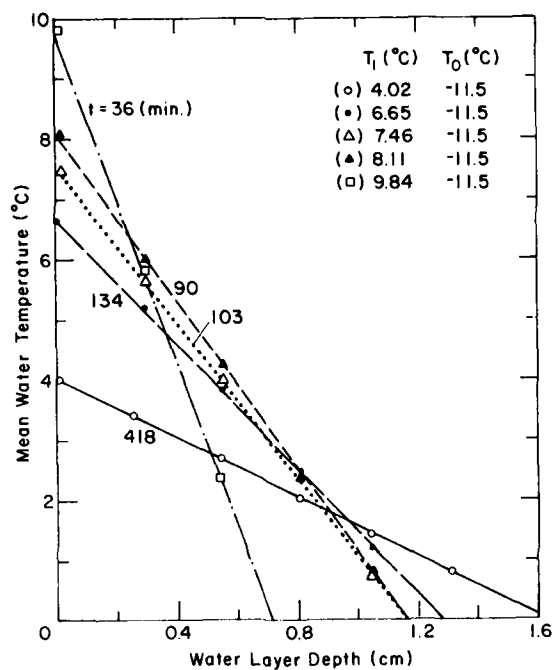


Figure 66. Schematic representation of the interdependence of stable and unstable regions with the thermal boundary conditions.

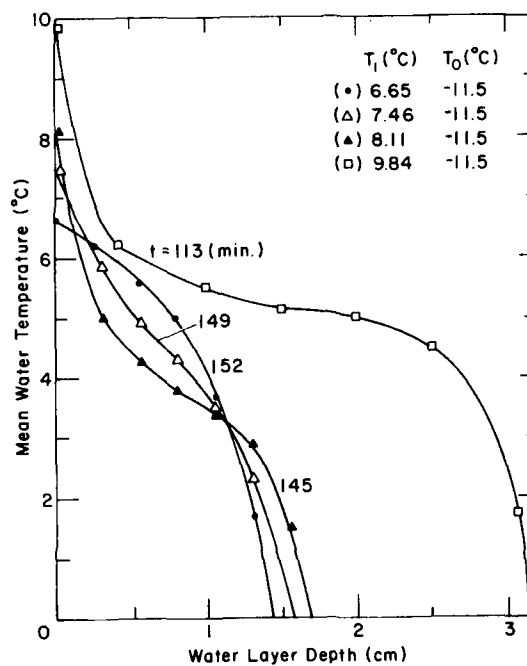
of temperature in melting from below but a considerably weaker one in the case of melting from above. Figure 66 is a schematic representation of the interdependence of stable and unstable regions with the thermal boundary conditions. Figures 67 and 68 show some typical temperature distributions in the melt layer at various times after initiation of the melting (Yen 1984). It can be seen that the time elapsed to deviate from linear distribution depends on the boundary temperature imposed. For melting from below, the higher the boundary temperature the shorter the time needed to change from conduction to convection. On the other hand, for melting from above, since the maximum density region is near the water/ice interface, the overlying stable layer becomes thicker as upper boundary temperatures increase, extending the 4°C region upward and thus reducing its effectiveness in overturning the water near the ice surface. The major difference in the temperature distribution in the pseudo-steady state is that the constant temperature zone depends on the boundary temperature in melting from below, while the temperature in the constant temperature region is ~3.2°C independent of the upper boundary temperature in melting from above (see Fig. 68c).

Yen (1980) derived heat flux expressions for the melt layer formed by melting from both below and above. In his experiments where the melting rate was determined, the total upward or downward heat flux for melting from below or above was evaluated by

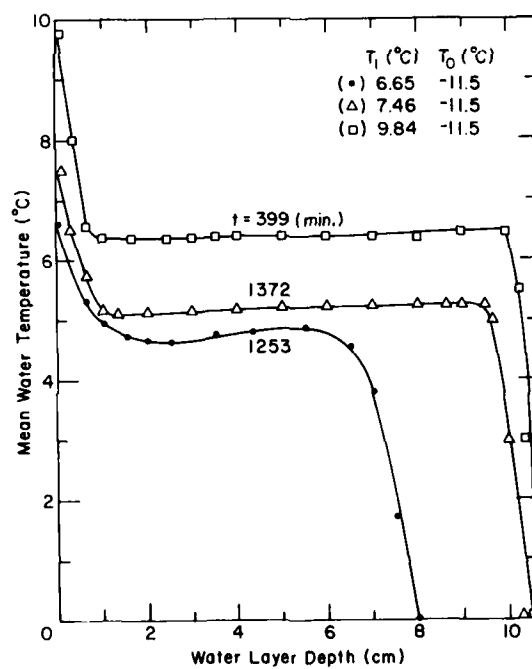
$$q = \rho \frac{dz}{dt} [L_f + C_i (T_m - T_{io})] + \frac{\rho c_p}{2t} [z(t)(T + T_m)] - K_i \left. \frac{dT_i}{dz} \right|_{z=H_c} \quad (91)$$



a. Before onset of convection.

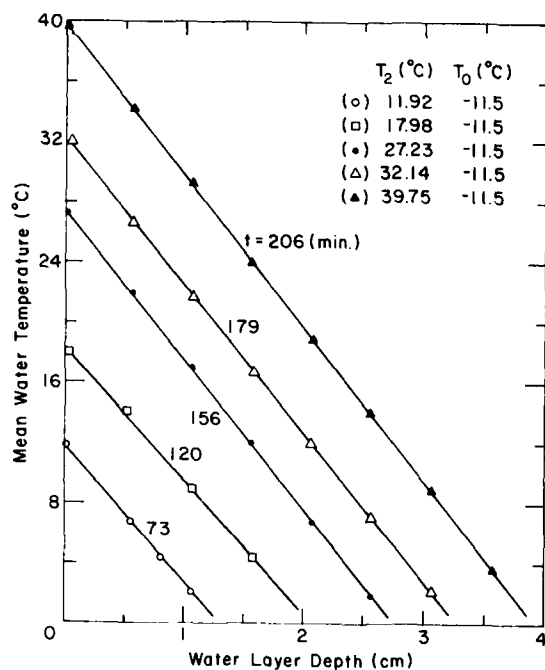


b. Development of the convective layer.

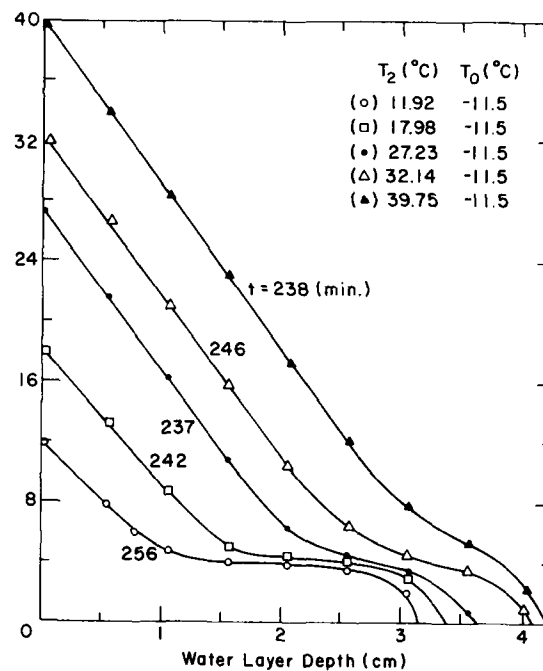


c. Pseudo-steady state.

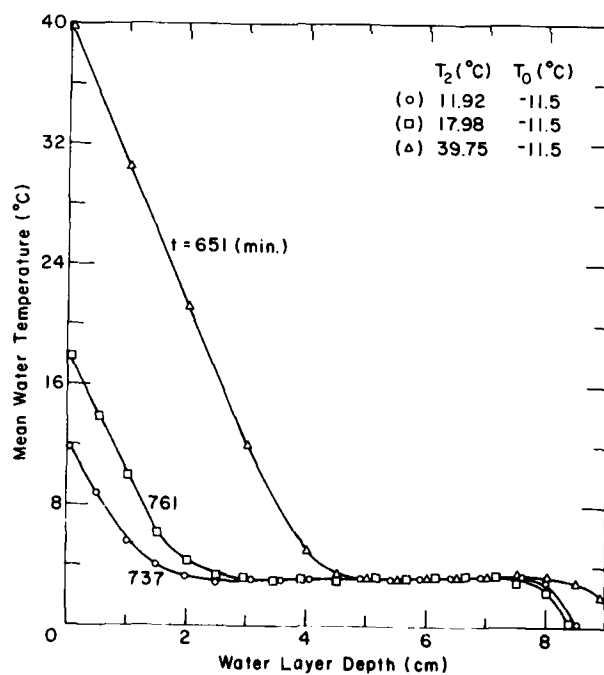
Figure 67. Mean temperature profiles for melting from below (after Yen 1984).



a. Before onset of convection.



b. Development of the convective layer.



c. Pseudo-steady state.

Figure 68. Mean temperature profiles for melting from above (after Yen 1984).

where L_f = latent heat of fusion
 C_i and T_i = specific heat and temperature of ice
 ρ = water density
 T_{io} = the ice initial temperature.

The term $(\rho c_p / 2t)[z(t)(T_m + T)]$ represents the mean sensible heat content variation of the entire layer of a depth $z(t)$. Since $T_m = 0^\circ\text{C}$, therefore, T stands for either T_1 or T_2 . The contribution of this term to the overall heat flux was found to be much more significant in the case of melting from above (since the melting rate is much slower in the case). For experiments in which the mean layer temperature was measured as the melting progressed, the heat flux was approximated by

$$q = \frac{\sum \frac{k}{2} \left[\left(\frac{dT}{dz} \right)_2 + \left(\frac{dT}{dz} \right)_1 \right] (t_2 - t_1)}{\Delta t} \quad (92)$$

in which $(dT/dz)_2$ and $(dT/dz)_1$ are the mean temperature gradients at the stable region near the upper boundary for melting from above, and at the lower warm plate for melting from below. Subscripts 1 and 2 indicate the beginning and end of each period and Δt is the total time period for calculating a value of q . At least a dozen or more of the periods (with varying durations) were used. The heat from above was found to be a rather weak function of T_2 and can be represented by

$$q = 177 (T_2)^{0.303} \quad (93)$$

Eq 93 is valid for T_2 ranging from 11.75 to 39.9°C. For melting from below, the heat flux is found to be a linear function of T_1 and can be expressed as

$$q = -1900 + 315 (T_1) \quad (94)$$

for T_1 ranging from 7.7 to 25.5°C. Higher values of T_1 and thus higher temperatures in the convective zone, resulted in greater convective motion in the unstable region and consequently reduced the thickness of the stable layer adjacent to both the ice and the thermal boundary. The work of Townsend (1964) and Adrian (1975) is similar to the case of melting from above. However, in their investigations, a rather deep invariant water layer was used throughout the experiment and there was no phase transition taking place at the bottom of the tank. Both Townsend (1964) and Adrian (1975) reported a nearly constant heat flux of approximately 340 W/m² independent of the initial water temperature.

Melting in bulk water

Merk (1954) reported the most comprehensive and earliest theoretical study of melting free convective heat transfer, such as that for spheres and cylinders. Employing a third-order density-temperature polynomial of water density and applying the Von Karman-Pohlhausen integral method for the case of $Pr \gg 1$, he successfully solved the boundary layer equation and developed a general Nusselt number ratio:

$$\frac{Nu}{Nu_0} = \left[\left(P_1 + \frac{6715}{13671} P_2 m + \frac{8471}{31031} P_3 n \right) \frac{[1 + (S/2)]^3}{1 - St} \right]^{1/4} \quad (95)$$

where S is the shape factor of the temperature profile and is connected to the Stefan number $St = c_p(T_m - T_\infty)/L_f$ as

$$S = -2 + \frac{3}{St} - \frac{3}{St} \sqrt{1 - \frac{4}{3} St} \quad (96)$$

or

$$St = \frac{6S}{(S+2)^2}, \quad (97)$$

where T_∞ is the bulk water temperature. The values of P_1 , P_2 and P_3 are expressed as

$$P_1 = 1 - \frac{89}{217} S + \frac{19}{434} S^2$$

$$P_2 = 1 - \frac{765}{1343} S + \frac{303}{2686} S^2 - \frac{19}{2686} S^3$$

and

$$P_3 = 1 - \frac{6475}{8471} S + \frac{3537}{16942} S^2 - \frac{199}{8471} S^3 + \frac{19}{16942} S^4.$$

The values of m and n are defined, respectively, as

$$m = (\beta_2'' + 3 \beta_3'' T_\infty) \theta_m / N \beta_\infty$$

$$n = \beta_3'' \theta_m^2 / (N \beta_\infty)$$

where $\theta_m = T_m - T_\infty$ and N and β_∞ are defined as

$$N = 1 + \beta_1'' T_\infty + \beta_2'' T_\infty^2 + \beta_3'' T_\infty^3$$

and

$$\beta_\infty = (\beta_1'' + \beta_2'' T_\infty + 3\beta_3'' T_\infty^2) / N$$

in which the β 's are the coefficient in the formula for the specific volume of the water, i.e.,

$$\frac{1}{\rho} = \frac{1}{\rho_0} (1 + \beta_1'' T + \beta_2'' T^2 + \beta_3'' T^3) \quad (97a)$$

Nu_0 is the Nusselt number for the case of $St = m = n = 0$. Merk (1954) reported that for large values of the Prandtl number, neither the shape of the body nor the position on the surface influences the ratio Nu/Nu_0 . Therefore, this ratio can be replaced by Nu/Nu_0 , which can be expressed by the following if only the effect of melting is considered (i.e., for $m = n = 0$)

$$\frac{\overline{Nu}}{Nu_0} = \left[\frac{1 - \frac{89}{217} S + \frac{19}{434} S^2}{1 - \frac{1}{2} S + \frac{1}{4} S^2} \left(1 + \frac{1}{2} S \right)^5 \right]^{1/4}. \quad (98)$$

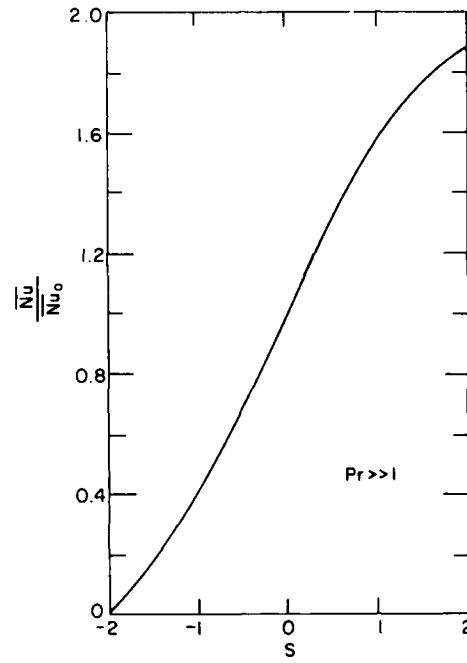


Figure 69. The influence of melting ($S < 0$) and solidification ($S > 0$) on the heat transfer in thermal convection for large Prandtl numbers (after Merk 1954).

Figure 69 is a graphic representation of eq 98; it clearly shows that for $S < 0$ or for melting, $\overline{Nu} < \overline{Nu}_0$. For solidification, i.e., $S > 0$, $\overline{Nu} > \overline{Nu}_0$. For the case of no melting, but with convective inversion, then $S = 0$ and hence $P_1 = P_2 = P_3 = 1$. Eq 95 becomes

$$\frac{\overline{Nu}}{\overline{Nu}_0} = (1 + 0.4912 m + 0.2730 n)^{1/4}. \quad (99)$$

By defining \overline{Nu}_0 for large values of the Prandtl number as

$$\overline{Nu}_0 = C (GrPr)^{1/4} = C \left(\frac{gL^3}{\alpha\nu} \beta_\infty \theta_m \right)^{1/4} \quad (100)$$

eq 99 can be written as

$$f = \frac{\overline{Nu}}{\left(C \frac{gL^3}{\alpha\nu} \right)^{1/4}} = [\beta_\infty \theta_m (1 + 0.4912 m + 0.2730 n)]^{1/4} \quad (101)$$

where f is a dimensionless number. For small values of T_∞ , $\beta_\infty \approx \beta_1'' + 2\beta_2'' T_\infty$, $m = \beta_2' \theta_m / \beta_\infty$, and $n \approx 0$, eq 101 can be transformed to

$$f = [1.509 \beta_2 |T_\infty - T_{iv}| |T_m - T_\infty|]^{1/4} \quad (102)$$

in which T_{iv} is the inversion temperature:

$$T_{iv} = -0.663 \frac{\beta_1''}{\beta_2''} - 0.326 T_m. \quad (103)$$

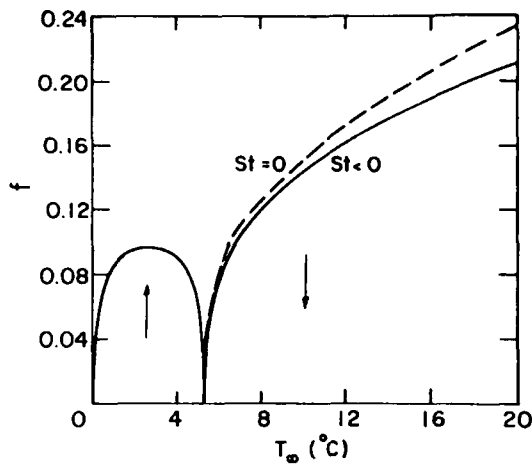


Figure 70. Convective inversion for melting ice in water of temperature T_∞ . The arrows indicate the direction of the flow along the surface. The dashed curve shows the behavior neglecting melting, while the full curve of the melting is taken into account (after Merk 1954).

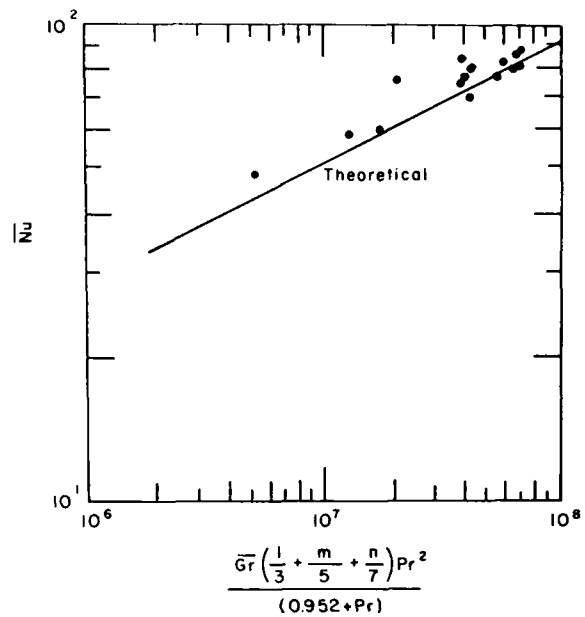


Figure 71. Comparison of theoretical (eq 109) and experimental Nu for unidirectional convection (after Schechter and Isbin 1958).

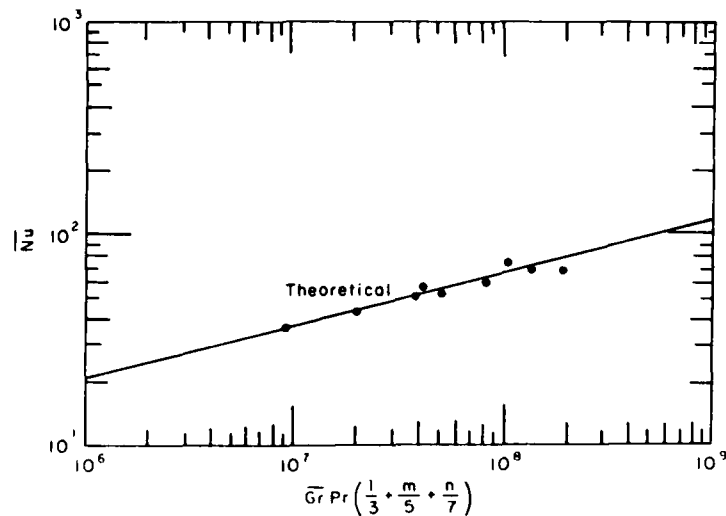


Figure 72. Comparison of theoretical (eq 110) and experimental Nu for inverted regime (after Schechter and Isbin 1958).

Using appropriate values of β_1'' and β_2'' and taking $T_m = 0^\circ\text{C}$, Merk reported a value of $T_{iv} = 5.005^\circ\text{C}$, indicating that the inversion temperature for melting ice in water is somewhat greater than $\approx 4^\circ\text{C}$. The significance of the inversion temperature is clearly seen from eq 102 at $T_\infty = T_{iv}$, $Nu = 0$, and the direction of the flow in the boundary layer along the surface of the body is inverted (for $T_\infty < T_{iv}$ the flow is upward and for $T_\infty > T_{iv}$ it is downward). Using the general eq 95, Merk derived the minimum Nusselt number at $T_{iv} = 5.30^\circ\text{C}$ for $S = 0$ (no melting) and $T_{iv} = 5.31^\circ\text{C}$ for $S < 0$ (with

melting). Figure 70 shows the effect on the value of f (i.e., the value of \overline{Nu}) with and without melting with the convective inversion. It is clearly shown that the effect of melting is only appreciable for $T_\infty > T_{iv}$ and may be neglected for $T_\infty < T_{iv}$. Experimental results of Dumoré et al. (1953) and analytical results from the non-melting vertical plate study by Ede (1955) generally confirmed Merk's findings.

Tkachev (1953), using photographic techniques, reported a minimum Nusselt number for melting ice cylinders at 5.5°C and was the first to notice the peculiar nature of the maximum density boundary layer. He suggested that under certain conditions the boundary layer might be split, with a region of predominantly upward motion immediately adjacent to the ice surface and a region of downward motion outside this. Tkachev conducted melting experiments on spheres as well as on vertical and horizontal cylinders. Using the same initial cylinder diameters but with various bulk water temperatures, he found that the coefficient of heat transfer is lowest for a water temperature of about 5.5°C. He correlated his data with the following dimensionless expressions as

$$Nu_{md} = 0.40 (GrPr)_{md}^{1/4} \quad (104)$$

and

$$Nu_{md} = 0.104 (GrPr)_{md}^{1/4} \quad (105)$$

for cylinders for the values in the range of $10^2 < GrPr < 10^7$ and $(GrPr)_{md} > 10^7$, respectively. The corresponding equations for spheres are

$$Nu_{md} = 0.54 (GrPr)_{md}^{1/4} \quad (106)$$

for laminar flow [$10^3 < (GrPr)_{md} < 10^7$] and

$$Nu_{md} = 0.135 (GrPr)_{md}^{1/4} \quad (107)$$

for turbulent motion [$(GrPr)_{md} > 10^7$]. Subscript md represents the physical properties, and the diameter of the sphere or cylinder was evaluated at the arithmetic mean temperature [i.e., $(T_m + T_\infty)/2$] and mean diameter [i.e., $(d_0 + d_f)/2$] where d_0 and d_f are the initial and final diameter at the end of the experiment. Based on his experimental data, Tkachev further presented an expression for determining the time required for completing melting as

$$StFo_{md} Nu_{md} = 0.305. \quad (108)$$

The suggestion of split boundary layer flow was verified by the analytical and experimental work of Schechter and Isbin (1958), in which an isothermal, vertical, non-melting plate was used. Figures 71 and 72 compare the theoretical and experimental results for the unidirectional and inverted convections, respectively. The theoretical curves in Figures 71 and 72 are given by

$$\overline{Nu} = 0.892 \left[\frac{\overline{Gr} \left(\frac{1}{3} + \frac{m}{5} + \frac{n}{7} \right)}{(0.952 + Pr)} \right]^{1/4} Pr^{1/2} \quad (109)$$

and

$$\overline{Nu} = 0.652 \left[\overline{Gr} Pr \left(\frac{1}{3} + \frac{m}{5} + \frac{n}{7} \right) \right]^{1/4} \quad (110)$$

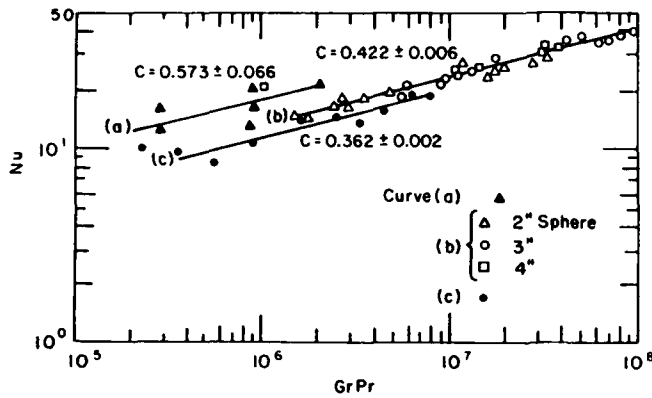


Figure 73. Nusselt number as function of Rayleigh number ($GrPr$) (after Vanier and Tien 1970).

where m and n are the same as appeared in eq 95. They reported that a test of the type of region that will prevail for given conditions of plate and bulk temperature can be stated; i.e., if

$$\frac{1}{3} + \frac{m}{5} + \frac{n}{7} \geq 0,$$

there will be normal convection (unidirectional), and if

$$\frac{1}{3} + \frac{m}{5} + \frac{n}{7} < 0,$$

there will be inverted convection. Schechter and Isbin (1958) concluded that the heat transfer coefficient can be predicted for both regions with a deviation in Nusselt number of $\pm 10\%$, provided the absolute value of $(1/3 + m/5 + n/7) > 0.05$ by use of eq 109 or 110, depending on the convective region. However, the boundary layer equations as approached either by the Von Karman-Pohlhausen integral method or by the similarity transformation method did not yield meaningful results under split-flow conditions.

To resolve this problem Vanier and Tien (1968) used an accurate numerical method to solve the similarity equations for a semi-infinite vertical plate at constant temperature T_w immersed in an indefinitely large volume of water at bulk temperature T_∞ . They reported that a new solution is necessary for every combination of T_w and T_∞ . By obtaining several hundred such solutions, the authors were able to map out temperature zones for each flow regime. The split boundary layer was found to be confined to two distinct triangular regions within which the similarity equations become quite intractable. They confirm the findings of Merk (1954) that the melting heat transfer rates were very similar to those for the case of non-melting.

Vanier and Tien (1970) conducted experimental work aimed at relating their numerical plate results to a more practical geometry of the sphere (including the effect of changing body configuration). This was also partially motivated by lack of detailed analysis and correlations of the experimental results on the melting of ice spheres and cylinders presented by Dumoré et al. (1953) and Tkachev (1953). They presented their results in a least-squares-fitted semi-empirical equation as

$$Nu = 2 + C (GrPr)^{1/4} \quad (111)$$

and found that for $T_\infty > 7^\circ\text{C}$, that the results did not appear to be affected by the maximum density and that the most appropriate value of C is 0.422 ± 0.006 in the range of $1.7 \times 10^6 < GrPr < 2.4 \times 10^8$ (Fig. 73, curve b). However, for $T_\infty < 7^\circ\text{C}$, nearly the same value of C is found but with considerably more scattering (twice the standard deviation), indicating the need at least to incorporate another parameter

Figure 74. Nusselt number variation with bulk temperature for approximately constant sphere diameters (after Vanier and Tien 1970).

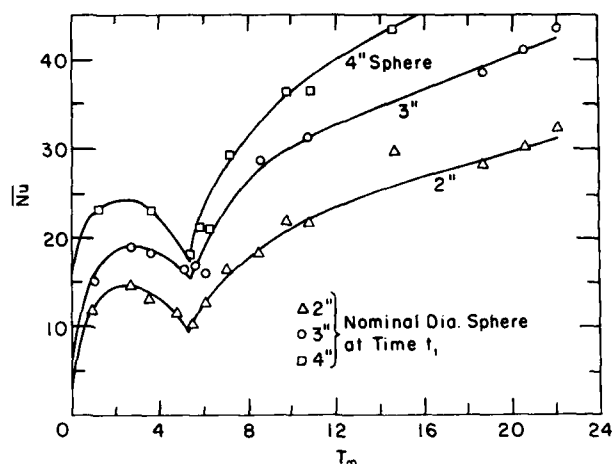
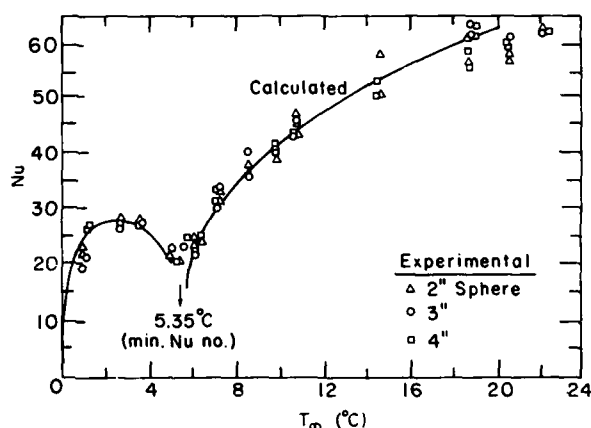


Figure 75. Correspondence between the melting of flat plates and spheres of ice (after Vanier and Tien 1970).



such as T_{∞} to adequately describe the heat transfer under these conditions. This was done by separating the low temperature data into positive and negative deviations. For $T_{\infty} < 3.8^{\circ}\text{C}$, Nu values are higher than expected (curve a), while for $4.1^{\circ} < T_{\infty} < 7.1^{\circ}\text{C}$, Nu values are too low (curve c). To check the one-quarter power assumption in eq 111, a two-parameter fit was carried out, resulting in

$$Nu = 2 + 0.437 (GrPr)^{0.248} \quad (112)$$

which provides an excellent verification. However, when the Grashof number was calculated by using an arithmetic mean temperature basis of T_{∞} , the constant C was found to be 0.52 for $T_{\infty} > 14^{\circ}\text{C}$. This provides a remarkable agreement with the results reported by Tkachev (1953). The effect of sphere diameter and maximum density on heat transfer can be seen in Figure 74 where the curves are in general agreement with the flat plate results reported by Vanier and Tien (1968), which show a sharp minimum between $5^{\circ} < T_{\infty} < 6^{\circ}\text{C}$. To ascertain the effect of sphere diameter, Vanier and Tien (1970) proposed a correlation of the sphere results with those from theoretical analysis of a melting plate by

$$\overline{Nu}_p / \overline{Nu} = C (L/D)^{3/4} \quad (113)$$

where L and D are the characteristic height of the plate and the diameter of the sphere. The least-squares-fitted constant C was found to be 1.106 ± 0.144 . The scaled-up experimental data are shown in Figure 75, which clearly shows that the melting sphere behaves very similarly to a melting flat plate and that if all the transfer parameters are equal (including temperature, characteristic length, and surface area), about 11% more heat is transferred to the plate than to the sphere. This is the effect of

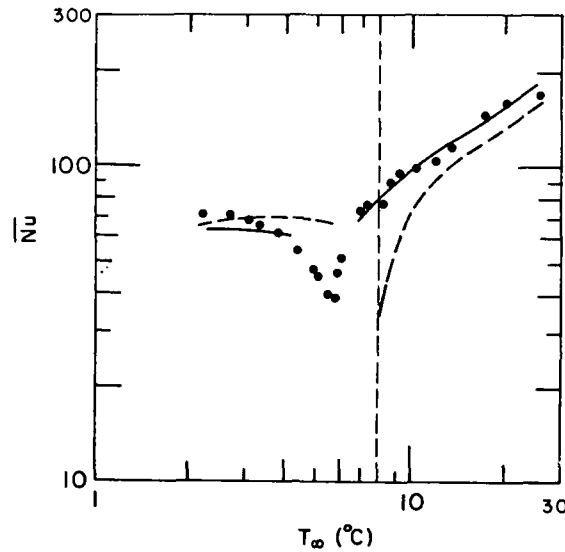


Figure 76. Variation of mean Nusselt numbers with ambient temperature T_{∞} (experimental results). The solid curve is from the analytical work of Gebhart and Mollendorf (1978), the dashed curve is the prediction with the Boussinesq approximation (after Bendell and Gebhart 1976).

curvature on the flow velocities and is in good agreement with the analytical results reported by Merk and Prins (1954) for non-melting free convection systems without maximum density effects, i.e.,

$$\overline{Nu_p} / \overline{Nu} = 1.14 (L/D)^{3/4}. \quad (114)$$

The minimum Nusselt number for spheres occurs at $T_{\infty} = 5.35 \pm 0.2^{\circ}\text{C}$, as compared to the value of 5.31°C based on Merk's (1954) theoretical results.

The most recent study of heat transfer and ice melting in ambient water near its density extremum was reported by Bendell and Gebhart (1976). In their experiment, a vertical ice slab (30.3 cm high, 14.8 cm wide and 3 cm thick initially) was immersed in water at a uniform bulk ambient temperature, T_{∞} . Figure 76 shows the experimental results along with the analytical results of Gebhart and Mollendorf (1978) and those predicted with the Boussinesq approximation. Gebhart and Mollendorf's work is similar to that of Vanier and Tien (1968) except that it gives a more accurate representation of the density-temperature relationship of water. As Vanier and Tien pointed out, the validity of the simplest boundary layer theory becomes questionable in the inversion region. However, beyond that region, the experimental Nusselt number values are nearly equal to those predicted by theoretical analysis. Bendell and Gebhart (1976) reported that for a melting vertical ice surface, upflow occurred when $T_{\infty} \leq 5.6^{\circ}\text{C}$. For $T_{\infty} \geq 5.5^{\circ}\text{C}$, downflow was observed and was found to be in good agreement with earlier results. Bendell and Gebhart (1976) found the minimum Nusselt number for the experimental temperature range $2.2^{\circ} \leq T_{\infty} \leq 25.2^{\circ}\text{C}$ occurred at $T_{\infty} = 5.6^{\circ}\text{C}$. In the immediate neighborhood of the flow direction inversion T_{iv} , very slow flow exists with the effective Grashof number becoming very small. Therefore, the validity of the simplest boundary-layer theory becomes questionable, and no theoretical results for this regime were found in the literature. After multiplication by a factor of $(0.102/0.303)^{1/4}$ (solid curve in Fig. 76), the theoretical results of Gebhart and Mollendorf (1978) generally compared remarkably well with those reported by Vanier and Tien (see solid curve in Fig. 75), even though a rather elaborate and more accurate density-temperature relationship of water was claimed to be used in Gebhart and Mollendorf's study.

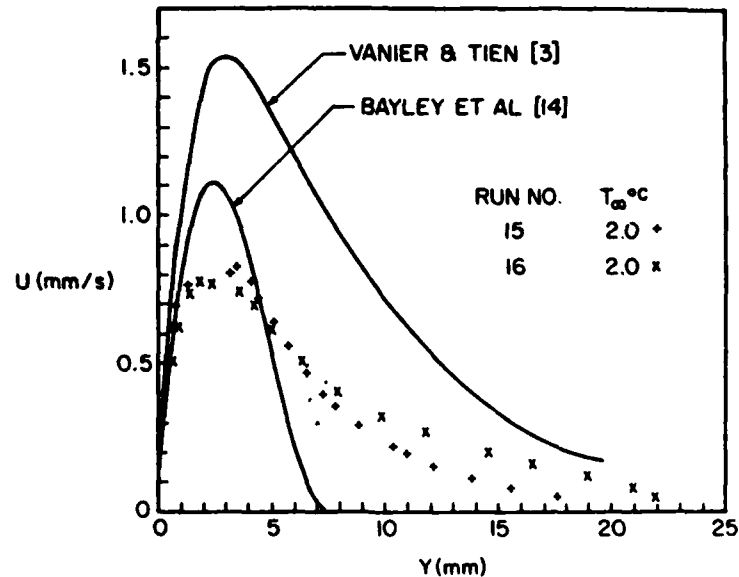


Figure 77. Velocity profiles for $T_{\infty} = 2.0^{\circ}\text{C}$ (Wilson and Vyas 1979).

Wilson and Vyas (1979) reported the only experimental results concerning a velocity profile near a vertical ice surface melting into fresh water at temperatures from 2° to 7°C . The results suggested that upward flows exist for water temperatures below 4.7°C . Completely downward flowing boundary layers are suggested for temperatures about 7°C . At 4.7°C an oscillatory dual flow situation begins to occur. As the temperature is increased, this phenomenon is increasingly prevalent, with increasing downward velocities reaching a maximum at 5.6°C . Figure 77 shows a comparison between the Wilson and Vyas (1979) experimental data and predictions obtained from free convective boundary layer theories by Bagley et al. (1972) and Vanier and Tien (1970). The work of Bagley et al. predicts a maximum velocity higher than that of the data and a significantly thinner boundary layer thickness. Disagreement may be attributed to the high degree of sensitivity of the analysis to the fluid density.

As indicated in Figure 78a as the water temperature rises to 3.2°C , the net buoyancy forces increase resulting in an increase in the maximum velocity. At 4.4°C , the flow is still upward, although the maximum velocity is lower and the boundary layer is slightly thinner than at 3.2°C (Fig. 78b), because of the downwards buoyancy occurring in the portion of the profile with the temperature between 4° and 4.4°C . At 4.7°C (Fig. 78c) a similar but stronger tendency is noted as the result of the increased downward buoyancy existing in the outer portion of the boundary layer. The distinct difference in the two maximum velocities suggested the oscillating nature of the water flow at this temperature.

At 5°C (Fig. 79a) the oscillatory dual flow characteristics are clearly established, and it can be noted that the upward flowing portion is substantially thinner and is accompanied by a decrease in the maximum upward velocity when downflow exists. This trend is continued for $T = 5.3^{\circ}$, 5.6° and 5.9°C as shown in Figures 79b, c and d, respectively. In each case, oscillatory dual flow exists continuously; i.e., upward flows were not observed at any time beyond the near-wall upward flow region. At 5.3°C , the position of maximum downward velocity oscillates between 7.3 and 11.5 mm from the wall. For 5.6°C , it lies between 6 mm and 18 mm, but at 5.9°C , this variation is limited to 5.2 to 8.0 mm. In addition, the profiles at 5.9°C (Fig. 79d) pose much greater self-similarity than those of 5.3° and 5.6°C . Thus the flow phenomena for 5.3° and 5.6°C seem to be substantially more complex than that

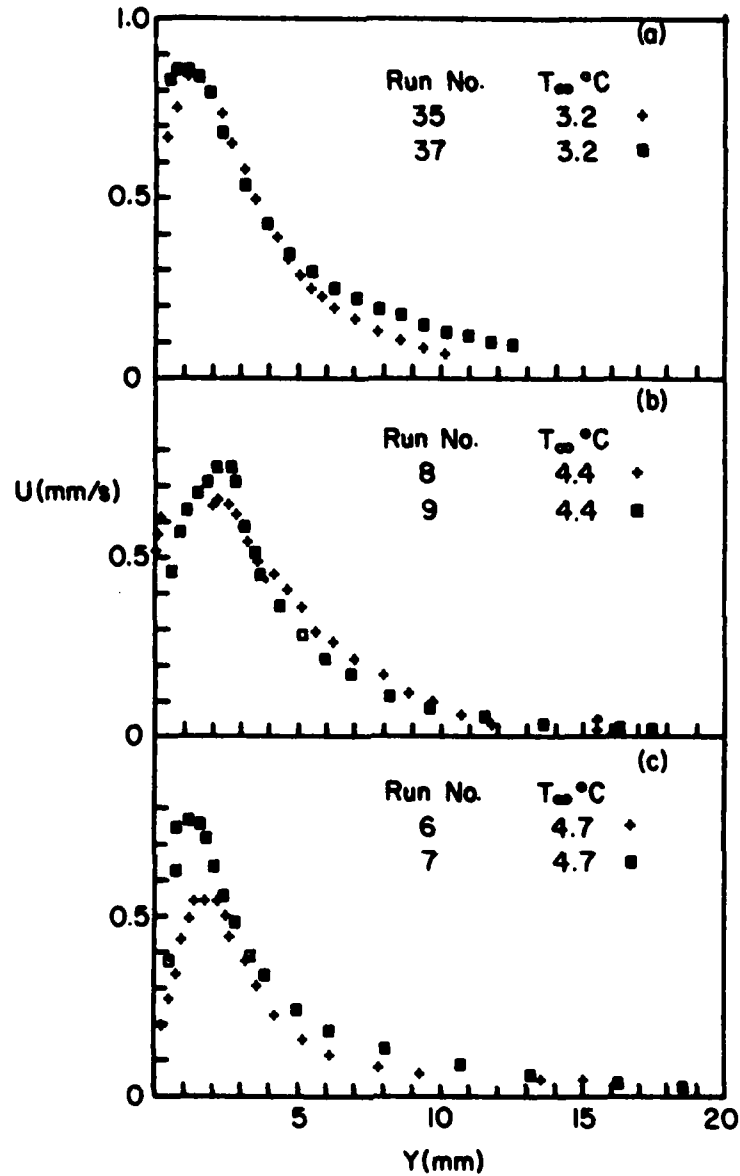
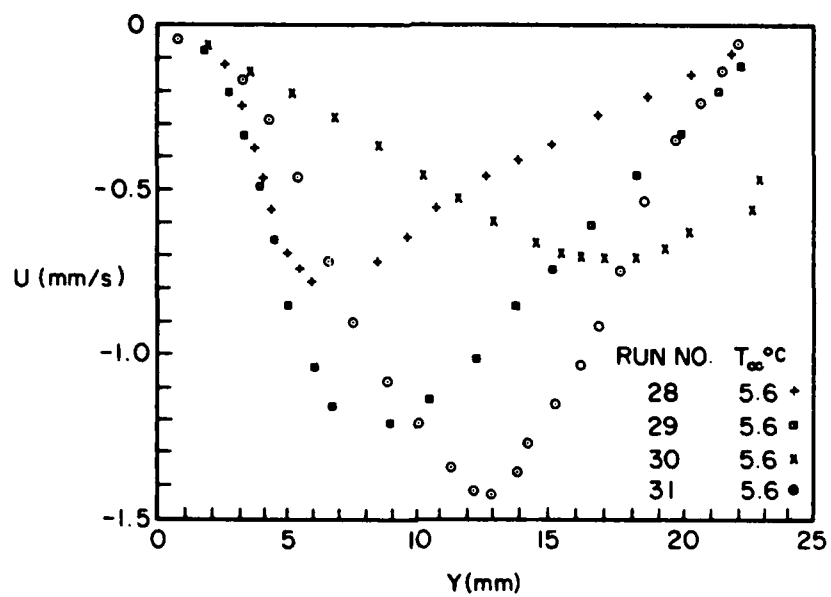
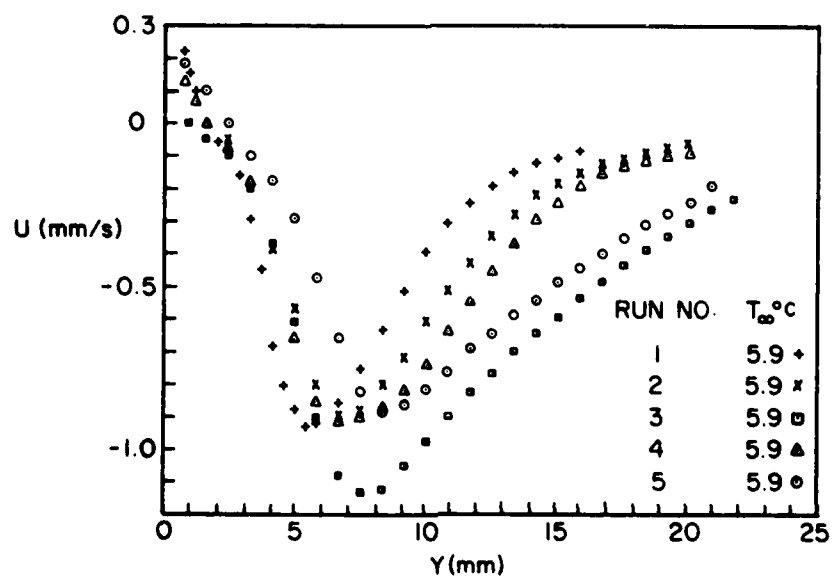


Figure 78. Velocity profiles for a) $T_{\infty} = 3.2^{\circ}\text{C}$, b) $T_{\infty} = 4.4^{\circ}\text{C}$ and $T_{\infty} = 4.7^{\circ}\text{C}$ (Wilson and Vyas 1979).

at 5.9°C . In both Figures 79b and 79d there are small regions of the order of 1 to 2 mm in thickness near the wall where upwards flow exists, while at 5.6°C much smaller velocities were observed within the same region but with much lower maximum velocity. Figure 79e shows the characteristics of a relatively stable downward flow regime. In this case, the portion of the boundary layer with upward buoyancy is approximately 0.5 to 1.0 mm in thickness. The downward buoyancy forces in the outer portion are much stronger and the whole flow is downward, because the viscous forces, which tend to draw the fluid downward, approximately balance the upward buoyancy forces near the ice. The velocity gradient is approximately zero at the ice surface.

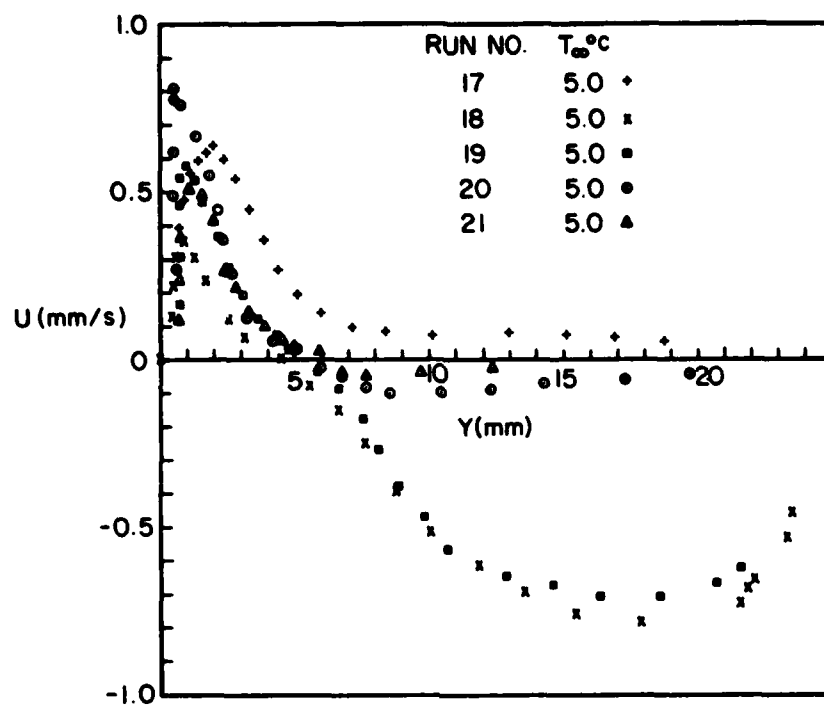


c. $T_{\infty} = 5.6^{\circ}\text{C}$.

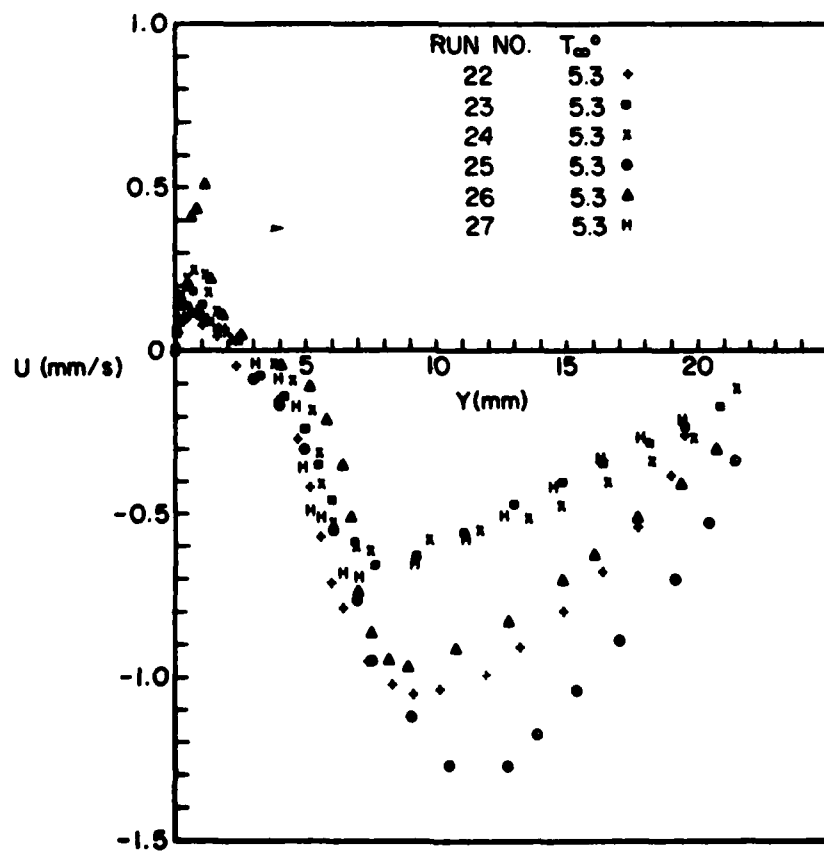


d. $T_{\infty} = 5.9^{\circ}\text{C}$.

Figure 79 (cont'd).

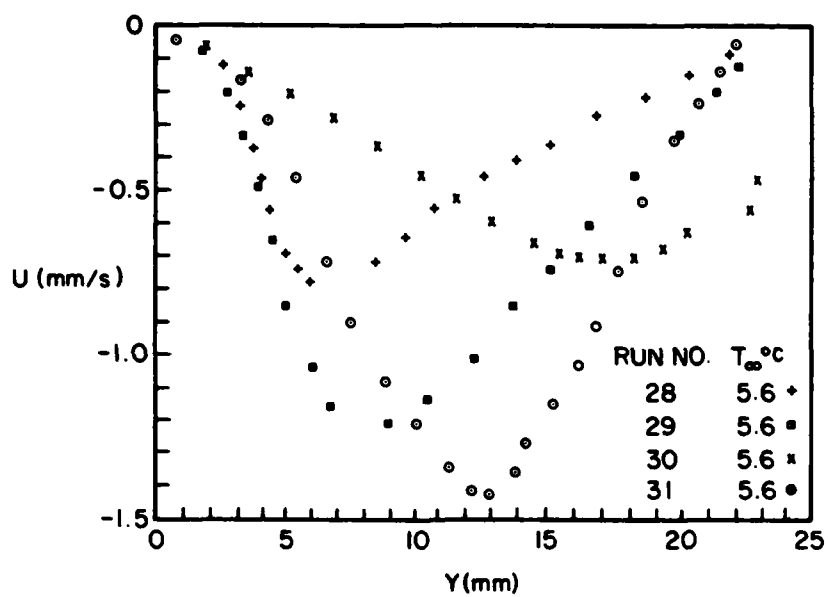


a. $T_{\infty} = 5.0^{\circ}\text{C}$.

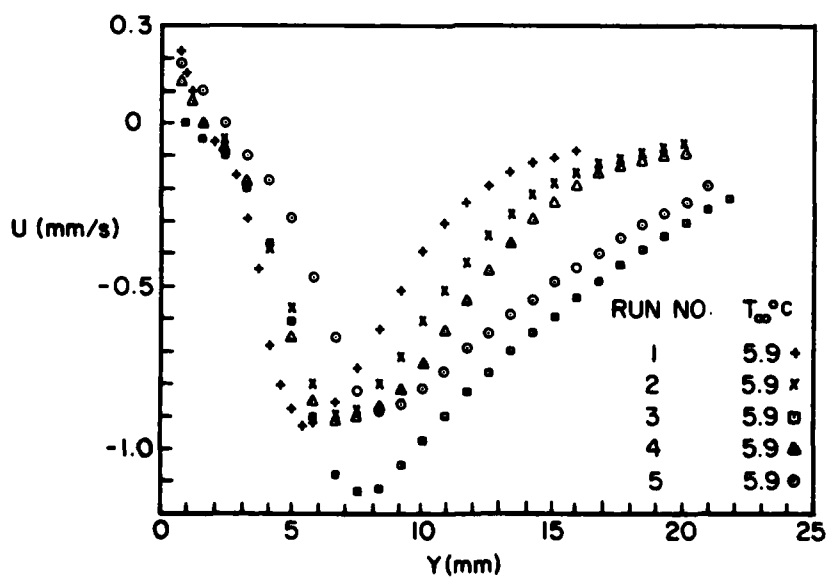


b. $T_{\infty} = 5.3^{\circ}\text{C}$.

Figure 79. Velocity profiles (Wilson and Vyas 1979).

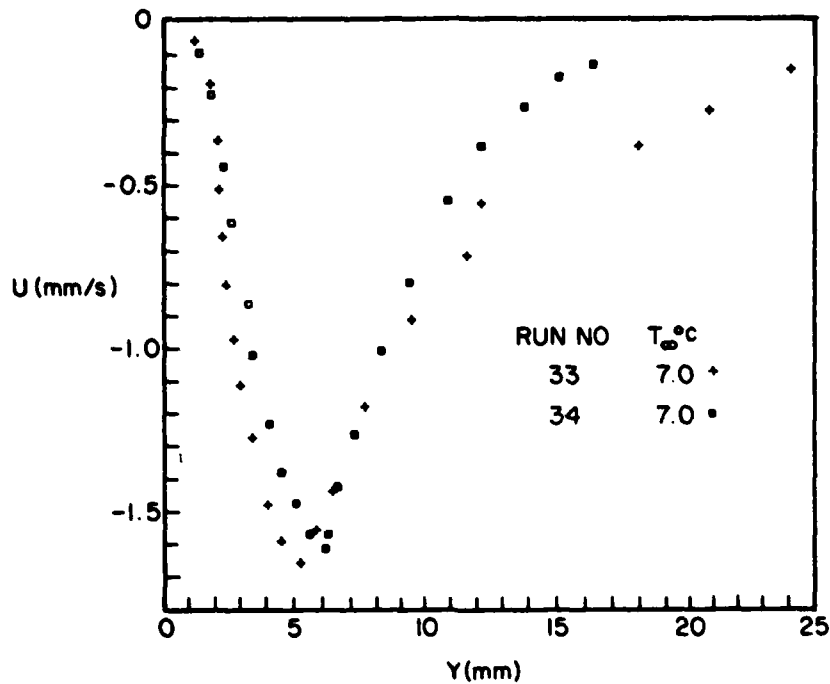


c. $T_{\infty} = 5.6^{\circ}\text{C}$.



d. $T_{\infty} = 5.9^{\circ}\text{C}$.

Figure 79 (cont'd).



e. $T_{\infty} = 7.0^{\circ}\text{C}$.

Figure 79 (cont'd). Velocity profiles.

DISCUSSION AND CONCLUSIONS

This review covers only the problems associated with the anomalous density-temperature relationship of water contained in various geometrical systems. The discussion and conclusion are classified into two subjects: 1) onset of convection, 2) flow patterns and natural convective heat transfer.

Onset of convection

The criterion for the onset of convection of a confined horizontal layer that contains a density extremum was found both experimentally (Yen 1968, Yen and Galea 1969) and analytically (Veronis 1963, Sun et al. 1969, Merker et al. 1979) to not be a constant value, as in the classical Benard problem, but dependent on the thermal boundary conditions.* This is evident in Figure 4, in which Ra_c was plotted explicitly vs T_1 or T_2 . In the case of melting from the top, the higher the values of T_2 , the greater Ra_c becomes; in other words, the farther removed temperature T_2 is from 4°C , the less prone the layer is to begin the onset of convection. In the case of melting from below, as temperature T_1 increases, Ra_c decreases exponentially and asymptotically approaches the value ≈ 1708 , as reported in the classical Benard problem. This is evident because, as T_1 becomes higher and higher, the buoyancy forces created by temperature difference $\Delta T (= T_1 - T_{\max})$ possess a much stronger influence on the layer stability than the effect produced by the density extremum (i.e., at $\approx 4^{\circ}\text{C}$), and subsequently the continuously forming layer behaves like a normal fluid (i.e., there is a monotonic

* If the layer is formed by phase transition, then one of the thermal boundaries is at the ice melting point, i.e., $T_m = 0^{\circ}\text{C}$.

density-temperature relationship) as in the Benard problem. On the other hand, as T_1 decreases and approaches the temperature of the density extremum, Ra_c increases and approaches the limiting value of infinity. This is also expected, since if T_1 is maintained at $\approx 4^\circ\text{C}$, the water has its greatest density at the lower boundary and the water layer will always remain stable.

In the case of a water layer formed by melting ice from above, the trend of variation of Ra_c with boundary temperature is simply reversed. The higher the temperature T_2 , the greater Ra_c becomes. This can be explained by noting that if T_2 is maintained in the range of $0 < T_2 \leq 4^\circ\text{C}$, the entire layer is unstable because the higher density water will overlies the less dense water underneath, and will consequently result in lower Ra_c values. If T_2 is maintained at a higher temperature than 4°C , only a fraction of the layer ($= 4H/T_2$) is potentially unstable, and the layer is less prone to onset of convection. It seems that the Ra_c value grows increasingly greater as the effect of the density extremum becomes less pronounced. It is also interesting to note that the two Ra_c curves intersect at exactly $T_1 = T_2 = 8^\circ\text{C}$, which clearly indicates that under these particular thermal conditions, the two systems are identical and have a unique Ra_c value regardless of how the water layer was formed.

In the case of a confined pure water layer, Merker et al. (1979) reported Ra_c values for both constant temperature and constant heat flux thermal boundaries. The effect of T_1 and T_2 on Ra_c seems to be similar but with higher values of Ra_c for the cases of $T_w = \text{constant}$ (see Fig. 6 and 7). They indicated that the values for Ra_c depend on the specific values of T_1 and T_2 . A few comparisons between the results from Sun et al. and Merker et al. were found to be in good agreement.

The stability problem, equivalent to the case of melting from above, was studied by Seki et al. (1977) with the added condition of a free surface maintained either at $T_2 > 4^\circ\text{C}$ or $T_2 \leq 4^\circ\text{C}$ and T_1 at 0°C . For $T_2 < 8^\circ\text{C}$, they demonstrated both analytically and experimentally that the criterion of hydrodynamic stability in a water with a density inversion is dependent on the free water-surface temperature T_2 and increases as surface tension increases and decreases as T_2 is lowered, resulting in a reduction of the stable layer thicknesses. On the other hand, for $T_2 \geq 8^\circ\text{C}$, the criterion is found to be independent of T_2 and approaches asymptotically a limiting value of a modified critical Rayleigh number, i.e., $Ra_c \approx 500$, as predicted by Sun et al. (1969).

Hassab and Sorour (1982) reported the first analytical study on the stability of the conduction regime of natural convection in a vertical melt layer formed by melting ice. Their stability criterion is expressed in terms of critical Grashof number Gr_c . The values of Gr_c (and the corresponding critical melting thickness h_c) are dependent upon the stepped wall temperature T_1 , such that as T_1 is increased the change in heat transfer mode from conduction to convection is enhanced for all values of T_1 in the range of 1° to 30°C . They found that the instability sets in as vertical traveling waves, with the secondary flow occurring as two-column waves for $T_1 < 7.1^\circ\text{C}$ and $T_1 > 9.4^\circ\text{C}$, and as three-column waves for $7.1^\circ\text{C} < T_1 < 9.4^\circ\text{C}$.

Flow patterns and natural convective heat transfer

The most striking phenomenon that results from the presence of a fluid density maximum within a confined area is the creation of an unusual temperature distribution and its associated cellular formation and flow, which are directly related to geometrical arrangement (i.e., in a confined horizontal layer, in a vertical gap, in a cylindrical annulus, or in a rectangular and square enclosure). In a horizontal layer formed by melting ice (in this case, one in which the boundary is ice at its melting temperature), the transient temperature and its pseudo-steady temperature distribution can be represented as shown in Figures 67 and 68. It can be noted that the unique features of these distributions are the formation and expansion of the constant temperature region. The heat flux across the water/ice interface was found to be a weak function of temperature for the melt layer for the case of melting from above and a linear function of temperature for the case of melting from below.

Lankford and Bejan (1986) developed a unique heat transfer correlation based on scale analysis for water near 4°C . The curve shown in Figure 27 was obtained from eq 35, with $C_1 = 0.31$ and C_2

= 0.5, and a set of specific Rayleigh numbers based on the hot and cold sides boundary layers, respectively. Without this modification the ordinary correlation for normal fluids (or water warmer than 4°C), e.g., eq 25 or Figure 25, failed to represent the data, including the results for temperatures near 4°C or below.

Figures 29a, b, c, and d typically demonstrated the temperature distribution and cell rotation pattern in a square enclosure (aspect ratio, $A = 1$, $K \approx r_o/r_i = 1$; no curvature effect) as function of values of R' , when $R' = 0.5$ (i.e., when the maximum density is in the middle plane). The temperature distribution as well as the cell size are nearly identical except rotating in the opposite direction. When $R' = 1.0$, (i.e., the hot wall temperature is equal to the T_m), the water behaves as a normal Boussinesq fluid except for the direction of circulation. The effect of A on temperature distribution and flow pattern is clearly demonstrated in Figure 31. As A increases, the convection heat transfer occurs only at the top of the annulus, and not at the near-bottom, because of the dual cell structure. The effect of K and Ra' on the heat transfer at the inner wall (relative to conduction) is shown in Figure 33. From this study, it is evident that density inversion phenomena are altered substantially by the curvature of the annulus. A particular steady flow structure is determined by the combination of the inversion parameter R' and the curvature K . A transition from inner to outer convective cell dominance can be accomplished by either increasing R' or by increasing the curvature K of the annulus.

Seki et al. (1975) described the only experimental study of the effect of water near 4°C on natural convective heat transfer between two horizontal concentric cylinders. They reported that the effect of density inversion is unexpectedly large and, especially when two counter-eddies of approximately the same size coexist in the gap, the average Nusselt number indicated a minimum value and the minimum Nu increasing as the gap width increased (see Fig. 39). However, there seemed to be no definite pattern as to the temperatures where the minimum heat transfer occurred.

The analytical work of Nguyen et al. (1982) confirmed the experimental findings of Seki et al. (1975). The pattern of circulation and angular velocity are functions of inversion parameters γ' as well as outer to inner radius ratio, i.e., R' and the Rayleigh number. A slight variation in γ' creates a radical change in cellular configuration. The minimum coefficient of convective heat transfer is found to deviate from $\gamma' = -1$ as R' increases (see Figs. 40, 41, 42 and 43).

The extension of this work by Vasseur et al. (1983) further delineated the temperature distribution and the circulation pattern within the cylindrical annulus, especially for high Rayleigh numbers. For $R' = 2.6$ and Ra_n varying from 2×10^3 to 7×10^4 , an overall minimum Nu was found to occur at $\gamma' = -0.85$. On the other hand for $Ra_n = 1 \times 10^4$, the minimum Nu occurs at $\gamma' > -1$ but approaches $\gamma' = -1$ as R' increases from 1.75 to 2.6.

The work of Watson (1972) and later Lin and Nansteel (1987a) on the effect of density inversion on the temperature distribution and heat transfer in a square enclosure is a special case of that for rectangular enclosures. Watson demonstrated that the variation of Nu with the warm temperature boundary T_1 between the full equation and constant viscosity model are negligible for $T_1 < 8^\circ\text{C}$ but deviate from each other as $T_1 > \sim 9^\circ\text{C}$. On the other hand, the Boussinesq model displayed a completely different heat transfer phenomenon (see Fig. 47). For a square enclosure, for R' values ranging from 0 to 1, the average Nu was found to be symmetrical with respect to $R' = 0.5$, with a minimum at $R' = 0.5$, and increases as Ra increases.

For rectangular enclosures, Desai and Forbes (1981) numerically calculated that the Nusselt number is always higher for the $T_c - T_h$ range of 0° to 8°C than for the $T_c - T_h$ range of 2° to 6°C (although for both cases $R' = 1/2$) independent of the temperature-density representation and aspect ratio. Nansteel et al. (1987) also found that the value of Nu is very sensitive to R' as well as the aspect ratio. The minimum Nu occurs at $R' = 1/2$, and it increases with increasing A .

The effects of 4°C on the natural convective heat transfer and temperature distribution with initial temperatures at 4° and 8°C were reported by Forbes and Cooper (1975) who cooled water from the top with either a rigid boundary condition at constant temperature or a free water-air surface with constant convective heat transfer coefficient. They demonstrated that the eddy's formation is closely related to the position of the maximum isotherm. At the beginning, one cell was formed below the

4°C line (square enclosure). As the 4°C curve descended farther, two cells were formed on top of each other, with part of the 4°C line as the boundary and, finally, the two cells returned to one eddy (or one cell) as the 4°C line progressed through the bottom of the container. For $W/D > 1$, the same mechanism of cell formation was observed, but the number of eddies formed was not in any way related to the values of W/D . (Based on limited data, for $W/D = 3$, three eddies with unequal size were formed; however, for $W/D = 6$, seven eddies were noted.)

Yen (1968) and Yen and Galea (1969) performed the only experimental work on temperature distribution and heat transfer in a melt layer formed by melting ice (with ice initially at its fusion temperature). Four cases of melting layers were set up, with $T_1 \geq 4^\circ\text{C}$ (melting from below) and $T_2 \geq 4^\circ\text{C}$ (melting from above). In the case of $T_1 = 4^\circ\text{C}$ the whole melt layer was always stable, but for $T_2 = 4^\circ\text{C}$ the whole layer was unstable. For T_1 and $T_2 > 4^\circ\text{C}$, the melt layer consisted of one stable and one unstable region. The effects of these unstable regions on temperature distribution, heat transfer and onset of convection were found dependent on mode of melting. The most striking feature in the ice-melting system was the formation and expansion of the constant temperature zone, which had a temperature of about 3.2°C , regardless of the value of T_2 , but had a dependency on T_1 in the case of melting from below.

For the case of ice melting in bulk water, experimental and analytical studies reveal the existence of split-flow at the inversion temperature T_{iv} , (i.e., for $T_\infty < T_{iv}$ the boundary layer flow is upward, and for $T_\infty > T_{iv}$ the entire boundary layer is downward). The inversion temperature was found to be about 5° or 6°C for a great number of phase-transition geometries, but not at the temperature of maximum density ($\approx 4^\circ\text{C}$).

LITERATURE CITED

- Adrian, R.J. (1975) Turbulent convection in water over ice. *Journal of Fluid Mechanics*, **69**: 753–781.
- Bagley, F.J., J.M. Owen and A.B. Turner (1972) *Heat Transfer*. Thomas Nelson and Sons Ltd., p. 211–212.
- Bejan, A. (1979) A note on Gill's solution for free convection in a vertical enclosure. *Journal of Fluid Mechanics*, **90**: 561–568.
- Bejan, A. (1984) *Convection Heat Transfer*. New York: Wiley.
- Bendell, M.S. and B. Gebhart (1976) Heat transfer and ice melting in ambient water near its density extremum. *International Journal of Heat and Mass Transfer*, **19**: 1081–1087.
- Chandrasekhar, S. (1961) *Hydrodynamic and Hydromagnetic Stability*. Oxford: Clarendon Press.
- Debler, W.R. (1966) On the analogy between thermal and rotational hydrodynamic stability. *Journal of Fluid Mechanics*, **24**: 165–177.
- Desai, V.S. and R.E. Forbes (1971) Free convection in water in the vicinity of maximum density. *Environmental and Geophysical Heat Transfer*, **HTD-4**: 41–47.
- Dumore, J.M., H.J. Merk and J.A. Prins (1953) Heat transfer from water to ice by thermal convection. *Nature*, **172**: 460–461.
- Ede, A.J. (1955) The influence of anomalous expansion on natural convection in water. *Applied Scientific Research*, **5**: 458–460.
- Forbes, R.E. and J.W. Cooper (1975) Natural convection in a horizontal layer of water cooled from above to near freezing. *Journal of Heat Transfer*, **97**: 47–53.
- Gebhart, B. and J.C. Mollendorf (1978) Buoyancy-induced flows in water under conditions in which density extrema may arise. *Journal of Fluid Mechanics*, **89**(4): 673–707.
- Hassab, M.A. and M.M. Sorour (1982) Onset of convection in a melted ice layer between vertical plates. *International Journal of Heat and Mass Transfer*, **25**: 909–916.
- Kimura, S. and A. Bejan (1984) The boundary layer natural convection regime in rectangular cavity with uniform heat flux from the side. *Journal of Heat Transfer*, **106**: 98–104.

- Lankford, K.E. and A. Bejan** (1986) Natural convection in a vertical enclosure filled with water near 4°C. *Journal of Heat Transfer*, **108**: 755–763.
- Legros, J.C., D. Longree and G. Thomas** (1974) Benard problem in water near 4°C. *Physica*, **72**: 410–414.
- Lin, D.S. and M.W. Nansteel** (1987a) Natural convection heat transfer in a square enclosure containing water near its density maximum. *International Journal of Heat and Mass Transfer*, **30**: 2319–2329.
- Lin, D.S. and M.W. Nansteel** (1987b) Natural convection in a vertical annulus containing water near the density maximum. *Journal of Heat Transfer*, **109**: 899–905.
- Lunardini, V.** (1981) *Heat Transfer in Cold Climates*. New York: Van Nostrand Reinhold Company.
- Lunardini, V.** (1988) Heat conduction with freezing or thawing. USA Cold Regions Research and Engineering Laboratory, CRREL Monograph 88-1.
- Merk, H.J.** (1954) The influence of melting and anomalous expansion on the thermal convection in laminar boundary layers. *Applied Scientific Research*, **4(A)**: 435–452.
- Merk, H.J. and J.A. Prins** (1954) Thermal convection in laminar boundary layers III. *Applied Scientific Research* **4(A)**: 297–223.
- Merker, G.P., P. Wass and U. Grigull** (1979) Onset of convection in a horizontal water layer with maximum density effects. *International Journal of Heat and Mass Transfer*, **22**: 505–515.
- Nansteel, M.W., K. Medjani and D.S. Lin** (1987) Natural convection of water near its density maximum in a rectangular enclosure: low Rayleigh number calculations. *Physics of Fluids*, **30**: 312–317.
- Nguyen, T. Hung, P. Vasseur and L. Robillard** (1982) Natural convection between horizontal concentric cylinders with density inversion of water for low Rayleigh numbers. *International Journal of Heat and Mass Transfer*, **25**: 1559–1568.
- Seki, N., S. Fukusako and M. Nakaoka** (1975) Experimental study on natural convection heat transfer with density inversion of water between two horizontal concentric cylinders. *Journal of Heat Transfer*, **97**: 556–561.
- Seki, N., S. Fukusako and M. Sugawara** (1977) A criterion of onset of free convection in a horizontal melted water layer with free surface. *Journal of Heat Transfer*, **99**: 92–98.
- Schechter, R.S. and H.S. Isbin** (1958) Natural convection heat transfer in regions of maximum fluid density. *American Institute of Chemical Engineers Journal*, **4**: 81–89.
- Sun, Z.-S., C. Tien and Y.C. Yen** (1969) Thermal instability of a horizontal layer of liquid with maximum density. *American Institute of Chemical Engineers Journal*, **15**: 910–915.
- Tien, C.** (1968) Thermal instability of a horizontal layer of water near 4°C. *American Institute of Chemical Engineers Journal*, **14**: 652–653.
- Tkachev, A.G.** (1953) Heat exchange in melting and freezing of ice. In *Problems of Heat Transfer During a Change of State: A Collection of Articles*. Moscow: Translated from a publication of the state power press, AEC-TR-34-5, p. 169–178.
- Townsend, A.A.** (1964) Natural convection in water over an ice surface. *Quarterly Journal of the Royal Meteorological Society*, **90**: 248–259.
- Vanier, C.R. and C. Tien** (1968) Effect of maximum density and melting on natural convection heat transfer from a vertical plate. *Chemical Engineering Progress Symposium Series*, **64**: 240–254.
- Vanier, C.R. and C. Tien** (1970) Free convection melting of ice spheres. *American Institute of Chemical Engineers Journal*, **16**: 76–82.
- Vasseur, P., L. Robillard and B. Chandrashekar** (1983) Natural convection heat transfer of water within a horizontal annulus with density inversion effects. *Journal of Heat Transfer*, **105**: 117–123.
- Veronis, G.** (1963) Penetrative convection. *Astrophysical Journal*, **137**: 641–663.
- Watson, A.** (1972) The effect of the inversion temperature on the convection of water in an inclosed rectangular cavity. *Quarterly Journal of Mechanics and Applied Mathematics*, **25**: 423–446.

- Wilson, N.W. and B.D. Vyas** (1979) Velocity profiles near a vertical ice surface melting into fresh water. *Journal of Heat Transfer*, **101**: 313–317.
- Yen, Y.C.** (1968) Onset of convection in a layer of water formed by melting ice from below. *Physics of Fluids*, **11**: 1263–1270.
- Yen, Y.C. and F. Galea** (1969) Onset of convection in a water formed continuously by melting ice. *Physics of Fluids*, **12**: 509–516.
- Yen, Y.C.** (1980) Free convection heat transfer characteristics in a melt layer. *Journal of Heat Transfer*, **102**: 550–556.
- Yen, Y.C.** (1984) Temperature structure and interface morphology in melting ice-water system. In *Frontiers in Hydrology. Water Resources Publications*, p. 305–325.

REPORT DOCUMENTATION PAGE

Form Approved
OMB No. 0704-0188

Public reporting burden for this collection of information is estimated to average 1 hour per response, including the time for reviewing instructions, searching existing data sources, gathering and maintaining the data needed, and completing and reviewing the collection of information. Send comments regarding this burden estimate or any other aspect of this collection of information, including suggestion for reducing this burden, to Washington Headquarters Services, Directorate for Information Operations and Reports, 1215 Jefferson Davis Highway, Suite 1204, Arlington, VA 22202-4302, and to the Office of Management and Budget, Paperwork Reduction Project (0704-0188), Washington, DC 20503.

1. AGENCY USE ONLY (Leave blank)		2. REPORT DATE December 1990		3. REPORT TYPE AND DATES COVERED	
4. TITLE AND SUBTITLE Natural Convection Heat Transfer in Water Near its Density Maximum				5. FUNDING NUMBERS PE: 6.11.02A PR: 4A161102AT24 TA: SS WU: 09	
6. AUTHORS Yin-Chao Yen					
7. PERFORMING ORGANIZATION NAME(S) AND ADDRESS(ES) U.S. Army Cold Regions Research and Engineering Laboratory 72 Lyme Road Hanover, New Hampshire 03755-1290				8. PERFORMING ORGANIZATION REPORT NUMBER Monograph 90-4	
9. SPONSORING/MONITORING AGENCY NAME(S) AND ADDRESS(ES)				10. SPONSORING/MONITORING AGENCY REPORT NUMBER	
11. SUPPLEMENTARY NOTES					
12a. DISTRIBUTION/AVAILABILITY STATEMENT Approved for public release; distribution is unlimited. Available from NTIS, Springfield, Virginia 22161				12b. DISTRIBUTION CODE	
13. ABSTRACT (Maximum 200 words) This monograph reviews and summarizes to date the experimental and analytical results on the effect of water density near its maximum on convection, transient flow and temperature structure characteristics: 1) in a vertical enclosure, 2) in a vertical annulus, 3) between horizontal concentric cylinders, 4) in a square enclosure, 5) in a rectangular enclosure, 6) in a horizontal layer, 7) in a circular confined melt layer, and 8) in bulk water during melting. In a layer of water containing a maximum density temperature of 4°C, the onset of convection (the critical number) is found not to be a constant value as in the classical normal fluid but one that varies with the imposed thermal and hydrodynamic boundaries. In horizontal layers, a nearly constant temperature zone forms and continuously expands between the warm and cold boundaries. A minimum heat transfer exists in most of the geometries studied and, in most cases, can be expressed in terms of a density distribution parameter. The effect of this parameter on a cell's formation, disappearance and transient structure is discussed, and the effect of split-boundary flow on heat transfer is presented.					
14. SUBJECT TERMS Convection Heat transfer Hydrodynamic stability Ice-water systems Temperature-density relationships Water				15. NUMBER OF PAGES 104 16. PRICE CODE	
17. SECURITY CLASSIFICATION OF REPORT UNCLASSIFIED	18. SECURITY CLASSIFICATION OF THIS PAGE UNCLASSIFIED	19. SECURITY CLASSIFICATION OF ABSTRACT UNCLASSIFIED	20. LIMITATION OF ABSTRACT UL		